

Numerical Approximation of a Kinetic Model for Sedimentation in Suspensions of Rod-Like Particles using Hyperbolic Systems of Moment Equations

Inaugural dissertation

for the attainment of the title of doctor
in the Faculty of Mathematics and Natural Sciences
at the Heinrich Heine University Düsseldorf

presented by

Sina Dahm

from Radevormwald

Düsseldorf, September 2022

from the Mathematical Institute
at the Heinrich Heine University Düsseldorf

Published by permission of the
Faculty of Mathematics and Natural Sciences at
Heinrich Heine University Düsseldorf

Supervisor: Prof. Dr. Christiane Helzel
Heinrich Heine University Düsseldorf
Co-supervisor: Prof. Dr. Jennifer Ryan
KTH Royal Institute of Technology Stockholm

Date of the oral examination: 24/10/2022

Abstract

We study mathematical models and approximations for the sedimentation in dilute suspensions of rod-like particles. The starting point of our considerations is a coupled system of partial differential equations, previously derived by Helzel and Tzavaras [35], consisting of a kinetic equation for the rod orientation that is coupled to a macroscopic flow equation. It describes the motion of a suspension of rigid rod-like particles under the influence of gravity. Since the coupled system is high-dimensional (five dimensions + time) a direct numerical method is cumbersome. Thus, we are interested in the derivation of lower dimensional models which can adaptively adjust the level of detail.

Here we restrict ourselves to simplified flow situations on S^1 , i.e. the particle orientation is restricted to the plane spanned by the direction of shear and the direction of gravity. We derive hierarchies of moment equations which can be interpreted as approximations of the coupled kinetic model. We show that the systems of moment equations resulting from a simple moment closure are hyperbolic. While the original kinetic system is a time-dependent partial differential equation in space and orientation, the hyperbolic system of moment equations depends only on space and time.

An operator splitting method is used to compute the numerical solution of the coupled moment systems. Numerical simulations of the coupled moment systems for test cases motivated by physical phenomena such as the formation of clusters in an initially well stirred suspension or the instability of a sedimenting cloud of rod-like particles lead to accurate results once the number of moment equations is large enough.

We adapt the number of moment equations used in the hyperbolic moment system to locally varying accuracy requirements. For this purpose, we study an interface coupling of moment systems with different resolution and derive a conservative high-resolution Wave Propagation Algorithm for solving generalised Riemann problems of moment systems with different numbers of moment equations. Selection criteria for choosing the right number of moment equations is introduced. Finally, we analyse numerical simulations of the coupled shear flow problem in which the number of moment equations is adjusted adaptively in order to efficiently resolve relevant flow features.

Most of the results presented in this thesis can also be found in the publication [24].

Acknowledgement

I would like to express my deep and sincere gratitude to my supervisor, Prof. Dr. Christiane Helzel. Thank you for the opportunity for me to be part of your working group, to work on this interesting topic and to benefit from your sound scientific experience. Your tireless engagement and constant support not only enabled me to successfully complete the PhD, but also made the last four years a very valuable time that will always hold fond memories for me. I am grateful for inspiring discussions in which you shared your broad knowledge with me, for constructive advices and invaluable encouragement throughout all stages of my PhD studies. I very much appreciate that you offered me the opportunity to attend interesting conferences throughout Europe and to interact with international researchers. I could not have asked for a better supervisor.

My sincere thanks go to Prof. Dr. Jennifer K. Ryan for the co-supervision of this thesis. Your patient guidance at the beginning of my research project helped me in particular. I am grateful for your hospitality and many precious suggestions during my visit at the KTH Royal Institute of Technology in Stockholm. I have learned a lot from you and would like to express my thanks for that.

I would like to thank my colleagues and friends at the Mathematical Institute and especially at the chair of Applied Mathematics. I enjoyed working with you very much.

A special thank is due to my family and friends for always being there for me. Thank you, Alessia Platte, for being a friend for life. Raphael Kronberg and Christian Gesse, I am grateful that studying mathematics has brought us together and that we have become friends. In particular, I am deeply grateful to my beloved parents, Martina and Andreas Dahm, and grand-parents, Lore and Hans-Hermann Dahm, for making all this possible for me. You have always encouraged and motivated me. I thank you from the bottom of my heart for your generous support and valuable advices.

Finally, I would like to thank you, Marius Kottmann, for your love, for cheering me up and believing in me.

Table of Contents

Abstract	iii
Acknowledgement	iv
1. Introduction	1
1.1. Motivation	1
1.2. Overview over Existing Results in Literature	4
1.3. Dissertation Objectives	6
1.4. Dissertation Outline	7
2. High-Resolution Finite Volume Methods for Hyperbolic Conservation Laws	9
2.1. Hyperbolic Conservation Laws	9
2.1.1. One-Dimensional Riemann Problem	13
2.2. High-Resolution Finite Volume Method in One Space Dimension	15
2.2.1. Finite Volume Method	15
2.2.2. Godunov's Method	16
2.2.3. High-Resolution Wave Propagation	17
2.3. High-Resolution Finite Volume Method in Two Space Dimensions	19
2.3.1. Finite Volume Method	20
2.3.2. Godunov's Method	20
2.3.3. High-Resolution Wave Propagation	21
2.4. Operator Splitting for Handling Source Terms	24
2.4.1. Fractional-Step Method	25
2.4.2. Strang Splitting	25
2.5. Projection Method for the Two-Dimensional Navier-Stokes Equation	26
3. Multiscale Models for Sedimentation of Rod-Like Particles	30
3.1. General Model	30
3.2. Simplified Model for Two-Dimensional Flow	32
3.3. Simplified Model for Shear Flow	34

Table of Contents

4. A Detailed Numerical Method for the Coupled System	35
4.1. A Detailed Numerical Method for Shear Flow	35
4.1.1. Spectral Method for the Drift-Diffusion Equation	36
4.1.2. Outlook: Filtered Spectral Method for the Drift-Diffusion Equation	41
4.1.3. The One-Dimensional Transport Equation	44
4.2. A Detailed Numerical Method for General Two-Dimensional Flow	45
4.2.1. Spectral Method for the Drift-Diffusion Equation	46
4.2.2. The Two-Dimensional Transport Equation	48
4.3. Transfer of Different Degrees of Freedom	48
5. Hierarchy of Moment Equations	50
5.1. Definition of Moments and Moment Closure	50
5.2. Hierarchy of Moment Equations for Shear Flow	51
5.3. Hyperbolic Structure of the One-Dimensional System of Moment Equations for Shear Flow	55
5.4. Hierarchy of Moment Equations for General Two-Dimensional Flow	72
5.5. Hyperbolic Structure of the Two-Dimensional System of Moment Equations	75
6. Numerical Discretisation of the Coupled Moment System	89
6.1. Numerical Discretisation of the Coupled Moment System for Shear Flow . .	89
6.2. Numerical Discretisation of the Coupled Moment System for General Two- Dimensional Flow	91
6.3. Comparison with the Detailed Numerical Method	93
6.4. Numerical Simulations	100
7. Interface Coupling of Moment Systems with Different Resolution	106
7.1. Riemann Problems for Moment Systems with Different Resolution for Shear Flow	107
7.2. Numerical Discretisation of Moment Systems with Different Resolution for Shear Flow	110
8. Conclusions and Outlook	117
8.1. New Results	117
8.2. Future Work	117
Appendices	119
A. Statement about the Authors Contribution to Previously Published Work	120

Bibliography	121
List of Figures	129
List of Tables	133

Introduction

1.1 Motivation

Sedimentation in suspensions is a process that is frequently encountered in various areas of everyday life as well as in a wide range of industrial applications. Sedimenting particles in the air that contribute to the environmental pollution [57], the flow of red blood cells through the veins [72], the deposition of micro-plastic in the ocean [61], purification of waste water [83] or material processing in the paper industry [59] are only some of many familiar examples. Guazzelli and Morris [29] define a suspension as follows: Suspensions refer to particles dispersed in a liquid or a gas. If the particles dispersed in the fluid are larger than 10^{-1} mm and have a higher density than the fluid, gravitational forces lead to a deposition of the particles which is called sedimentation.

Although sedimentation is one of the simplest examples of suspension flows, the motion of the suspended particles can be very complex [27]. The sedimentation dynamics in suspensions are affected by various physical parameters, like the shape and rigidity of the suspended molecules or the properties of the fluid surrounding the particles. In contrast to spherical particles, the orientation of rigid anisotropic particles like fibres or rod-like particles strongly influences their motion and sensitivity to flow fields. For example, a particle with a vertical orientation sediments twice as fast as a particle with horizontal orientation and a particle with oblique orientation sediments sideways [25, App. 8.1]. In addition, the sedimentation process of rigid orientable particles is dependant on the concentration of the molecules in the fluid. Unlike spherical or flexible particles, rigid rods are affected by interactions with other particles even at low concentrations. As illustrated in Figure 1.1, Doi and Edwards [25] distinguish four concentration regimes for rod-like particles.

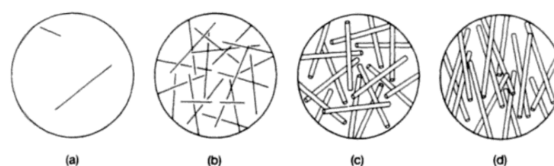


Figure 1.1.: Concentration regimes of rod-like polymers: (a) dilute solution, (b) semidilute solution, (c) isotropic concentrated solution, and (d) liquid crystalline solution. Compare with [25, Fig. 9.1].

The sedimentation process in dilute suspensions of rigid rod-like particles under the influence of gravity is of special interest due to its wide range of complex flow structures. A typical phenomenon during the sedimentation process in initially well-stirred suspensions of rod-like particles is the formation of concentration instabilities. Guazzelli and coworkers observed experimentally in [37], [36], [62], [63] that after some time and under the influence of gravity, initially homogeneously distributed rods form clusters with higher particle concentrations. Within a cluster, the rod-like particles are observed to orient strongly in the direction of gravity, occasionally they flip. As visualised in Figure 1.2, the clusters organise in downward flowing regions which are balanced by regions of backflow with a lower concentration of rods. Koch and Shaqfeh [49] theoretically explain the basic mechanism of the cluster formation in initially well-mixed suspensions with the hydrodynamic interaction between sedimenting rod-like particles. Each particle causes a disturbance in the fluid flow which, in turn, influences all the other particles.

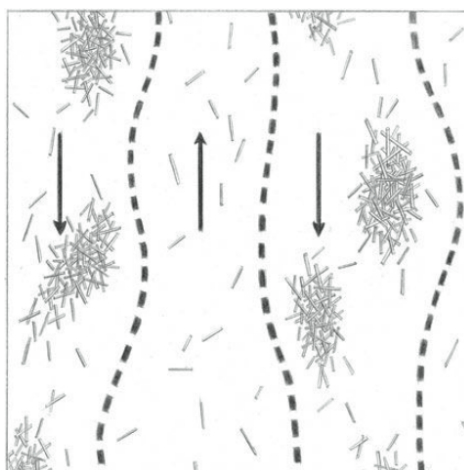


Figure 1.2.: Sketch of the structural instability of a sedimenting suspension of fibres. Compare with [29, chap. 6, Fig. 6.15].

Also for a cloud of a large number of randomly distributed rigid rod-like particles sedimenting in a viscous fluid interesting concentration fluctuations are observable which for example

occur in sedimentation of silt in rivers and on the continental shelf. Experimental simulations by Park et al. [70] show a repetitive deformation and break-up process of a sedimenting cloud of rod-like particles. Figure 1.3 illustrates how an initially spherical cloud deforms into a torus that destabilises and breaks into secondary unstable droplets. Nitsche and Batchelor [66] explain that hydrodynamic interactions cause particles located at the central region of the cloud to depart from a closed circulatory motion into a downstream tail so that the sedimenting cloud breaks into a torus.

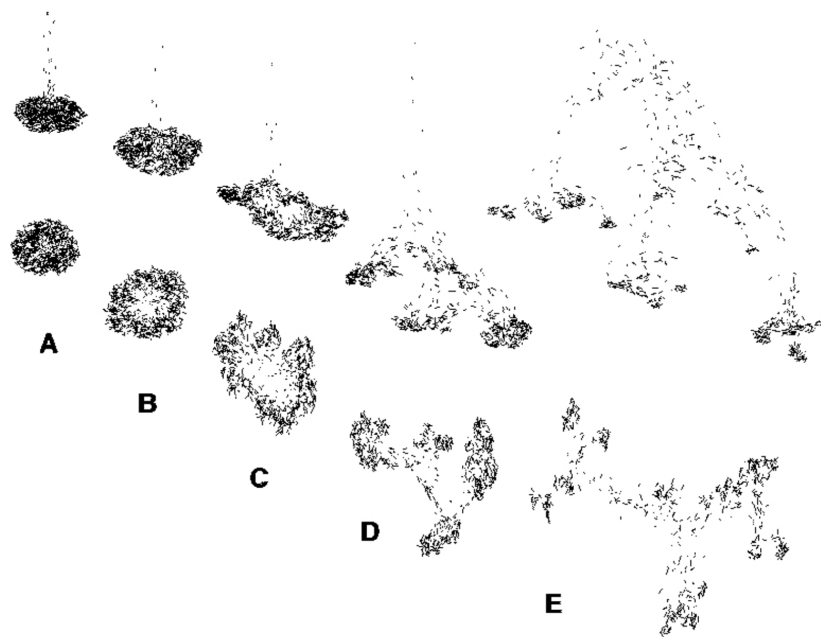


Figure 1.3.: Experimental simulation of the evolution of a cloud of rigid fibres. Images in the top row are views normal to the direction of gravity; the row of images on the bottom are views from the direction of gravity. The rigid fibres are made of copper with a dimension of $l = 0.127 \pm 0.013$ cm and $d = 0.0149 \pm 0.0020$ cm. Compare with [69, Fig. D-1], [70].

The exact mechanisms behind the complex flow structures in sedimentations of suspensions of rod-like particles, including the instability of sedimenting clouds or the formation of clusters of initially well-stirred suspensions described above, are still an object of active research. For example, the wavelength selection in the cluster formation or the further expansion of the torus into secondary droplets are still poorly understood.

In view of various industrial applications of sedimentation in suspensions of rod-like particles, the mathematical description of complex fluids with sedimenting microstructure is an important modeling problem. In this thesis, we focus on the derivation of macroscopic models and numerical methods in order to provide deeper insights into the mechanism of sedimentation in dilute suspensions of rigid rod-like Brownian particles in a viscous fluid.

1.2 Overview over Existing Results in Literature

Various approaches to derive mathematical models and numerical methods have been proposed to confirm the structural instabilities in sedimenting suspensions of rod-like particles described in the last section. In this section, a brief overview of existing approaches in literature is given. For more details also see the review paper by Guazzelli and Hinch [28] or the monograph by Binetruy, Chinesta and Keunings [9, chap. 1] and references therein.

Mathematical models and numerical simulations of the microscopic interaction between the orientation of rod-like particles and the fluid leading to concentration instabilities on a macroscopic level were introduced with different degrees of detail, ranging from simulations of individual particles at the microscopic scale to macroscopic models describing the collective behaviour of the suspension dynamics.

On the microscopic level, the hydrodynamic interaction of each particle is modeled deterministically in order to explain the macroscopic dynamics of the suspension. The main difficulty of this approach is that the number of particles that can be simulated is limited due to high computational costs. The numerical computations by Mackaplow and Shaqfeh [60] use the slender body approximation developed by Batchelor [7] to model the interplay of 100 suspended rods with the fluid. Batchelor states in [7] that the basic idea of slender body theory is that the disturbance created by a long solid particle is approximately the same as that due to a suitably chosen line distribution of point forces along the particle axis. A detailed analysis of the cluster formation of up to a few hundred rod-like particles is given by Gustavsson and Tornberg [84], [45]. Butler and Shaqfeh [11] reduce the computational costs by considering a lower order slender body description which is based on a point-force approximation rather than a line distribution of forces. Saintillan, Darve, and Shaqfeh [77] as well as Nazockdast et. al. [65] improve the algorithm by using fast-summation techniques and model suspensions with several thousand rod-like particles. Hamid et al. [31] approximate the interaction of the rods with a bead-chain model and use a direct numerical simulation to analyse the microstructure of the suspension.

On the mesoscopic level, the individual simulation of a large number of rod-like particles is replaced by a distribution function describing the probability that a population of Brownian particles has a given orientation at a given time and position in the domain. The time evolution of the distribution function is determined by the kinetic Smoluchowski equation, a Fokker-Planck type equation, which has to be solved in physical space (space and

time), configuration space (e. g. orientation) and temporal domain. A rigorous theoretical framework for kinetic models describing suspensions of rigid anisotropic particles in the four different regimes mentioned in Figure 1.1 has been established by Doi and Edwards [25].

For simple flow situations like shear flow, the full kinetic model can be solved with standard numerical methods like finite-volume methods on the sphere [32], [35], finite element and spectral methods [13], [48], [42], finite difference methods [78] or radial basis functions [33]. For more complicated situations, the development of appropriate numerical methods for the coupled system is challenging due to the high-dimensionality of the kinetic equation. A direct numerical method for Fokker-Planck equations with many configurational degrees of freedom is the technique of Proper Generalized Decomposition (or PGD) which is based on the use of separated representations of each coordinate [15], [5], [4]. Various model reduction techniques were derived e.g. in [64], [16], [23].

An alternative approach to circumvent the high-dimensionality of the deterministic Fokker-Planck equation is to solve the associated stochastic differential equation [67]. Since the introduction of the CONNFESSIT (Calculation of Non-Newtonian Flow: Finite Elements and Stochastic Simulation Technique) method by Öttinger and Laso [50], which combines finite element methods with Monte-Carlo simulations, various stochastic numerical methods have been developed for the stochastic representation of the Fokker-Planck equation, like the method of Brownian configuration fields [41] or the Lagrangian particle method [30]. An overview of both methods can be found in the review paper by Keunings [46]. Several extensions of these approaches have been an object of active research in recent years [51], [12], [82]. Other recently developed mesoscopic methods for the numerical treatment of the full kinetic model are reviewed in [3].

In this thesis, we are interested in the derivation of mathematical models and numerical simulations on the macroscopic level. On the macroscopic level, the density function for the rod orientation in every point of the domain is replaced in favour of computational efficiency by its moment equations whose time evolution only involves the space variables [2], [1], [71]. A typical approximation of the distribution function of rod orientation is the Galerkin ansatz which uses spherical harmonics [80]. The downside of this approach is that the derivation of the lower-dimensional models involves moment closure approximations which can lead to inaccuracies or unphysical solutions [79], [58], [20]. Hinch and Leal analyse in detail the moment closure mechanism for a system describing suspensions of rigid rods in [39].

The starting point of the consideration in this thesis is a multiscale model by Helzel and Tzavaras [35] for sedimentation in dilute suspensions of rod-like particles under the influence

of gravity. In [35], [34], Helzel and Tzavaras prove that the high-dimensional mathematical model is thermodynamically consistent. They perform a moment closure from the full coupled system, based on deriving equations for the first three moments and using the structure of spherical harmonics to suggest a closure strategy. A macroscopic evolution equation for the rod density is obtained by considering a quasi-dynamic approximation which consists of setting the higher order moments to their local equilibrium and evaluating them in terms of the zeroth moment and its spatial derivatives. In addition, a second macroscopic model is obtained by taking the diffusive limit of the full multiscale model. Numerical simulations with those lower dimensional models reproduce the cluster formations that were observed in experiments. In some situations, these simple models which only use very few moments produce unphysical solutions. We will provide a simple example in chapter 6.

1.3 Dissertation Objectives

The central goal of this thesis is to develop new mathematical models and approximations for sedimentation in dilute suspensions of rod-like particles which can adaptively adjust the level of detail to efficiently produce physically correct solutions. The main objectives are defined as follows:

- Describe a detailed numerical method for the high-dimensional coupled model by Helzel and Tzavaras [35] for sedimentation in suspensions of rod-like particles for shear flow and two-dimensional flow.
- Derive a hierarchy of moment equations based on spherical harmonics and a moment closure mechanism for the kinetic model for shear flow and two-dimensional flow.
- Show the hyperbolicity of the systems of moment equations.
- Numerically solve the hyperbolic systems of moment equations and couple them with the diffusion equation in case of shear flow and with the Navier-Stokes equation in case of two-dimensional flow.
- Compare the numerical solutions of the lower dimensional system of moment equations and the detailed kinetic model.
- Based on locally varying accuracy requirements, adapt the number of moments in the hyperbolic moment system.

1.4 Dissertation Outline

In this section, the outline of the dissertation is given.

- In **chapter 2**, we provide a brief overview of relevant background knowledge on hyperbolic conservation laws, high-resolution finite volume methods and the related Wave Propagation Algorithm by LeVeque [56] that will be used in the following chapters to analyse the systems in question. In addition, we present a projection method by Long Lee [52] for solving the two-dimensional Navier-Stokes equation. Readers familiar with these numerical tools can skip this chapter.
- In **chapter 3**, we introduce the underlying mathematical model describing sedimentation in dilute suspensions of rod-like particles under the influence of gravity. The system of partial differential equations was derived by Helzel and Tzavaras [35] and couples a Smoluchowski equation with a Navier-Stokes system. Moreover, simplified lower dimensional models for rods with orientation restricted to the plane S^1 for shear flow and general two-dimensional flow are presented. These two models will be the basis for all further considerations.
- In **chapter 4**, we describe a direct numerical method for the coupled system which couples a Navier-Stokes solver for the flow equation with a spectral method for the Smoluchowski equation. This method will serve as a reference for theoretical comparisons with approaches introduced in the remaining part of the thesis.
- In **chapter 5**, hierarchies of moment equations and a moment closure mechanism for the shear flow and the two-dimensional flow problem are derived. We prove that the systems of moment equations are hyperbolic.
- In **chapter 6**, the numerical discretisation of the coupled moment systems is presented. A splitting approach is used for solving the coupled moment systems. We show that the moment system can be interpreted as an approximation of the more detailed kinetic model. Numerical simulations of test cases motivated by physical applications as the cluster formation or the instability of suspended particle clouds illustrate that the coupled moment systems accurately approximate a reference solution if a sufficiently large number of moments is used.
- In **chapter 7**, we adaptively adjust the level of detail in different spatial regions of the domain by coupling moment systems with different numbers of moment equations. A conservative high-resolution Wave Propagation Algorithm for moment systems with

different resolution is derived. Selection criteria for choosing the right number of moment equations is presented.

- In **chapter 8**, we close with conclusions and an outlook on future research.

The main results, presented in chapter 4 - chapter 6, were published in [24]. In appendix A, a statement about my contribution to this publication is given.

High-Resolution Finite Volume Methods for Hyperbolic Conservation Laws

This chapter is intended to give a brief overview of the relevant concepts essential to analyse and solve hyperbolic conservation laws with high-resolution finite volume methods and to establish the notation used in the following chapters. For a more detailed study of hyperbolic conservation laws and their numerical treatment, the reader is referred to [53], [54], [55], [56].

After giving a short introduction on hyperbolic conservation laws and the fundamental solutions to Riemann problems in section 2.1, we will present the concept of high-resolution finite volume methods for solving homogeneous conservation laws in one space dimension, see section 2.2, as well as in two space dimensions, see section 2.3. In section 2.4, two different splitting approaches for solving conservation laws with source terms are introduced. The presentation in these four sections is mostly based on LeVeque [56] and [55]. Finally, in section 2.5, we present a projection method based on high-resolution finite volume methods for solving the incompressible Navier-Stokes equation which was developed by Long Lee [52]. Throughout this chapter, we illustrate the presented theoretical background and the numerical methods in various examples related to the models of interest.

2.1 Hyperbolic Conservation Laws

In this section, we present the general form of conservation laws. In addition, we summarise the basic properties of hyperbolic linear systems and similarity transformations which will be used in section 5.3 to prove the hyperbolicity of the one- and two-dimensional systems of moment equations.

The class of homogeneous partial differential equations of the form

$$\frac{\partial q(x, t)}{\partial t} + \nabla_x \cdot f(q(x, t)) = 0, \quad x = (x_1, \dots, x_d)^T \in \Omega, \quad t > 0, \quad (2.1)$$

is called conservation law. $q : \Omega \times \mathbb{R}^+ \rightarrow \mathbb{R}^m$ is a vector of m conserved quantities and the vector valued functions $f_1, \dots, f_d : \mathbb{R}^m \rightarrow \mathbb{R}^m$ are the so-called flux functions. We denote the spatial variable with $x = (x_1, \dots, x_d)^T \in \Omega$, where $\Omega \subset \mathbb{R}^d$ is an arbitrary region, and the time variable with $t \in \mathbb{R}^+$. The integration of (2.1) over a space-time volume $\Omega \times [t^n, t^{n+1}]$ and the subsequent application of the divergence theorem for an outward unit normal vector $n = (n_1, \dots, n_d)^T$ to the boundary $\partial\Omega$ of Ω transforms (2.1) into an integral equation of the form

$$\int_{\Omega} q(x, t^{n+1}) dx - \int_{\Omega} q(x, t^n) dx + \int_{t^n}^{t^{n+1}} \int_{\partial\Omega} f(q(x, t)) n dS = 0, \quad (2.2)$$

which clarifies the eponymous characteristic of conservation laws. Equation (2.2) indicates that the rate of change of the total mass q contained in a domain Ω is equal to the flux $f(q)$ through the boundary $\partial\Omega$ of the domain. In the inside of the domain, the amount of the quantity q neither increases nor decreases and is thus conserved. If we add a non-zero source term $\psi(q(x, t))$, equation (2.1) is called balance law.

For sufficiently smooth f , the conservation law (2.1) can be rewritten in the quasilinear form

$$\frac{\partial q(x, t)}{\partial t} + \sum_{j=1}^d A_j(q) \frac{\partial q(x, t)}{\partial x_j} = 0,$$

where the entries (i, k) of the Jacobian matrix $A_j(q)$ are defined as

$$(A_j(q))_{i,k} = \frac{\partial f_{j,i}(q)}{\partial q_k}.$$

The class of conservation laws that satisfies the property of hyperbolicity in the sense of Definition 2.1 is of special interest.

2.1 Definition. The system of conservation laws (2.1) is called hyperbolic if for any direction defined by the unit vector $n \in \mathbb{R}^d$, $|n| = 1$, and any $q : \Omega \times \mathbb{R}^+ \rightarrow \mathbb{R}^m$ the matrix

$$\check{A}(q) = \sum_{j=1}^d n_j A_j(q)$$

is diagonalisable with real eigenvalues. We denote the eigenvalues by

$$\lambda^1 \leq \lambda^2 \leq \dots \leq \lambda^m.$$

The matrix \check{A} is diagonalisable if there is a complete set of eigenvectors, i.e. if there are

nonzero vectors $r^1, r^2, \dots, r^m \in \mathbb{R}^m$ such that

$$\check{A}r^p = \lambda^p r^p, \quad 1 \leq p \leq m$$

and these vectors are linearly independent.

In the following, some basic results from linear algebra are listed which will be used in chapter 5 to show that the one- and two-dimensional systems of moment equations are hyperbolic.

2.2 Theorem. [6, Theorem 7.2.1] *If A is a $n \times n$ matrix, then the following are equivalent.*

(a) *A is orthogonally diagonalisable.*

(b) *A is symmetric.*

Proof. The proof can be found in [6, Theorem 7.2.1]. □

2.3 Definition. [40, Definition 1.3.1] Let $A, B \in \mathbb{R}^{n \times n}$ be given. We say that B is similar to A if there exists a nonsingular $S \in \mathbb{R}^{n \times n}$ such that $B = SAS^{-1}$.

2.4 Theorem. [40, Corollary 1.3.4] *If two matrices are similar, they have the same eigenvalues.*

Proof. The proof can be found in [40, Corollary 1.3.4]. □

2.5 Example. *We study the following system of conservation laws*

$$\partial_t \begin{pmatrix} \rho \\ C_1 \\ S_1 \end{pmatrix} + \underbrace{\begin{pmatrix} 0 & 0 & -1 \\ 0 & 0 & 0 \\ -1/8 & 0 & 0 \end{pmatrix}}_{A:=} \partial_x \begin{pmatrix} \rho \\ C_1 \\ S_1 \end{pmatrix} = 0. \quad (2.3)$$

We will see in Example 5.1 that (2.3) corresponds to the homogeneous system of moment equations describing sedimentation in suspensions of rod-like particles in shear flow. In this example, we present two approaches to show that (2.3) is hyperbolic, using Definition 2.1 or alternatively Theorem 2.2 and Theorem 2.4.

Eigenvalues and eigenvectors of system (2.3) are given as

$$\lambda_1 = -\frac{\sqrt{2}}{4}, \quad \lambda_2 = 0, \quad \lambda_3 = \frac{\sqrt{2}}{4} \quad (2.4)$$

and

$$r_1 = \begin{pmatrix} 2\sqrt{2} \\ 0 \\ 1 \end{pmatrix}, \quad r_2 = \begin{pmatrix} 0 \\ 1 \\ 0 \end{pmatrix}, \quad r_3 = \begin{pmatrix} -2\sqrt{2} \\ 0 \\ 1 \end{pmatrix}. \quad (2.5)$$

As A has a complete set of linearly independent eigenvectors such that

$$Ar^p = \lambda^p r^p, \quad p = 1, 2, 3,$$

the system is hyperbolic by Definition 2.1.

Alternatively, the hyperbolicity of system (2.3) can be proven by considering the 7×7 matrix

$$\bar{A} = \left(\begin{array}{c|c} 0 & 0 \\ \hline 0 & \begin{array}{c|c} A & 0 \\ \hline 0 & A \end{array} \end{array} \right) = \begin{pmatrix} 0 & 0 & 0 & 0 & 0 & 0 & 0 \\ 0 & 0 & 0 & -1 & 0 & 0 & 0 \\ 0 & 0 & 0 & 0 & 0 & 0 & 0 \\ 0 & -\frac{1}{8} & 0 & 0 & 0 & 0 & 0 \\ 0 & 0 & 0 & 0 & 0 & 0 & -1 \\ 0 & 0 & 0 & 0 & 0 & 0 & 0 \\ 0 & 0 & 0 & 0 & -\frac{1}{8} & 0 & 0 \end{pmatrix}.$$

As the characteristic polynomial $p_{\bar{A}}(\lambda)$ of the block diagonal matrix $\bar{A} \in \mathbb{R}^{7 \times 7}$ has the form

$$p_{\bar{A}}(\lambda) = \det(\lambda I_7 - \bar{A}) = \lambda \det(\lambda I_3 - \bar{A}) \det(\lambda I_3 - \bar{A}) = \lambda (p_A(\lambda))^2,$$

\bar{A} has the same eigenvalues as A but counted twice and an additional eigenvalue 0. A similarity transformation of the form $S\bar{A}S^{-1}$ with

$$S = \begin{pmatrix} 1 & 0 & 0 & 0 & 0 & 0 & 0 \\ 0 & 0 & 1 & -1 & 0 & 0 & 0 \\ 0 & 0 & 0 & 0 & 0 & 1 & -1 \\ 0 & 0 & 0 & 0 & \frac{1}{2} & 0 & 0 \\ 0 & -\frac{1}{2} & 0 & 0 & 0 & 0 & -1 \\ 0 & 0 & 1 & 1 & 0 & 0 & 0 \\ 0 & 0 & 0 & 0 & 0 & 1 & 1 \end{pmatrix}, \quad S^{-1} = \begin{pmatrix} 1 & 0 & 0 & 0 & 0 & 0 & 0 \\ 0 & 0 & 0 & 0 & -2 & 0 & 0 \\ 0 & \frac{1}{2} & 0 & 0 & 0 & \frac{1}{2} & 0 \\ 0 & -\frac{1}{2} & 0 & 0 & 0 & \frac{1}{2} & 0 \\ 0 & 0 & 0 & 2 & 0 & 0 & -1 \\ 0 & 0 & \frac{1}{2} & 0 & 0 & 0 & \frac{1}{2} \\ 0 & 0 & -\frac{1}{2} & 0 & 0 & 0 & \frac{1}{2} \end{pmatrix},$$

leads to the symmetric matrix

$$\tilde{A} = S\bar{A}S^{-1} = \begin{pmatrix} 0 & 0 & 0 & 0 & 0 & 0 & 0 \\ 0 & 0 & 0 & 0 & -\frac{1}{4} & 0 & 0 \\ 0 & 0 & 0 & \frac{1}{4} & 0 & 0 & 0 \\ 0 & 0 & \frac{1}{4} & 0 & 0 & 0 & -\frac{1}{4} \\ 0 & -\frac{1}{4} & 0 & 0 & 0 & \frac{1}{4} & 0 \\ 0 & 0 & 0 & 0 & \frac{1}{4} & 0 & 0 \\ 0 & 0 & 0 & -\frac{1}{4} & 0 & 0 & 0 \end{pmatrix}.$$

As a consequence of Theorem 2.2 and Theorem 2.4, all eigenvalues of \bar{A} and consequently all eigenvalues of A are real. Furthermore, the matrix \bar{A} has a complete set of eigenvectors. Using the special structure of \bar{A} , it follows that A has a complete set of right eigenvectors.

In chapter 5, the approach presented in example 2.5 will be extended to general N to show that the one-dimensional system of moment equations for shear flow is hyperbolic.

2.1.1 One-Dimensional Riemann Problem

In this subsection, we concentrate on spatially one-dimensional linear systems of hyperbolic conservation laws, i.e.

$$q_t(x, t) + f(q)_x = 0, \quad x \in \mathbb{R}, \quad t > 0, \quad (2.6)$$

where $q : \mathbb{R} \times \mathbb{R}^+ \rightarrow \mathbb{R}^m$ represents a vector of m conserved quantities and $f(q(x, t)) := Aq(x, t)$ the flux function. $A \in \mathbb{R}^{m \times m}$ is hyperbolic in the sense of Definition 2.1. We study a so-called Riemann problem in which (2.6) is considered together with initial data that is piecewise constant with a jump discontinuity

$$q_0(x) = \begin{cases} q_l, & x < 0, \\ q_r, & x > 0. \end{cases} \quad (2.7)$$

In this special case, the solution of the conservation law is a similarity solution of the form

$$q(x, t) = \tilde{q}(x/t),$$

which is constant along $x/t = \text{constant}$ through the origin [56, chap. 5]. m discontinuities propagating at speeds given by the eigenvalues of A separate the solution into $(m + 1)$ constant

states $q_l, \tilde{q}_1, \dots, \tilde{q}_{m-1}, q_r$ which can be decomposed into eigenvectors of A

$$q_r - q_l = R\alpha = \sum_{p=1}^{M_w} \mathcal{W}^p, \quad (2.8)$$

where $\alpha = R^{-1}(q_r - q_l)$ and $R = (r_1|r_2|\dots|r_m)$ is the matrix of the eigenvectors corresponding to the eigenvalues of the coefficient matrix A . In the representation (2.8), the discontinuities are interpreted as M_w waves $\mathcal{W}^p \in \mathbb{R}^m$ traveling with speed λ^p through the domain. In terms of the waves, the solution to the Riemann problem is given as

$$q(x, t) = q_l + \sum_{p:\lambda^p < x/t} \mathcal{W}^p = q_r - \sum_{p:\lambda^p \geq x/t} \mathcal{W}^p. \quad (2.9)$$

2.6 Example. We consider a Riemann problem for the system of conservation laws (2.3). With the eigenvalues (2.4) and eigenvectors (2.5) we calculate the solution of the Riemann problem as

$$q(x, t) = \begin{cases} q_l, & x - \lambda^1 t < 0, \\ \tilde{q}_1 := q_l + \mathcal{W}^1, & x \in (\lambda^1 t, \lambda^2 t), \\ \tilde{q}_2 := q_l + \mathcal{W}^1 + \mathcal{W}^2, & x \in (\lambda^2 t, \lambda^3 t), \\ q_r, & x - \lambda^3 t > 0. \end{cases}$$

The solution of the Riemann problem in the $x - t$ -plane is visualised in Figure 2.1.

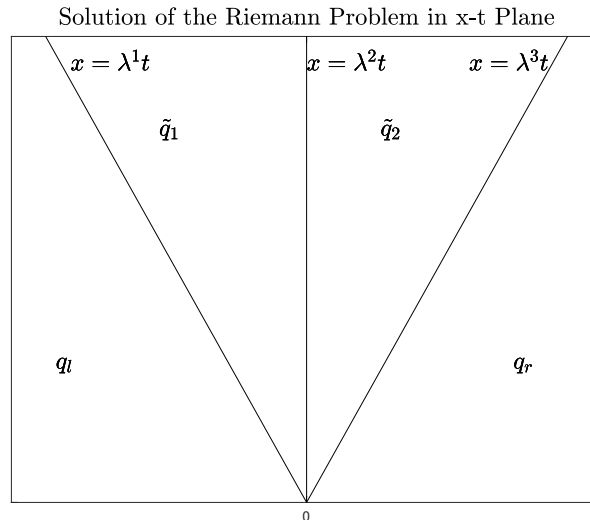


Figure 2.1.: Construction of the solution of the Riemann problem in Example 2.6 in the $x - t$ plane. The jump across each discontinuity in the solution is an eigenvector of A .

2.2 High-Resolution Finite Volume Method in One Space Dimension

The numerical solution of one space dimensional hyperbolic conservation laws (2.6) can be calculated with numerical methods that belong to the class of high-resolution finite volume methods. In this section, the basic concept of the scheme in one space dimension and the related Wave Propagation Algorithm is described.

We discretise the spatial domain $\Omega := [x_l, x_r]$ with an equidistant numerical grid $x_l = x_{\frac{1}{2}}, \dots, x_{M+\frac{1}{2}} = x_r$ with grid cells

$$C_i := \left[x_{i-\frac{1}{2}}, x_{i+\frac{1}{2}} \right], \quad i = 1, \dots, M, \quad (2.10)$$

of length $\Delta x := x_{i+\frac{1}{2}} - x_{i-\frac{1}{2}}$. To discretise the time variable, we consider $0 = t^0 < t^1 < t^2 < \dots$ and define the length of the time step as $\Delta t := t^{n+1} - t^n, \forall n \in \mathbb{N}_0$.

2.2.1 Finite Volume Method

The idea of solving the homogeneous hyperbolic partial differential equation (2.6) with a finite volume method is based on subdividing the spatial domain into grid cells and modifying the cell average of q in each time step by the flux through the edges of the grid cells. The approach of a finite volume method in one dimension is presented as a schematic in Figure 2.2.

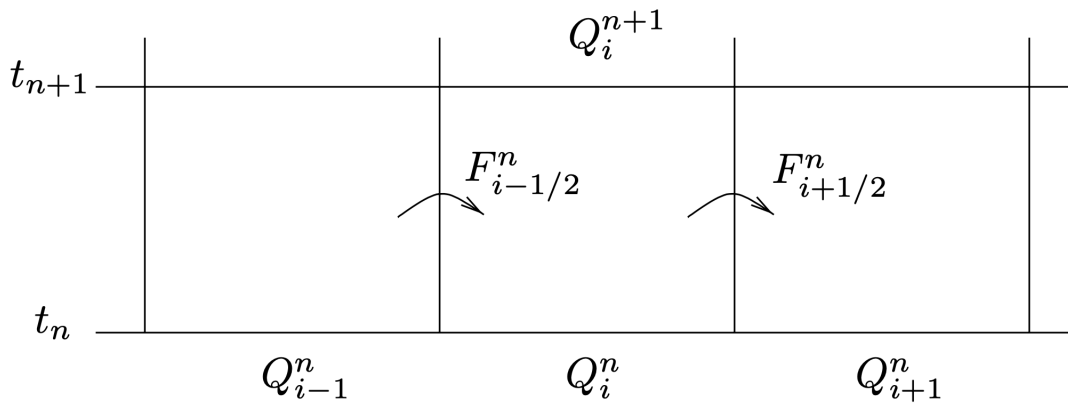


Figure 2.2.: Illustration of a finite volume method for updating the cell average Q_i^n by fluxes at the cell edge. Shown in the $x - t$ space. Compare with [56, chap. 4].

A finite volume method computes the numerical solution Q_i^n of (2.6) as an approximation of

the integral of the exact solution $q(x, t^n)$ over the i th grid cell at time t^n

$$Q_i^n \approx \frac{1}{\Delta x} \int_{x_{i-1/2}}^{x_{i+1/2}} q(x, t^n) dx = \frac{1}{\Delta x} \int_{C_i} q(x, t^n) dx.$$

In contrast to the point-wise approach of finite difference methods, finite volume methods are derived on the basis of the integral form (2.2) of the conservation law. In the standard flux-difference form, a conservative finite volume method is given as

$$Q_i^{n+1} = Q_i^n - \frac{\Delta t}{\Delta x} \left(F_{i+1/2}^n - F_{i-1/2}^n \right), \quad (2.11)$$

where

$$F_{i-1/2}^n \approx \frac{1}{\Delta t} \int_{t_n}^{t_{n+1}} f(x_{i-1/2}, t) dt$$

is an approximation to the average flux f along $x = x_{i-1/2}$. Hence, the main challenge of finite volume methods is to define an approximative evaluation $F_{i-1/2}^n$ of the average flux f so that the scheme converges to the exact solution of the conservation law.

2.2.2 Godunov's Method

A special class of finite volume methods are Godunov-type methods [26], which determine the flux on the basis of solving Riemann problems at the interface between grid cells exactly or approximately. This suggests the definition of the numerical flux in the finite volume method as

$$F_{i-1/2}^n = \frac{1}{\Delta t} \int_{t^n}^{t^{n+1}} f(q^*(Q_{i-1}, Q_i)) dt,$$

where $q^*(Q_{i-1}, Q_i)$ is the exact or approximate solution of the Riemann problem (2.7) at $x_{i-1/2}$.

The wave propagation form of Godunov's Method uses a more general decomposition of hyperbolic problems which allows an easier application of the method to systems that are not in conservative form. The method is defined as

$$Q_i^{n+1} = Q_i^n - \frac{\Delta t}{\Delta x} \left(\mathcal{A}^+ \Delta Q_{i-\frac{1}{2}} + \mathcal{A}^- \Delta Q_{i+\frac{1}{2}} \right). \quad (2.12)$$

This formulation of the method is based on the fact that the solution of a Riemann problem can be expressed as a set of waves, see equation (2.8), and calculates the numerical solution Q_i^{n+1} at time t^{n+1} by considering the net effect of all left-going waves arising from a Riemann

problem at cell edge $x_{i+\frac{1}{2}}$

$$\mathcal{A}^- \Delta Q_{i+\frac{1}{2}} = (\lambda^p)^-(Q_{i+1} - Q_i) = \sum_{p=1}^m (\lambda^p)^- \mathcal{W}_{i+\frac{1}{2}}^p, \quad (2.13)$$

and all right-going waves from a Riemann problem at cell edge $x_{i-\frac{1}{2}}$

$$\mathcal{A}^+ \Delta Q_{i-\frac{1}{2}} = \sum_{p=1}^m (\lambda^p)^+ \mathcal{W}_{i-\frac{1}{2}}^p, \quad (2.14)$$

where $\lambda^+ = \max(\lambda, 0)$ and $\lambda^- = \min(\lambda, 0)$. The so-called fluctuations $\mathcal{A}^\pm \Delta Q_{i-\frac{1}{2}}$ have to satisfy a conservation condition of the form

$$f(Q_i) - f(Q_{i-1}) = \mathcal{A}^- \Delta Q_{i-\frac{1}{2}} + \mathcal{A}^+ \Delta Q_{i-\frac{1}{2}}. \quad (2.15)$$

Godunov's methods are often called REA algorithm, standing for reconstruct-evolve-average. For more details on the algorithm, we refer to [55, chap. 4.10].

2.7 Example. For the linear system (2.3), Godunov's Method is visualised in Figure 2.3. As the second eigenvalue of A is zero, we have only two waves. The fluctuations are given as

$$\mathcal{A}^+ \Delta Q_{i-\frac{1}{2}} = \lambda^1 \mathcal{W}_{i-\frac{1}{2}}^1, \quad \mathcal{A}^- \Delta Q_{i+\frac{1}{2}} = \lambda^3 \mathcal{W}_{i+\frac{1}{2}}^3$$

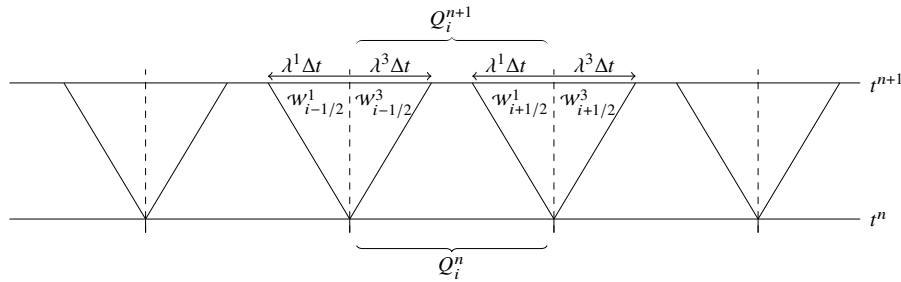


Figure 2.3.: Schematic of Godunov's Method for the linear system in (2.3). Riemann problems are solved at each interface. The exact solution at time t^{n+1} is determined by the wave structure. The solution is averaged over the grid cell to determine Q_i^{n+1} .

2.2.3 High-Resolution Wave Propagation

In the following, we will analyse the class of high-resolution Wave Propagation Algorithms. The scheme is numerically conservative, robust when discontinuities are present, capable of

capturing shock waves accurately and stable up to a CFL number of one.

The idea of high-resolution methods is based on extending the first-order accurate Godunov's method with second-order correction terms which are modified by limiter functions

$$Q_i^{n+1} = Q_i - \underbrace{\frac{\Delta t}{\Delta x} (\mathcal{A}^+ \Delta Q_{i-1/2} + \mathcal{A}^- \Delta Q_{i+1/2})}_{\text{first-order Godunov update}} - \underbrace{\frac{\Delta t}{\Delta x} (\tilde{F}_{i+1/2} - \tilde{F}_{i-1/2})}_{\text{second-order correction}}. \quad (2.16)$$

Using the Lax-Wendroff technique, the second-order correction term is defined as

$$\tilde{F}_{i-1/2} = \frac{1}{2} \sum_{p=1}^m |\lambda^p| \left(1 - \frac{\Delta t}{\Delta x} |\lambda^p| \right) \tilde{W}_{i-1/2}^p, \quad (2.17)$$

which is based on the Taylor series expansion of $q(x, t^{n+1})$ up to second-order. As the second-order accurate Lax-Wendroff method leads to unphysical oscillations near discontinuities or steep gradients while Godunov's method results in reasonable solutions in these regions, the limited wave $\tilde{W}_{i-1/2}^p$ analyses the solution's local behaviour and ensures that the second order flux is only used in smooth solution regions while the update is calculated with Godunov's method near steep gradients. The decomposition into waves is used to measure the smoothness of the solution by comparing waves arising from neighbouring Riemann problems

$$\tilde{W}_{i-1/2}^p = \tilde{\alpha}_{i-1/2}^p r^p, \quad \tilde{\alpha}_{i-1/2}^p = \alpha_{i-1}^p \varphi(\theta_{i-1/2}^p).$$

The ratio of wave strengths $\theta_{i-1/2}^p$ is defined as

$$\theta_{i-1/2}^p = \frac{\alpha_{I-1/2}^p}{\alpha_{i-1/2}^p} \quad \text{with } I = \begin{cases} i-1, & \lambda^p > 0, \\ i+1, & \lambda^p < 0. \end{cases} \quad (2.18)$$

We expect $\theta_{i-1/2}^p \approx 1$ for smooth solutions, except at extrema, and $\theta_{i-1/2}^p \approx 0$, in case of discontinuities. Depending on the smoothness of the solution, the limiter $\varphi(\theta)$ switches the second order correction terms on or off. More information on flux limiters and commonly used limiter functions can be found in [56].

A necessary condition for stability and convergence of the method is the CFL condition, see [22]

$$\frac{\Delta t}{\Delta x} \max_p |\lambda^p| \leq 1.$$

2.8 Example. We solve the scalar advection equation

$$q_t(x, t) + uq_x(x, t) = 0, \quad x \in \mathbb{R}, t > 0, \quad (2.19)$$

where $u > 0$ is constant, with the high-resolution Wave Propagation Algorithm. As we only have a scalar value u in (2.19), we have

$$\mathcal{A}^+ \Delta Q_{i-1/2, j} = u(Q_i - Q_{i-1}), \quad \mathcal{A}^- \Delta Q_{i-1/2, j} = 0.$$

The total update is given as

$$Q_i^{n+1} = Q_i^n - \frac{\Delta t}{\Delta x} u(Q_i - Q_{i-1}) - \frac{1}{2} \frac{\Delta t}{\Delta x} u \left(1 - \frac{\Delta t}{\Delta x} u \right) (\sigma_{i+1/2}^n - \sigma_{i-1/2}^n),$$

with

$$\sigma_{i-1/2}^n = (Q_i^n - Q_{i-1}^n) \varphi \left(\theta_{i-1/2}^n \right) = (Q_i^n - Q_{i-1}^n) \varphi \left(\frac{Q_{i-1} - Q_{i-2}}{Q_i - Q_{i-1}} \right).$$

A detailed derivation of the method for the scalar advection equation and the formulation in flux-difference form can be found in [54].

2.3 High-Resolution Finite Volume Method in Two Space Dimensions

In this section, the high-resolution finite volume method from section 2.2 is expanded to solve hyperbolic conservation laws in two space dimensions.

We consider the conservation law (2.1) with $q : \Omega \times \mathbb{R}^+ \rightarrow \mathbb{R}^m$ on the arbitrary region $\Omega \subset \mathbb{R}^2$. The flux functions are vectors of the form $f_1, f_2 : \mathbb{R}^m \rightarrow \mathbb{R}^m$ with $f_1(q(x, t)) := Aq(x, y, t)$ and $f_2(q(x, y, t)) := Bq(x, y, t)$. The matrices $A \in \mathbb{R}^{m \times m}$ and $B \in \mathbb{R}^{m \times m}$ are hyperbolic in the sense of Definition 2.1. The two-dimensional spatial domain $\Omega := [x_l, x_r] \times [y_l, y_r]$ is discretised on an equidistant numerical grid. In Figure 2.4, we illustrate a rectangular grid cell of the form

$$C_{i,j} := \left[x_{i-\frac{1}{2}}, x_{i+\frac{1}{2}} \right] \times \left[y_{j-\frac{1}{2}}, y_{j+\frac{1}{2}} \right], \quad i = 1, \dots, M, j = 1, \dots, N, \quad (2.20)$$

with length $\Delta x := x_{i+\frac{1}{2}} - x_{i-\frac{1}{2}}$ and $\Delta y := y_{j+\frac{1}{2}} - y_{j-\frac{1}{2}}$. To discretise the time variable, we consider $0 = t^0 < t^1 < t^2 < \dots$ and define the length of the time step as $\Delta t := t^{n+1} - t^n$,

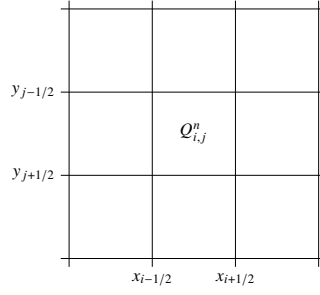


Figure 2.4.: Finite volume grid in two space dimensions, where $Q_{i,j}^n$ represents a cell average at time t^n . Compare with [56, chap. 19].

$\forall n \in \mathbb{N}_0$. We approximate the average value over the (i, j) -th grid cell at time t^n with

$$Q_{i,j}^n \approx \frac{1}{\Delta x \Delta y} \int_{y_{j-1/2}}^{y_{j+1/2}} \int_{x_{i-1/2}}^{x_{i+1/2}} q(x, y, t^n) dx dy = \frac{1}{\Delta x \Delta y} \int_{C_{i,j}} q(x, y, t^n) dx dy. \quad (2.21)$$

2.3.1 Finite Volume Method

As in section 2.2 for one space dimension, the multidimensional finite volume method is based on the integral form (2.2) of the conservation law and uses numerical fluxes at each cell edge to update the conserved quantity in each time step. The method has the form

$$Q_{i,j}^{n+1} = Q_{i,j}^n - \frac{\Delta t}{\Delta x} \left(F_{i+\frac{1}{2},j} - F_{i-\frac{1}{2},j} \right) - \frac{\Delta t}{\Delta y} \left(G_{i,j+\frac{1}{2}} - G_{i,j-\frac{1}{2}} \right),$$

where

$$F_{i-\frac{1}{2},j} \approx \frac{1}{\Delta t \Delta y} \int_{t^n}^{t^{n+1}} \int_{y_{j-1/2}}^{y_{j+1/2}} f(q(x_{i-1/2}, y, t)) dy dt,$$

$$G_{i,j-\frac{1}{2}} \approx \frac{1}{\Delta t \Delta x} \int_{t^n}^{t^{n+1}} \int_{x_{i-1/2}}^{x_{i+1/2}} g(q(x, y_{j-1/2}, t)) dx dt.$$

2.3.2 Godunov's Method

The idea of Godunov's Method in the multidimensional case is to solve Riemann problems normal to each cell edge. The one space dimensional method from subsection 2.2.2 is extended to

$$Q_{i,j}^{n+1} = Q_{i,j}^n - \frac{\Delta t}{\Delta x} \left(\mathcal{A}^+ \Delta Q_{i-\frac{1}{2},j} + \mathcal{A}^- \Delta Q_{i+\frac{1}{2},j} \right) - \frac{\Delta t}{\Delta y} \left(\mathcal{B}^+ \Delta Q_{i,j-\frac{1}{2}} + \mathcal{B}^- \Delta Q_{i,j+\frac{1}{2}} \right), \quad (2.22)$$

where

$$\mathcal{A}^{\pm} \Delta Q_{i-\frac{1}{2},j} = \sum_{p=1}^m (\lambda^p)^{\pm} \mathcal{W}_{i-\frac{1}{2},j}^p, \quad \mathcal{B}^{\pm} \Delta Q_{i,j-\frac{1}{2}} = \sum_{p=1}^m (\lambda^p)^{\pm} \mathcal{W}_{i,j-\frac{1}{2}}^p$$

represent the fluctuations resulting from solving Riemann problems in the x - and y -direction. For example, $\mathcal{B}^{\pm} \Delta Q_{i,j-\frac{1}{2}}$ results from the Riemann problem at the interface $(i, j - 1/2)$.

2.3.3 High-Resolution Wave Propagation

The multidimensional high-resolution Wave Propagation Algorithm for solving two-dimensional systems of hyperbolic conservation laws has the form

$$\begin{aligned} Q_{i,j}^{n+1} = Q_{i,j}^n & - \frac{\Delta t}{\Delta x} (\mathcal{A}^+ \Delta Q_{i-1/2,j} + \mathcal{A}^- \Delta Q_{i+1/2,j}) - \frac{\Delta t}{\Delta x} (\mathcal{B}^+ \Delta Q_{i,j-1/2} + \mathcal{B}^- \Delta Q_{i,j+1/2}) \\ & - \frac{\Delta t}{\Delta x} (\tilde{F}_{i+1/2,j} - \tilde{F}_{i-1/2,j}) - \frac{\Delta t}{\Delta x} (\tilde{G}_{i,j+1/2} - \tilde{G}_{i,j-1/2}). \end{aligned}$$

The fluxes \tilde{F} and \tilde{G} are included to extend the first order accurate Godunov method to a high-resolution method.

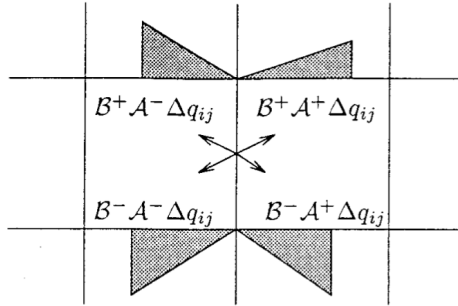


Figure 2.5.: Illustration of the four transverse flux differences for a general system of equations. Compare with [55].

As visualised in Figure 2.5, in the multidimensional high-resolution method each wave is assumed to potentially propagate transversely into each of the neighbouring cells. In the x -direction, this is described by decomposing the fluctuations $\mathcal{A}^+ \Delta Q_{i-1/2,j}$ into two transverse fluctuations

$$\mathcal{B}^{\pm} \mathcal{A}^+ \Delta Q_{i-1/2,j} = \sum_{p=1}^m (\lambda^{y,p})^{\pm} \beta^p r^{y,p},$$

which can be understood as solving Riemann problems in the transverse direction. Similarly,

$\mathcal{A}^- \Delta Q_{i-1/2,j}$ is split. We use the transverse fluctuations to update the correction fluxes \tilde{G}

$$\begin{aligned}\tilde{G}_{i,j\pm 1/2} &:= \tilde{G}_{i,j\pm 1/2} - \frac{\Delta t}{2\Delta x} \mathcal{B}^\pm \mathcal{A}^+ \Delta Q_{i-1/2,j}, \\ \tilde{G}_{i-1,j\pm 1/2} &:= \tilde{G}_{i-1,j\pm 1/2} - \frac{\Delta t}{2\Delta x} \mathcal{B}^\pm \mathcal{A}^- \Delta Q_{i-1/2,j},\end{aligned}\tag{2.23}$$

which are initialised as $\tilde{G}_{i,j\pm 1/2} = 0$ for all i, j at each step. Analogously, after solving Riemann problems in the y -direction at the interface $(i, j - 1/2)$, the fluctuation $\mathcal{B}^\pm \Delta Q_{i,j+1/2}$ is split to update the correction fluxes \tilde{F}

$$\begin{aligned}\tilde{F}_{i\pm 1/2,j} &:= \tilde{F}_{i\pm 1/2,j} - \frac{\Delta t}{2\Delta y} \mathcal{A}^\pm \mathcal{B}^+ \Delta Q_{i-1/2,j}, \\ \tilde{F}_{i\pm 1/2,j-1} &:= \tilde{F}_{i\pm 1/2,j-1} - \frac{\Delta t}{2\Delta y} \mathcal{A}^\pm \mathcal{B}^- \Delta Q_{i-1/2,j},\end{aligned}\tag{2.24}$$

which are initialised as $\tilde{F}_{i,j\pm 1/2} = 0$ for all i, j at each step. Second-order accuracy is achieved by adding second order flux corrections, analogous to (2.17), in each direction to the fluxes already defined in (2.24) and (2.23)

$$\begin{aligned}\tilde{F}_{i+1/2,j} &:= \tilde{F}_{i+1/2,j} + \frac{1}{2} \sum_{p=1}^m \left| \lambda_{i+1/2,j}^{x,p} \right| \left(1 - \frac{\Delta t}{\Delta x} \left| \lambda_{i+1/2,j}^{x,p} \right| \right) \tilde{W}_{i+1/2,j}^{x,p}, \\ \tilde{G}_{i,j+1/2} &:= \tilde{G}_{i,j+1/2} + \frac{1}{2} \sum_{p=1}^m \left| \lambda_{i,j+1/2}^{y,p} \right| \left(1 - \frac{\Delta t}{\Delta y} \left| \lambda_{i,j+1/2}^{y,p} \right| \right) \tilde{W}_{i,j+1/2}^{y,p}.\end{aligned}$$

As in one dimension in (2.18), the limiter $\tilde{W}_{i+1/2,j}^{x,p}$ compares $W_{i+1/2,j}^{x,p}$ with $W_{i-1/2,j}^{x,p}$ or $W_{i+3/2,j}^{x,p}$ depending on the sign of $\lambda_{i+1/2,j}^{x,p}$. Analogously for the limiter $\tilde{W}_{i,j+1/2}^{y,p}$. The CFL-condition for the multidimensional Wave Propagation Algorithm is defined by

$$\max \left(\lambda \frac{\Delta t}{\Delta x}, \mu \frac{\Delta t}{\Delta y} \right) \leq 1,$$

where λ and μ are the maximum wave speeds in the x - and y -direction.

2.9 Example. We briefly present the multidimensional high-resolution finite volume method for solving the two-dimensional scalar advection equation

$$q_t(x, y, t) + f(q(x, y, t))_x + g(q(x, y, t))_y = 0, \quad x, y \in \mathbb{R}, t > 0,$$

where $f(q(x, y, t))_x = uq_x(x, y, t)$ and $g(q(x, y, t))_y = vq_y(x, y, t)$ and u, v are constant in

space and time. As we have scalar values u, v , the fluctuations have the form

$$\mathcal{A}^\pm \Delta Q_{i-1/2,j} = u^\pm (Q_{ij} - Q_{i-1,j}),$$

$$\mathcal{B}^\pm \Delta Q_{i,j-1/2} = v^\pm (Q_{ij} - Q_{i,j-1}),$$

using $u^+ = \max(u, 0)$ and $u^- = \min(u, 0)$. The transverse fluctuations are defined as

$$\mathcal{B}^\pm \mathcal{A}^\pm \Delta Q_{i-1/2,j} = v^\pm u^\pm (Q_{ij} - Q_{i-1,j}),$$

$$\mathcal{A}^\pm \mathcal{B}^\pm \Delta Q_{i,j-1/2} = v^\pm u^\pm (Q_{ij} - Q_{i,j-1}).$$

The flux-difference formulation of the method, which combines the fluxes of the first-order accurate corner-transport (CTU) method by Colella [21] with the flux in (2.17) in x - and y -direction, can be found in [54].

2.10 Example. In case of an incompressible velocity field, the high-resolution finite volume method from Example 2.9 can be easily adjusted to solve the two-dimensional variable-coefficient scalar advection equation

$$q_t(x, y, t) + f(q(x, y, t))_x + g(q(x, y, t))_y = 0, \quad x, y \in \mathbb{R}, t > 0 \quad (2.25)$$

with $f(q(x, y, t)) = u(x, y, t)q(x, y, t)$ and $g(q(x, y, t)) = v(x, y, t)q(x, y, t)$. As we assume that the velocity field is incompressible, we have

$$u_x(x, y, t) + v_y(x, y, t) = 0 \quad \text{for all } x, y, t.$$

Hence, the conservative form (2.25) of the advection equation can be rewritten in the so-called advective form

$$q_t(x, y, t) + u(x, y)q_x(x, y, t) + v(x, y)q_y(x, y, t) = 0, \quad x, y \in \mathbb{R}, t > 0. \quad (2.26)$$

Mathematically, equations (2.26) and (2.25) are identically, but numerical methods based on the two behave differently. The approach to solve the conservative form (2.25) can be found in [56, chap. 9.3].

To compute the numerical solution of the advective form (2.26), we discretise the velocities (u, v) at the cell edges and the conserved quantity q in the middle of the cell. As visualised in Figure 2.6, the edge velocity $u_{i-1/2,j}$ is defined at the edge between cells $(i-1, j)$ and (i, j) and $v_{i,j-1/2}$ at the edge between cells $(i, j-1)$ and (i, j) . $Q_{i,j}$ is the average value over

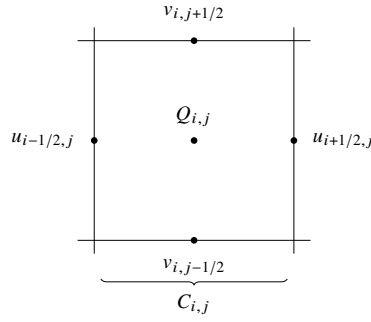


Figure 2.6.: The interface velocity values.

the grid cell (i, j) , defined as in (2.21). As an incompressible fluid is studied, the discrete velocity field should satisfy the discrete divergence-free relationship

$$\frac{u_{i+1/2,j} - u_{i-1/2,j}}{\Delta x} + \frac{v_{i,j+1/2} - v_{i,j-1/2}}{\Delta y} = 0. \quad (2.27)$$

Solving Riemann problems at each interface in the x - and y -direction results in the single waves

$$\mathcal{W}_{i-1/2,j} = Q_{ij} - Q_{i-1,j},$$

$$\mathcal{W}_{i,j-1/2} = Q_{ij} - Q_{i,j-1},$$

propagating with the edge velocity $u_{i-1/2,j}$ and $v_{i,j-1/2}$. The fluctuations are identical to the fluctuations in Example 2.9, only the constants u and v have to be replaced by u and v evaluated at the midpoint of the interface from which the wave propagates. For a more detailed presentation we refer to [56, chap. 20.5].

2.4 Operator Splitting for Handling Source Terms

So far, we have studied the numerical treatment of homogeneous conservation laws. Operator splitting methods allow to extend the numerical methods from the last sections to the more general balance laws of the form

$$q_t + f(q)_x = \psi(q), \quad (2.28)$$

where the homogeneous equation is hyperbolic in the sense of Definition 2.1. The idea is to split problem (2.28) into two subproblems of the form

$$\text{Problem A: } q_t + f(q)_x = 0,$$

$$\text{Problem B: } q_t = \psi(q),$$

and to alternate between solving subproblem A and B. As a consequence, the homogeneous equations in subproblem A can be solved with the finite volume methods from section 2.2 and the system of ordinary differential equations in subproblem B with a solver for ordinary differential equations. In the next two subsections, we will present different splitting methods.

2.4.1 Fractional-Step Method

The fractional-step method takes a time step of length Δt of subproblem A to calculate an intermediate value, which is used as initial data for calculating one time step of length Δt of subproblem B. This method is first-order accurate [56, chap. 17.5].

2.11 Example. *As an example we consider the two-dimensional variable-coefficient advection-diffusion equation, which was also analysed in [52]*

$$q_t(x, y, t) + (\mathbf{u}(x, y, t) \cdot \nabla)q(x, y, t) = \frac{1}{Re} \nabla^2 q(x, y, t), \quad (2.29)$$

where Re is a Reynolds number and $\mathbf{u} = (u, v)$. Equation (2.29) is discretised as in Example 2.10 and $\mathbf{u}^n = (u_{i\pm 1/2, j}^n, v_{i, j\pm 1/2}^n)$ satisfies the divergence-free condition (2.27). For the centered values Q^n and the edge values \mathbf{u}^n the semi-discrete form of equation (2.29) can be written as

$$\frac{Q^* - Q^n}{\Delta t} + (\mathbf{u}^n \cdot \nabla) Q^* = \frac{1}{2Re} (\Delta Q^* + \Delta Q^n). \quad (2.30)$$

For (2.30), the fractional-step method is given as

$$\frac{Q^\dagger - Q^n}{\Delta t} + (\mathbf{u}^n \cdot \nabla) Q^\dagger = 0, \quad (2.31)$$

$$\frac{Q^* - Q^\dagger}{\Delta t} = \frac{1}{2Re} (\Delta Q^* + \Delta Q^\dagger). \quad (2.32)$$

Q^\dagger in (2.31) is computed with a high-resolution finite volume method as presented in Example 2.10. Equation (2.32) is equivalent to the Crank-Nicolson discretisation for diffusion.

2.4.2 Strang Splitting

The approach of Strang splitting [81] is to solve subproblem A over a half time step of length $\Delta t/2$. The resulting solution is used as initial data for calculating a full time step Δt on subproblem B. Finally, a second half time step of length $\Delta t/2$ is taken on subproblem A.

Provided that each problem is solved with a second-order accurate method, Strang splitting is of second order [56, chap. 17.5].

2.12 Example. *Again, we consider the advection-diffusion equation (2.29) which is discretised as in (2.30). Strang splitting has the following steps*

$$\begin{aligned}\frac{Q^\dagger - Q^n}{\Delta t/2} &= \frac{1}{2Re} (\Delta Q^\dagger + \Delta Q^n), \\ \frac{Q^{\dagger\dagger} - Q^\dagger}{\Delta t} + (u^n \cdot \nabla) Q^{\dagger\dagger} &= 0, \\ \frac{Q^* - Q^{\dagger\dagger}}{\Delta t/2} &= \frac{1}{2Re} (\Delta Q^* + \Delta Q^{\dagger\dagger}).\end{aligned}$$

2.5 Projection Method for the Two-Dimensional Navier-Stokes Equation

The aim of this section is to study a numerical method for solving the incompressible Navier-Stokes equation in two space-dimensions

$$\begin{aligned}(\partial_t u + u \partial_x u + v \partial_y u) + p_x &= \frac{1}{Re} (u_{xx} + u_{yy}) + F_1, \\ (\partial_t v + u \partial_x v + v \partial_y v) + p_y &= \frac{1}{Re} (v_{xx} + v_{yy}) + F_2, \\ u_x + v_y &= 0, \\ u = b_1, \quad v = b_2 &\quad \text{on } \partial\Omega,\end{aligned}\tag{2.33}$$

where Re is a Reynolds number and F_1, F_2 represent an external force. We present a projection method by Long Lee [52] which fits well into the multidimensional wave propagation concept by LeVeque.

Originally, the idea of solving the Navier-Stokes equation with a projection method was introduced by Chorin in [17], [18], [19] in order to decouple the computation of the velocity and pressure field. This first order fractional-step method calculates first an intermediate velocity disregarding the incompressibility constraint, which is then projected onto a divergence-free subspace.

Comparable to the projection methods by Bell, Colella and Glaz [8] or by Kim and Moin [47], the presented method first ignores the pressure gradient and advects and diffuses the

cell-centered velocity with a high-resolution finite volume method by LeVeque [55] and a finite difference method, and then projects this velocity onto the divergence-free subspace by solving a Poisson pressure equation.

The two-dimensional spatial domain Ω and the time variable are discretised in the same ways as already presented in section 2.3. The grid cells have the same definition as in (2.20).

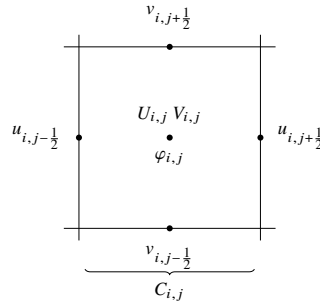


Figure 2.7.: Variables of the projection method for the Navier-Stokes equation (2.33).

As shown in Figure 2.7, the divergence-free velocity field (u, v) in the two-dimensional Navier-Stokes equation is discretised on a staggered grid. While $(U_{i,j}^n, V_{i,j}^n)$ is defined at the cell center of $C_{i,j}$, the horizontal and vertical components of the discrete edge velocity field $(u_{i\pm 1/2,j}^n, v_{i,j\pm 1/2}^n)$ are defined at the midpoints of the interfaces $(x_{i\pm 1/2}, y_j)$ and $(x_i, y_{j\pm 1/2})$ of the cell $C_{i,j}$. We compute the cell average $\mathbf{U}_{i,j}^n = (U_{i,j}^n, V_{i,j}^n)$ over the (i, j) -th grid cell at time t^n as

$$\mathbf{U}_{i,j}^n \approx \frac{1}{\Delta x \Delta y} \int_{C_{i,j}} \mathbf{u}(x, y, t^n) dx dy. \quad (2.34)$$

The discrete edge velocity is calculated by taking the average of the cell-centered values. For example, the left edge value of cell $C_{i,j}$ is

$$u_{i-1/2,j}^n = \frac{1}{2} (U_{i-1,j}^n + U_{i,j}^n). \quad (2.35)$$

We assume that the discrete velocity field satisfies the discrete divergence-free relationship, defined in (2.27). We define the discrete gradient and divergence operators on the staggered grid as follows

$$\begin{aligned} (\mathcal{D}\mathbf{u})_{i,j} &= \frac{u_{i+1/2,j} - u_{i-1/2,j}}{\Delta x} + \frac{v_{i,j+1/2} - v_{i,j-1/2}}{\Delta y}, \\ (\mathcal{G}\varphi)_{i,j} &= \left(\frac{\varphi_{i,j} - \varphi_{i-1,j}}{\Delta x}, \frac{\varphi_{i,j} - \varphi_{i,j-1}}{\Delta y} \right), \end{aligned} \quad (2.36)$$

$$\begin{aligned} (\mathcal{D}^\circ \mathbf{U})_{i,j} &= \frac{U_{i+1,j} - U_{i-1,j}}{2\Delta x} + \frac{V_{i,j+1} - V_{i,j-1}}{2\Delta y}, \\ (\mathcal{G}^\circ \varphi)_{i,j} &= \left(\frac{\varphi_{i+1,j} - \varphi_{i-1,j}}{2\Delta x}, \frac{\varphi_{i,j+1} - \varphi_{i,j-1}}{2\Delta y} \right), \end{aligned}$$

where φ is a scalar function.

The projection method by Long Lee [52] for solving an incompressible Navier-Stokes equation is an operator splitting method which splits the process of solving (2.33) in a transport- and projection step. To be precise, the algorithm has the following steps.

Step 1: In the transport step, we solve the advection-diffusion equation

$$\mathbf{u}_t + (\mathbf{u} \cdot \nabla) \mathbf{u} = \frac{1}{Re} \nabla^2 \mathbf{u} + \mathbf{F}, \quad (2.37)$$

with $\mathbf{u} = (u, v)$ and $\mathbf{F} = (F_1, F_2)$ over a time step of length Δt . Just like in Example 2.12, we consider the centered values $\mathbf{U}_{i,j}^n = (U_{i,j}^n, V_{i,j}^n)$ and the edge values $\mathbf{u}^n = (u_{i\pm 1/2,j}^n, v_{i,j\pm 1/2}^n)$ and use Strang splitting to compute the intermediate velocity field $\mathbf{U}_{i,j}^* = (U_{i,j}^*, V_{i,j}^*)$.

Step 2: We average the discrete centered values to get the edge values

$$\begin{aligned} u_{i-1/2,j}^* &= \frac{1}{2} (U_{i-1,j}^* + U_{i,j}^*), \\ v_{i,j-1/2}^* &= \frac{1}{2} (V_{i,j-1}^* + V_{i,j}^*). \end{aligned}$$

Step 3: In the projection step, we incorporate

$$\mathbf{u}_t = -\nabla p$$

and incompressibility of the velocity field. Therefore, we update \mathbf{U}^* to \mathbf{U}^{n+1} by

$$\mathbf{U}^{n+1} = \mathbf{U}^* - \Delta t \nabla \varphi^{n+1}. \quad (2.38)$$

Then, the pressure p^{n+1} can be obtained from φ^{n+1} through the relationship [10]

$$p^{n+1} = \varphi^{n+1} - \frac{\Delta t}{2Re} \nabla^2 \varphi^{n+1}.$$

To compute φ^{n+1} , the divergence operator $\nabla \cdot$ is applied to (2.38) and the incompressibility of the velocity field (2.27) is considered, which results in the

Poisson equation

$$\nabla^2 \varphi^{n+1} = \frac{\nabla \cdot \mathbf{u}^*}{\Delta t}. \quad (2.39)$$

The discrete version of (2.39) has the form

$$\mathcal{D}\mathcal{G}(\Delta t \varphi)_{i,j}^{n+1} = \mathcal{D}\mathbf{u}_{i,j}^*, \quad (2.40)$$

where the operator \mathcal{D} is defined as in (2.36) and $\mathcal{D}\mathcal{G}$ is a compact five-point Laplacian operator. The discrete Poisson equation (2.40) with Neumann boundary conditions is solved for φ with the fast fourier transformation algorithm.

- (a): Update of the interface values: Let $\mathcal{G}(\Delta t \varphi)_{i,j}^{n+1} = (\mathcal{G}_{1,(i,j)}, \mathcal{G}_{2,(i,j)})$. To compute divergence-free interface values, we update the interface values by

$$\begin{aligned} u_{i-1/2,j}^{n+1} &= u_{i-1/2,j}^* - \mathcal{G}_{1,(i,j)}, \\ v_{i,j-1/2}^{n+1} &= v_{i,j-1/2}^* - \mathcal{G}_{2,(i,j)}. \end{aligned}$$

- (b): Update of the cell-centered values: Let $\mathcal{G}^\circ(\Delta t \varphi)_{i,j}^{n+1} = (\mathcal{G}_{1,(i,j)}^\circ, \mathcal{G}_{2,(i,j)}^\circ)$. We update the cell-centered values by

$$\begin{aligned} U_{i,j}^{n+1} &= U_{i,j}^* - \mathcal{G}_{1,(i,j)}^\circ, \\ V_{i,j}^{n+1} &= V_{i,j}^* - \mathcal{G}_{2,(i,j)}^\circ. \end{aligned}$$

The method is second order accurate and stable up to the following CLF-condition, see [52]

$$\max_{i,j} \left(\frac{\Delta t}{\Delta x} |u_{i-1/2,j}|, \frac{\Delta t}{\Delta y} |v_{i,j-1/2}| \right) \leq 1.$$

Multiscale Models for Sedimentation of Rod-Like Particles

The starting point of our considerations is a coupled system of partial differential equations describing sedimentation in dilute suspensions of rod-like particles under the influence of gravity on a mesoscopic level. The mathematical model was derived by Helzel and Tzavaras [35], and is based on the coupling of a Smoluchowski equation to the Navier-Stokes equation. Kinetic models of this type were established by Doi and Edwards [25, chap. 8].

The chapter is organised as follows: In section 3.1, the general model for the description of the sedimentation process in suspensions of rod-like particles is presented. Subsequently, we derive lower dimensional simplifications for a two-dimensional flow in section 3.2 and a shear flow in section 3.3.

Similar to [24, section 2], the purpose of this chapter is to give a brief review of the mathematical model derived by Helzel and Tzavaras in order to ensure a basic understanding of the various components of the system. For a derivation of the model and more details the reader is referred to [32], [35], [68].

3.1 General Model

The general model by Helzel and Tzavaras [35] describes the sedimentation process in suspensions under the influence of gravity.

The first assumption of the model is the rigid rod-like structure of the particles. To guarantee a slender rod-like shape, the thickness b of the particles is assumed to be much smaller than their length l . In addition, a dilute regime is considered (see Figure 1.1). The characteristic feature of a dilute suspension is that the concentration of the particles is at such a low level that the average distance between the particles is much larger than the length l of the rods. Mathematically, this is described by $\nu l^3 < 1$, where ν is the number density of the rods. An

important assumption is that the density ν is not constant in time and space so that clusters are allowed to form.

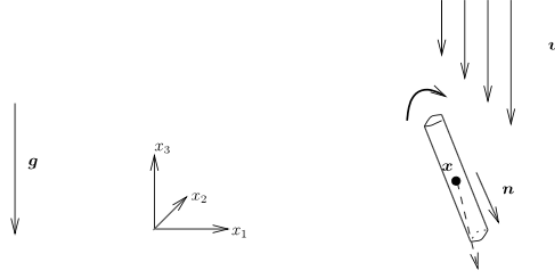


Figure 3.1.: Basic notation for a rod-like molecule which is falling sideways, see [35].

In a macroscopic physical space $\Omega \subset \mathbb{R}^d$ with spatial dimension d , the probability distribution function $f = f(t, \mathbf{x}, \mathbf{n})$ models the time-dependent probability that a particle with orientation $\mathbf{n} \in S^{d-1}$, where S^{d-1} is the unit sphere embedded in \mathbb{R}^d , has a center of mass at position $\mathbf{x} \in \mathbb{R}^d$. As visualised in Figure 3.1, the distribution of the particles is influenced by a solvent with a macroscopic velocity field $\mathbf{u}(\mathbf{x}, t)$ and pressure $p = p(t, \mathbf{x})$. A further influential factor for the rod distribution is the acceleration of gravity, which acts in the direction of \mathbf{e}_3 , where \mathbf{e}_3 is the unit vector in the upward direction.

The interaction of the rod-like particles and the fluid in the sedimentation process in dilute suspensions under the influence of gravity is modelled by a system of partial differential equations which couples a Smoluchowski equation to an incompressible Navier-Stokes equation. In non-dimensional form, the model is given as

$$\begin{aligned}
 \partial_t f + \nabla_x \cdot (\mathbf{u}f) + \nabla_n \cdot (P_{n^\perp} \nabla_x \mathbf{u} n f) - \nabla_x \cdot ((I + \mathbf{n} \otimes \mathbf{n}) \mathbf{e}_3 f) \\
 = D_r \Delta_n f + \gamma \nabla_x \cdot (I + \mathbf{n} \otimes \mathbf{n}) \nabla_x f, \\
 \sigma = \int_{S^{d-1}} (d\mathbf{n} \otimes \mathbf{n} - I) f d\mathbf{n}, \\
 Re (\partial_t \mathbf{u} + (\mathbf{u} \cdot \nabla_x) \mathbf{u}) = \Delta_x \mathbf{u} - \nabla_x p + \delta \gamma \nabla_x \cdot \sigma - \delta \int_{S^{d-1}} f d\mathbf{n} \mathbf{e}_3, \\
 \nabla_x \cdot \mathbf{u} = 0.
 \end{aligned} \tag{3.1}$$

We give a brief explanation of the meaning of the different terms in model (3.1).

The equation in the first line of (3.1) is known as a Smoluchowski equation. The second and fourth term in the first line describe the transport of the center of mass of the particles due to the macroscopic velocity \mathbf{u} and gravity. The third term models the rotation of the axis of

the particles due to a macroscopic velocity gradient $\nabla_x \mathbf{u}$, where $P_{n^\perp} \nabla_x \mathbf{u} \mathbf{n}$ is the orthogonal projection of the vector $\nabla_x \mathbf{u}$ onto the tangent space in \mathbf{n} . On the right hand side of the first equation, rotational and translational diffusion are described.

The macroscopic dynamic of an incompressible fluid is described by a Navier-Stokes equation in the third line. The velocity gradient $\nabla_x \mathbf{u}$ in the Navier-Stokes equation distorts an initial isotropic distribution of the particles and results in an increase in entropy. According to [25, Sec. 8.6], thermodynamic consistency requires that this is balanced by a stress tensor $\sigma(x, t)$. This stress tensor is added in the macroscopic Navier-Stokes equation. In addition, the Navier-Stokes equation is extended by a term that describes the buoyancy of the rods.

The full model (3.1) uses four non-dimensional parameters. Re is a Reynolds number based on the sedimentation velocity. D_r is a rotational diffusion coefficient. The parameter δ measures the relative importance of buoyancy versus viscous stress. γ measures the relative importance of elastic forces over buoyancy forces. We will restrict our attention to the case $\gamma = 0$ in which the effects of translational Brownian motion of the rod-like particles are ignored. As a consequence, the effect of elastic forces in the flow equation is negligible compared to the buoyancy forces.

Physical applications of the model assume a three-dimensional physical space $\Omega \subset \mathbb{R}^3$ in which the orientation of the particles is characterised by a director $\mathbf{n} \in S^2$. In this case, the full model is a time-dependent, five dimensional system of a three dimensional flow equation and a transport diffusion equation on the sphere.

3.2 Simplified Model for Two-Dimensional Flow

In this section, a lower-dimensional simplification of the general model (3.1) is achieved by restricting the considerations to a two-dimensional flow problem. In this case, we consider a velocity field of the form

$$\mathbf{u}(t, \mathbf{x}) = \begin{pmatrix} u(t, \mathbf{x}) \\ 0 \\ w(t, \mathbf{x}) \end{pmatrix}, \quad \mathbf{x} = \begin{pmatrix} x \\ 0 \\ z \end{pmatrix},$$

i.e. the velocity field varies only in the plane spanned by the x -direction and the z -direction, which is the direction of gravity. A further simplification, which was also considered in [35], is to characterise the orientation of the rod-like particles by a director $\mathbf{n} \in S^1$, which is the

sphere embedded in the (x, z) -plane. We use the following notation

$$\mathbf{n}(\theta) = \begin{pmatrix} \cos \theta \\ 0 \\ \sin \theta \end{pmatrix} \in S^1,$$

where the angle $\theta \in [0, 2\pi]$ is measured counter-clockwise from the positive x -axis. Considering these simplifications, $f = f(t, x, z, \theta)$ describes the distribution of the particles as a function of time t , space $(x, z) \in \mathbb{R}^2$ and orientation $\theta \in [0, 2\pi]$. The drift term on the sphere simplifies to

$$P_{n^\perp} \nabla_x \mathbf{u} \mathbf{n} = \begin{pmatrix} -\sin \theta \\ 0 \\ \cos \theta \end{pmatrix} \cdot \begin{pmatrix} u_x & 0 & u_z \\ 0 & 0 & 0 \\ w_x & 0 & w_z \end{pmatrix} \begin{pmatrix} \cos \theta \\ 0 \\ \sin \theta \end{pmatrix} f = (w_z - u_x) \cos \theta \sin \theta - u_z \sin^2 \theta + w_x \cos^2 \theta.$$

The Laplace-Beltrami operator on S^1 is given as $\Delta_{\mathbf{n}} f = \partial_{\theta\theta} f$. The equation describing the transport of the centers of mass of the particles due to gravity has the form

$$\begin{aligned} \nabla_x \cdot ((I + \mathbf{n} \otimes \mathbf{n}) \mathbf{e}_3 f) &= \nabla_x \cdot \left(\begin{pmatrix} (1 + \cos^2 \theta) & 0 & \sin \theta \cos \theta \\ 0 & 1 & 0 \\ \sin \theta \cos \theta & 0 & 1 + \sin^2 \theta \end{pmatrix} \begin{pmatrix} 0 \\ 0 \\ 1 \end{pmatrix} f \right) \\ &= \partial_x (\sin \theta \cos \theta f) + \partial_z ((1 + \sin^2 \theta) f). \end{aligned}$$

For $\gamma = 0$, the general model (3.1) reduces to a two-dimensional system of the form

$$\begin{aligned} \partial_t f + \partial_\theta \left((w_z - u_x) \cos \theta \sin \theta - u_z \sin^2 \theta + w_x \cos^2 \theta \right) f \\ + \partial_x ((u - \cos \theta \sin \theta) f) + \partial_z \left(w - (1 + \sin^2 \theta) f \right) &= D_r \partial_{\theta\theta} f, \\ \text{Re} (\partial_t u + u \partial_x u + w \partial_z u) + p_x &= u_{xx} + u_{zz}, \\ \text{Re} (\partial_t w + u \partial_x w + w \partial_z w) + p_z &= w_{xx} + w_{zz} - \delta \int_0^{2\pi} f d\theta, \\ u_x + w_z &= 0. \end{aligned} \tag{3.2}$$

3.3 Simplified Model for Shear Flow

An even lower dimensional simplification of model (3.1) results from considering rod-like particles on S^1 in a shear flow. Using the ansatz of shear flow in vertical direction, we define

$$f = f(t, x, \theta), \quad \mathbf{u} = \begin{pmatrix} 0 \\ 0 \\ w(t, x) \end{pmatrix}.$$

In this case, the drift term on the sphere reduces to

$$P_{n^\perp} \nabla_x \mathbf{u}_{ext} n = w_x \cos^2 \theta.$$

The spatial transport in x is given as

$$\nabla_x \cdot ((I + \mathbf{n} \otimes \mathbf{n}) \mathbf{e}_3 f) = \partial_x (\sin \theta \cos \theta f).$$

For shear flow, the pressure is given as $p = -\kappa(t)z$, where $\kappa(t)$ can account for an externally imposed pressure gradient. As in [35], we define an equilibrated flow with $\kappa = \delta \bar{\rho}$, where $\bar{\rho}$ describes the total mass of suspended rods. In case of periodic boundary conditions, the total density is constant in time, i.e.

$$\bar{\rho} = \frac{1}{|\Omega|} \int_{\Omega} \int_0^{2\pi} f(t, x, \theta) d\theta = \frac{1}{|\Omega|} \int_{\Omega} \int_0^{2\pi} f(0, x, \theta) d\theta.$$

Using again $\gamma = 0$, model (3.1) reduces to the coupled system

$$\begin{aligned} \partial_t f + \partial_\theta (w_x \cos^2 \theta f) - \partial_x (\sin \theta \cos \theta f) &= D_r \partial_{\theta\theta} f, \\ Re \partial_t w &= \partial_{xx} w + \delta \left(\bar{\rho} - \int_0^{2\pi} f d\theta \right). \end{aligned} \quad (3.3)$$

A Detailed Numerical Method for the Coupled System

In this chapter, we describe a direct numerical method for the high-dimensional coupled systems (3.3) and (3.2). The direct numerical method uses an operator splitting approach which, during each time step, separately computes the evolution of f and the evolution of the velocity field. The goal of this chapter is to demonstrate that the direct method is cumbersome due to the high dimensionality of f and therefore a more efficient computation of f is essential.

The chapter is structured as follows. The detailed numerical method for the coupled shear flow problem (3.3) and the coupled two-dimensional flow problem (3.2) is described separately in section 4.1 and section 4.2. In section 4.3, the transfer between different degrees of freedom necessary to compute the evolution of f is presented.

The chapter is adapted from [24, section 3] and presented in more detail.

4.1 A Detailed Numerical Method for Shear Flow

This section deals with the description of the detailed numerical method for the coupled shear flow problem (3.3).

The numerical solution of the detailed model (3.3) can be computed by separately solving the evolution equation of f , which is a time-dependant partial differential equation in space and orientation and the evolution of the velocity field, which is a diffusion equation. The diffusion equation in model (3.3) can be solved with a Crank-Nicolson method for periodic boundary conditions (see equation 2.32). The evolution of f in (3.3) can be split into two subproblems, which have to be solved consecutively during each time step.

(1) For each $x_i, i = 1, \dots, n$, solve the drift diffusion equation on S^1

$$\partial_t f + \partial_\theta \left(w_x \cos^2 \theta f \right) = D_r \partial_{\theta\theta} f \quad (4.1)$$

with the spectral method.

(2) For each $\theta_k \in [0, 2\pi], k = 1, \dots, n$, solve the advection equation

$$\partial_t f + \partial_x (\cos \theta \sin \theta f) = 0 \quad (4.2)$$

with the one-dimensional high-resolution Wave Propagation Algorithm.

In the following subsections, we describe the methods for the two subproblems in detail.

4.1.1 Spectral Method for the Drift-Diffusion Equation

In this subsection, we solve the drift-diffusion equation (4.1) with the spectral method presented in [33]. Therefore, we assume that the components of the velocity gradient are constant and externally imposed at a given point \bar{x} . The spectral method is based on the ansatz

$$f(\bar{x}, t, \theta) = f_0(\bar{x}, t) + \sum_{i=1}^N c_i(\bar{x}, t) \cos(2i\theta) + s_i(\bar{x}, t) \sin(2i\theta). \quad (4.3)$$

We suppress the dependence on \bar{x} in the remainder of this subsection to simplify the notation. Calculating the derivatives of ansatz (4.3) leads to

$$\begin{aligned} \partial_t f(t, \theta) &\approx f'_0(t) + \sum_{i=1}^N c'_i(t) \cos 2i\theta + s'_i(t) \sin 2i\theta, \\ \partial_\theta f(t, \theta) &\approx \sum_{i=1}^N -2ic_i(t) \sin 2i\theta + 2is_i(t) \cos 2i\theta, \\ \partial_{\theta\theta} f(t, \theta) &\approx \sum_{i=1}^N -4i^2 c_i(t) \cos 2i\theta - 4i^2 s_i(t) \sin 2i\theta. \end{aligned} \quad (4.4)$$

We insert the ansatz (4.3) and the derivatives (4.4) into

$$\partial_t f(t, \theta) = w_x \sin(2\theta) f(t, \theta) - \frac{1}{2} (w_x + w_x \cos 2\theta) \partial_\theta f + D_r \partial_{\theta\theta} f,$$

which is an equivalent representation of (4.1). Using Product-to-Sum Formulas results in

$$\begin{aligned}
 & f'_0(t) + \sum_{i=1}^N c'_i(t) \cos(2i\theta) + s'_i(t) \sin(2i\theta) \\
 &= w_x \sin 2\theta f_0(t) + \frac{1}{2} w_x \sum_{i=1}^N c_i(t) (\sin(2(i+1)\theta) - \sin(2(i-1)\theta)) \\
 &+ \frac{1}{2} w_x \sum_{i=1}^N s_i(t) (\cos(2(i-1)\theta) - \cos(2(i+1)\theta)) \\
 &- w_x \sum_{i=1}^N s_i(t) (-i c_i(t) \sin(2i\theta) + i s_i(t) \cos(2i\theta)) \\
 &+ \frac{1}{2} w_x \sum_{i=1}^N i c_i(t) (\sin(2(i+1)\theta) + \sin(2(i-1)\theta)) \\
 &- \frac{1}{2} w_x \sum_{i=1}^N i s_i(t) (\cos(2(i-1)\theta) + \cos(2(i+1)\theta)) \\
 &- 4D_r \sum_{i=1}^N \left(i^2 c_i(t) \cos(2i\theta) + i^2 s_i(t) \sin(2i\theta) \right).
 \end{aligned}$$

Grouping terms of different order in cosine and sine leads to

$$\begin{aligned}
 1 & : f'_0(t) = 0, \\
 \cos(2\theta) & : c'_1(t) = -w_x s_1(t) - 4D_r c_1(t) - \frac{1}{2} w_x s_2(t), \\
 \sin(2\theta) & : s'_1(t) = w_x f_0(t) + w_x c_1(t) - 4D_r s_1(t) + \frac{1}{2} w_x c_2(t), \\
 \cos(2j\theta) & : c'_j(t) = -4D_r j^2 c_j(t) - \frac{j}{2} w_x (s_{j-1}(t) + s_{j+1}(t)) - j w_x s_j(t), \quad j = 2, \dots, N, \\
 \sin(2j\theta) & : s'_j(t) = \frac{j}{2} w_x (c_{j-1}(t) + c_{j+1}(t)) + j w_x c_j(t) - 4D_r j^2 s_j(t), \quad j = 2, \dots, N.
 \end{aligned} \tag{4.5}$$

The equations for c_N and s_N contain terms involving c_{N+1} and s_{N+1} , for which no evolution equations are supplied. For practical computations, the system needs to be closed. In Figure 4.1, we plot $\max\{|s_i|, |c_i|\}$ versus i for the spectral representation of f in the steady state approximation for shear flow for different values of $|w_x/D_r|$. As the magnitude of the coefficients of the spectral method decreases with increasing i , a reasonable closure can be based on the assumption that higher order modes in the representation of the solution of (4.1) decay faster than lower order modes. Thus, we set $c_{N+1} = s_{N+1} = 0$ to close the system.

In [33], a matrix-vector notation of the ordinary differential equations (4.5) is presented. The system of ordinary differential equations of the form $\partial_t q(t) = Dq(t)$ with the unknown

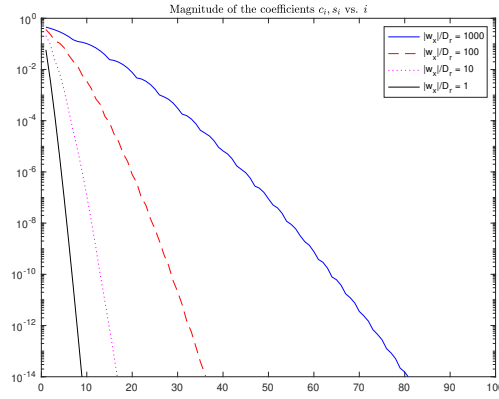


Figure 4.1.: Modulus of coefficients c_i, s_i versus i for the spectral representation of f in the steady state approximation for shear flow with different values of $|w_x|/D_r$.

coefficient vector $q(t) = (f_0(t), c_1(t), s_1(t), \dots, c_N(t), s_N(t))^T$ and $D \in \mathbb{R}^{(2N+1) \times (2N+1)}$ can be solved using a standard high-order accurate time stepping method.

In the remainder of the subsection, we analyse how many modes in the spectral method are needed to resolve the solution structure of (4.1). We also study the impact of the value $|w_x|/D_r$ on the accuracy of the spectral method.

4.1 Example. We consider (4.1) for externally imposed shear flow with $w_x = 1$ and different values for D_r . After some time, the exact solution of (4.1) attains a steady state which we compute with the spectral method using different numbers of modes, i.e. different values of N . In the simplest case $N = 1$, the spectral method for externally imposed shear flow results in a system of ordinary differential equations of the form

$$\partial_t \begin{pmatrix} f_0(t) \\ c_1(t) \\ s_1(t) \end{pmatrix} = \begin{pmatrix} 0 & 0 & 0 \\ 0 & -4D_r & -w_x \\ w_x & w_x & -4D_r \end{pmatrix} \begin{pmatrix} f_0(t) \\ c_1(t) \\ s_1(t) \end{pmatrix}.$$

In Figure 4.2 - Figure 4.4, we consider the approximation of the steady state of the exact solution of (4.1) for externally imposed shear flow in Example 4.1. We plot the numerical solution over the unit sphere. As a reference solution we use the solution obtained with the spectral method for $N = 50$.

In Figure 4.2, we show numerical solutions of f for $D_r = 0.1$. For $N = 3$ the solution structure compares well with the structure obtained using $N = 50$, indicating that the solution

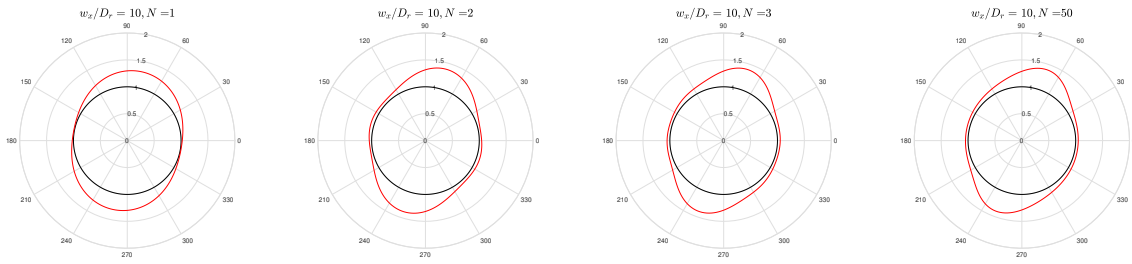


Figure 4.2.: Approximations of steady state solutions of f for externally imposed shear flow with $w_x/D_r = 10$ and different values of N .

is well resolved.

In Figure 4.3, the case $D_r = 0.01$ is considered. The numerical solution obtained with $N = 1$ already shows the general trend of the alignment, but the solution structure is not fully resolved. For $N = 3$, the approximation leads to negative values of f which are unphysical. We can eliminate the unphysical behaviour of the numerical solution of f by increasing the number of modes. A spectral method using $N = 8$ modes accurately approximates the reference solution, indicating that the numerical solution is well resolved.

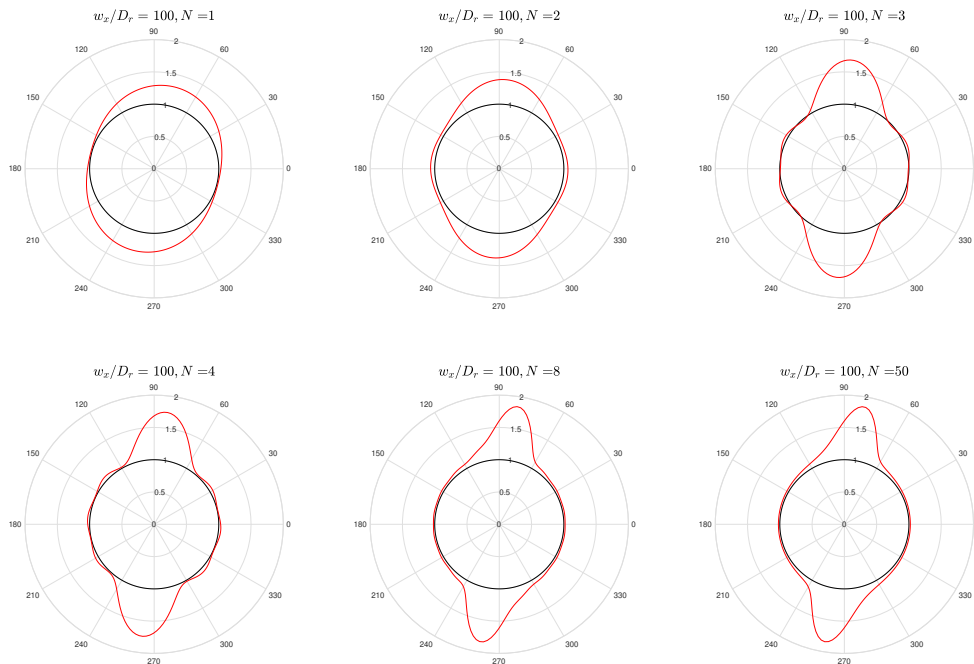


Figure 4.3.: Approximations of steady state solutions of f for externally imposed shear flow with $|w_x|/D_r = 100$ and different values of N .

In Figure 4.4, the approximation of the steady state solutions of f for externally imposed

shear flow with $w_x/D_r = 1000$ and different values of N is presented. In this case, $N = 19$ modes are necessary so that the solution structure compares well with the reference solution.

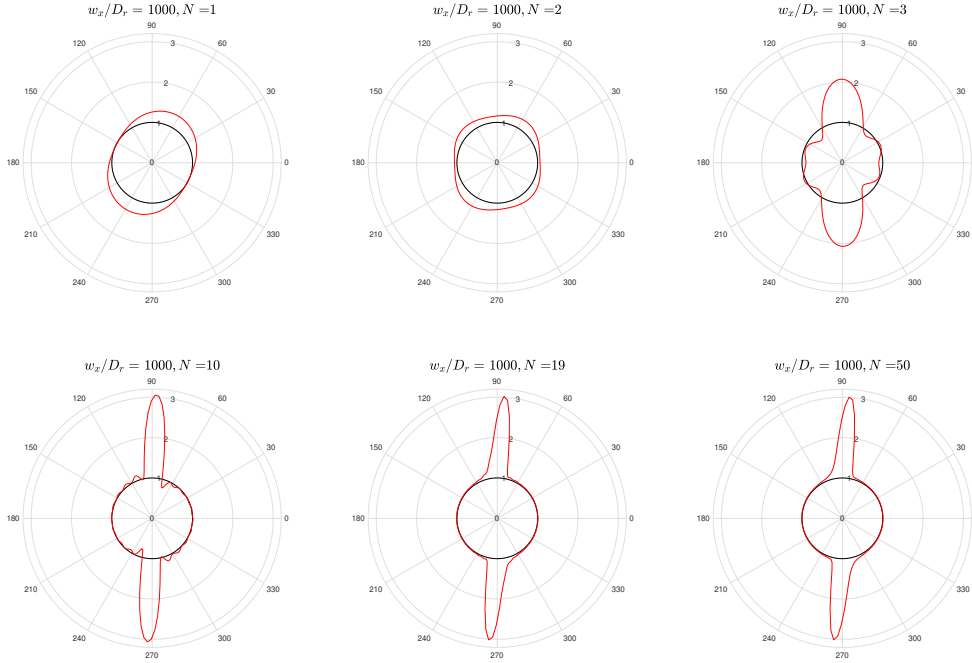


Figure 4.4.: Approximations of steady state solutions of f for externally imposed shear flow with $w_x/D_r = 1000$ and different values of N .

We can summarise that in a diffusion dominated regime of small $|w_x|/D_r$ fewer modes are needed to resolve the solution structure than in a drift dominated regime of large $|w_x|/D_r$. The reason for that can be found in Figure 4.1. The figure shows that in a diffusion dominated regime of small $|w_x|/D_r$ the coefficients of the spectral method decrease faster than in a drift dominated regime of large $|w_x|/D_r$. Thus, the larger $|w_x|/D_r$ the more modes are needed to find a good numerical approximation of f .

The non-physical oscillations in a drift dominated regime of large $|w_x|/D_r$ happen because the coefficients in the spectral method decay too slowly (compare with Figure 4.1). In the following subsection, we give a brief outlook to filtered spectral methods that preserve the positivity of the numerical solution as their coefficients decay faster.

4.1.2 Outlook: Filtered Spectral Method for the Drift-Diffusion Equation

In this subsection, at the suggestion of Jennifer K. Ryan, we approximate the steady state of the exact solution of the drift-diffusion equation (4.1) for externally imposed shear flow with the filtered spectral method.

To derive the filtered spectral method we make an ansatz of the form

$$f(\bar{x}, t, \theta) = f_0(\bar{x}, t)\sigma(0) + \sum_{i=1}^N c_i(\bar{x}, t) \cos(2i\theta)\sigma\left(\frac{i}{N}\right) + s_i(\bar{x}, t) \sin(2i\theta)\sigma\left(\frac{i}{N}\right),$$

where the function σ represents a filter.

4.2 Definition. A filter of order q is a real and even function $\sigma(\eta) \in C^{q-1}[-\infty, \infty]$ with the following properties (see [85])

$$\begin{aligned} \sigma(\eta) &= 0, & |\eta| &\geq 1, \\ \sigma(0) &= 1, \\ \sigma^{(m)}(0) &= \sigma^{(m)}(1) = 0, & m &= 1, 2, \dots, q-1. \end{aligned}$$

A detailed introduction to filters can be found in [38] and [85]. We list some common filters.

- Cesár filter:

$$\sigma(\eta) = 1 - \eta$$

- Lanczos filter [85]:

$$\sigma(\eta) = \frac{\sin(\pi\eta)}{\pi\eta}$$

- Exponential filter [85]:

$$\sigma(\eta) = \begin{cases} 1, & |\eta| \leq \eta_c, \\ \exp\left(-\alpha \left(\frac{\eta - \eta_c}{1 - \eta_c}\right)^p\right), & |\eta| \geq \eta_c, \end{cases}$$

where α measures how strongly the solution is filtered and η_c is the threshold of the filter. This filter will lead to p^{th} order convergence in smooth regions.

- Smoothness-Increasing Accuracy-Conserving (SIAC) filter [74], [43]:

$$\sigma(\eta) = \left(\frac{\sin(\frac{\eta}{2})}{\frac{\eta}{2}} \right)^{k+1} \left(c_0 + 2 \sum_{\gamma=1}^k c_\gamma^{2(k+1),k+1} \cos(\gamma\eta) \right),$$

where $c_\gamma^{2(k+1),k+1}$ are weights of B-splines, $\psi^{(k+1)}$, and are determined by

$$\sum_{\gamma=0}^{2k} c_\gamma \int_{-\infty}^{\infty} \psi^{(k+1)}(x)(x+x_\gamma)^m dx = \begin{cases} 1, & m = 0, \\ 0, & m = 1, \dots, 2k. \end{cases}$$

x_γ depends on the point being post-processed. We refer to [44], [75], [76] for more details on the SIAC filter.

4.3 Example. We consider (4.1) for externally imposed shear flow with $w_x = 1$ and different values for D_r . We compute the steady state of the exact solution of (4.1) with the spectral method using different filters.

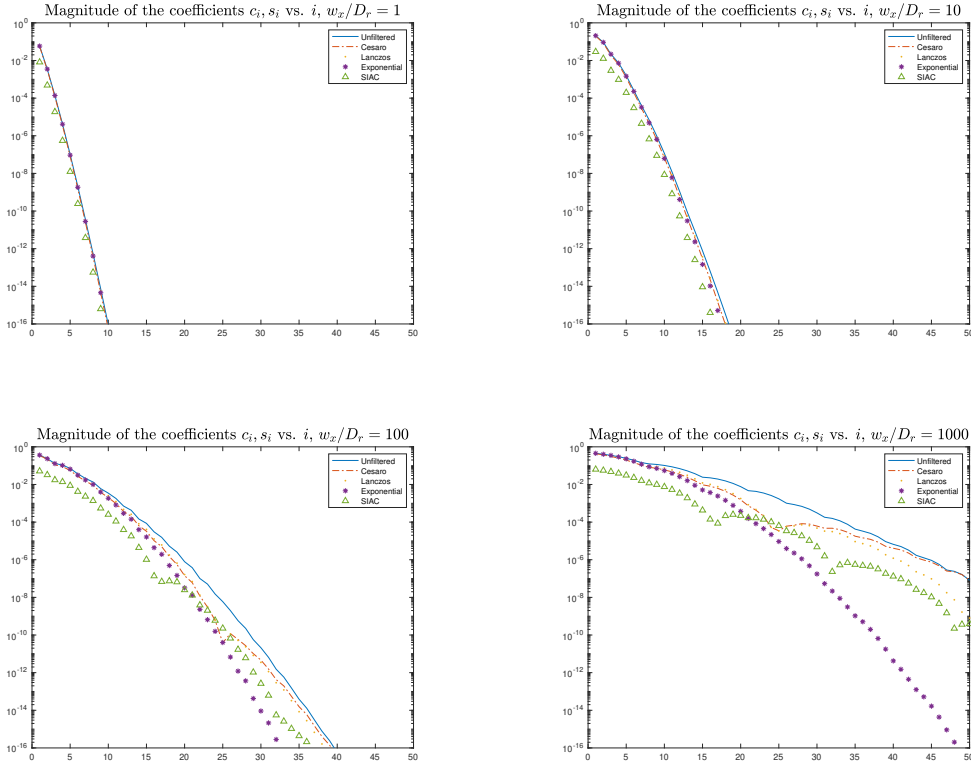


Figure 4.5.: Modulus of coefficients c_i, s_i versus i for the filtered and unfiltered spectral representations of f in the steady state approximation for shear flow with different values of $|w_x|/D_r$.

In Figure 4.5, we plot $\max\{|s_i|, |c_i|\}$ versus i for the filtered and unfiltered spectral representations of f in the steady state approximation for shear flow. For the exponential filter, we used $p = 2$, $\alpha = 5$ and $\eta_c = 0.01$. For the SIAC filter, we used $k = 50$. We consider different values of $|w_x/D_r|$. While the magnitude of the filtered and unfiltered coefficients for $w_x/D_r = 1$ and $w_x/D_r = 10$ decay at almost the same rate, the filtered coefficients for $w_x/D_r = 100$ and $w_x/D_r = 1000$ decay faster. The coefficients of the exponential filter decay the fastest.

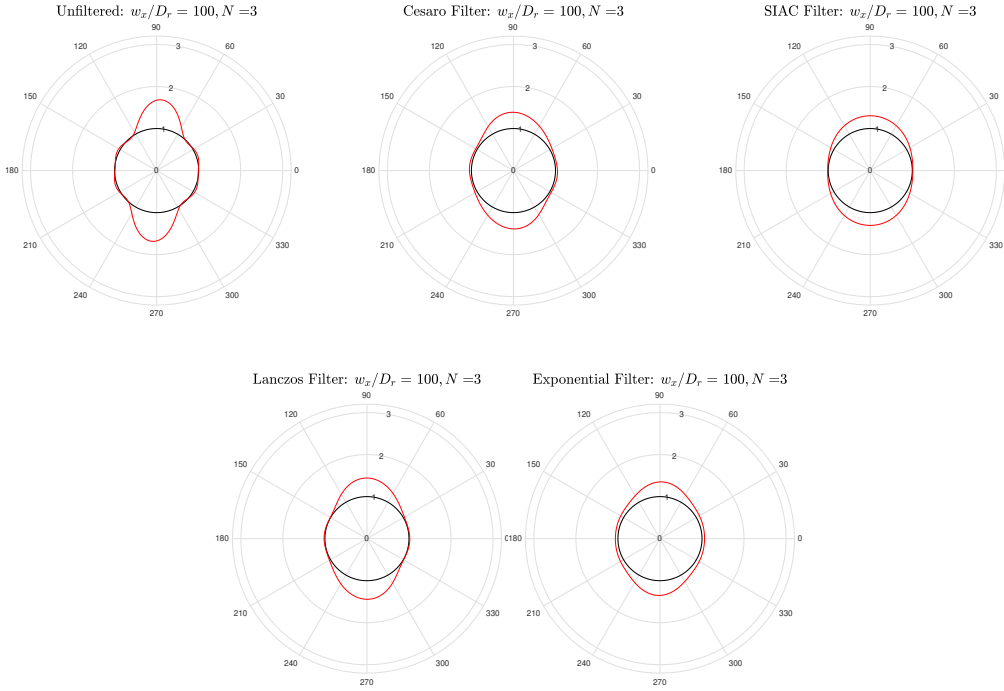


Figure 4.6.: Comparison of the approximations of the steady state solution of f for externally imposed shear flow with $w_x/D_r = 100$ and $N = 3$ using the filtered and unfiltered spectral methods.

In Figure 4.6, we compute the numerical approximation of the steady state of the exact solution of (4.1) for externally imposed shear flow and $w_x/D_r = 100$ with the unfiltered and filtered spectral methods using $N = 3$. We plot the solution over the unit sphere. As we have already seen in Figure 4.3, the approximation with the unfiltered spectral method using $N = 3$ leads to negative values of f which are unphysical. Using the same number of modes, the approximations of the filtered spectral methods preserve the positivity of the solution.

Next, we want to analyse whether the usage of the exponential filter also increases the accuracy of the method.

In Figure 4.7, the approximation of the steady state of the exact solution of (4.1) is computed

with the spectral method using the exponential filter and different values of N . The filtered approximation no longer leads to unphysical solutions, but the numerical solution is less accurate. While an unfiltered spectral method using $N = 8$ modes accurately approximates the reference solution in Figure 4.3, the spectral method using the exponential filter in Figure 4.7 needs $N = 20$ for a good approximation.

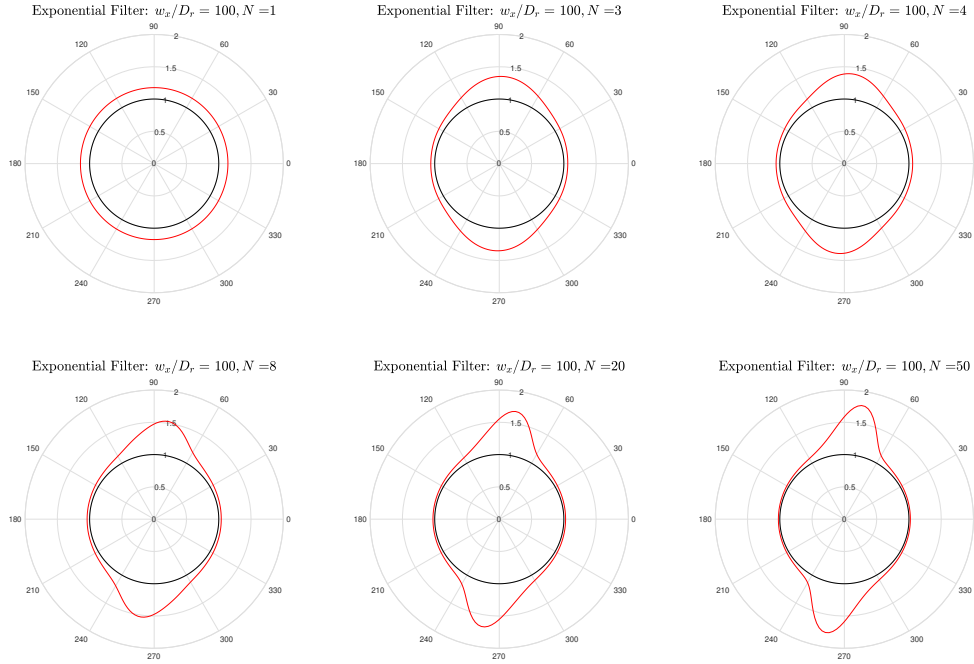


Figure 4.7.: Approximations of steady state solutions of f for externally imposed shear flow with $w_x/D_r = 100$ and different values of N using the exponential filter in the spectral method.

The application of filters to the approximation of the models for sedimentation in suspensions of rod-like particles might be studied in more detail in future research.

4.1.3 The One-Dimensional Transport Equation

For the approximation of the one-dimensional transport equation (4.2), the one-dimensional high-resolution Wave Propagation Algorithm by LeVeque, presented in subsection 2.2.3, can be used. Note that the one-dimensional transport equation needs to be solved for all $\theta \in [0, 2\pi)$.

Let $f_{i,k}^n$ approximate the cell average of f over a grid cell $[x_{i-1/2}, x_{i+1/2}] \times [\theta_{k-1/2}, \theta_{k+1/2}]$ of length $\Delta x := x_{i+1/2} - x_{i-1/2}$ and $\Delta\theta := \theta_{k+1/2} - \theta_{k-1/2}$ at time t^n . The grid for the numerical

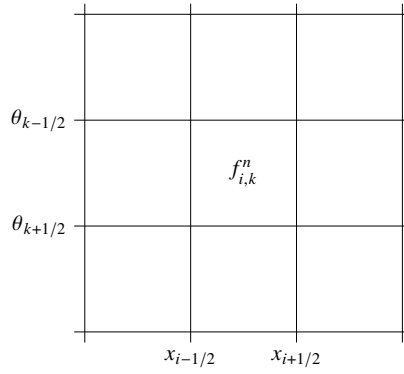


Figure 4.8.: Grid for the numerical approximation of the one-dimensional transport equation (4.2), where $f_{i,k}^n$ approximates the cell average at time t^n .

approximation of the one-dimensional transport equation is visualised in Figure 4.8. For each discretisation of θ , the cell average $f_{i,k}^n$ of the constant coefficient scalar advection equation (4.2) is updated using a method of the form

$$f_{i,k}^{n+1} = f_{i,k} - \frac{\Delta t}{\Delta x} (\mathcal{A}^+ \Delta Q_{i-1/2} + \mathcal{A}^- \Delta Q_{i+1/2}) - \frac{\Delta t}{\Delta x} (\tilde{F}_{i+1/2} - \tilde{F}_{i-1/2}), \quad \forall i.$$

4.2 A Detailed Numerical Method for General Two-Dimensional Flow

In this section, we describe a direct numerical method for the coupled model (3.2) for the two-dimensional flow problem.

For the coupled two-dimensional flow problem (3.2), the evolution of the incompressible velocity field is described with a two-dimensional Navier-Stokes equation, which can be computed during each time step with the projection method by Lee [52], presented in detail in section 2.5. Comparable to the approach in section 4.1, the three-dimensional evolution of f in model (3.2) can be split into two subproblems, which can be solved consecutively during each time step.

- (1) For each $x_i, i = 1, \dots, n, z_j, j = 1, \dots, n$, solve

$$\partial_t f + \partial_\theta \left(\left((w_z - u_x) \cos \theta \sin \theta - u_z \sin^2 \theta + w_x \cos^2 \theta \right) f \right) = D_r \partial_{\theta\theta} f \quad (4.6)$$

with the spectral method.

(2) For each $\theta_k \in [0, 2\pi]$, $k = 1, \dots, n$, solve

$$\partial_t + \partial_x ((u - \cos \theta \sin \theta) f) + \partial_z \left(\left(w - \left(1 + \sin^2 \theta \right) \right) f \right) = 0 \quad (4.7)$$

with the two-dimensional high-resolution Wave Propagation Algorithm.

4.2.1 Spectral Method for the Drift-Diffusion Equation

In this subsection, the drift-diffusion equation (4.6) of the two-dimensional flow problem is solved with spectral method using an ansatz of the form

$$f(\bar{x}, \bar{z}, t, \theta) = f_0(\bar{x}, \bar{z}, t) + \sum_{i=1}^N c_i(\bar{x}, \bar{z}, t) \cos(2i\theta) + s_i(\bar{x}, \bar{z}, t) \sin(2i\theta). \quad (4.8)$$

We assume that the components of the velocity gradient are constant and externally imposed at a given point (\bar{x}, \bar{z}) . We insert the ansatz (4.8) and the derivatives (4.4) in

$$\begin{aligned} \partial_t f(t, \theta) &= ((u_x - w_z) \cos 2\theta + (u_z + w_x) \sin 2\theta) f(t, \theta) \\ &+ \frac{1}{2} ((u_z - w_x) - (u_z + w_x) \cos 2\theta + (u_x - w_z) \sin 2\theta) \partial_\theta f \\ &+ D_r \partial_{\theta\theta} f, \end{aligned}$$

which is an equivalent representation of (4.6). Using Product-to-Sum Formulas results in

$$\begin{aligned} &f'_0(t) + \sum_{i=1}^N c'_i(t) \cos(2i\theta) + s'_i(t) \sin(2i\theta) \\ &= (u_x - w_z) \cos 2\theta f_0(t) + (u_z + w_x) \sin 2\theta f_0(t) \\ &+ \frac{1}{2} (u_x - w_z) \sum_{i=1}^N c_i(t) (\cos(2(i-1)\theta) + \cos(2(i+1)\theta)) \\ &+ \frac{1}{2} (u_x - w_z) \sum_{i=1}^N s_i(t) (\sin(2(i+1)\theta) + \sin(2(i-1)\theta)) \\ &+ \frac{1}{2} (u_z + w_x) \sum_{i=1}^N c_i(t) (\sin(2(i+1)\theta) - \sin(2(i-1)\theta)) \\ &+ \frac{1}{2} (u_z + w_x) \sum_{i=1}^N s_i(t) (\cos(2(i-1)\theta) - \cos(2(i+1)\theta)) \end{aligned}$$

$$\begin{aligned}
& + (u_z - w_x) \sum_{i=1}^N s_i(t) (-ic_i(t) \sin(2i\theta) + is_i(t) \cos(2i\theta)) \\
& + \frac{1}{2}(u_z + w_x) \sum_{i=1}^N ic_i(t) (\sin(2(i+1)\theta) + \sin(2(i-1)\theta)) \\
& - \frac{1}{2}(u_z + w_x) \sum_{i=1}^N is_i(t) (\cos(2(i-1)\theta) + \cos(2(i+1)\theta)) \\
& - \frac{1}{2}(u_x - w_z) \sum_{i=1}^N ic_i(t) (\cos(2(i-1)\theta) - \cos(2(i+1)\theta)) \\
& + \frac{1}{2}(u_x - w_z) \sum_{i=1}^N is_i(t) (\sin(2(i+1)\theta) + \sin(2(i-1)\theta)) \\
& - 4D_r \sum_{i=1}^N \left(i^2 c_i(t) \cos(2i\theta) + i^2 s_i(t) \sin(2i\theta) \right).
\end{aligned}$$

Matching terms of different order in $\cos(2i\theta)$ and $\sin(2i\theta)$ leads to

$$\begin{aligned}
1 & : f'_0(t) = 0 \\
\cos(2\theta) & : c'_1(t) = (u_x - w_z)f_0(t) + (u_z - w_x)s_1(t) - 4D_r c_1(t) \\
& \quad - \frac{1}{2}(u_x - w_z)c_2(t) - \frac{1}{2}(u_z + w_x)s_2(t), \\
\sin(2\theta) & : s'_1(t) = (u_z + w_x)f_0(t) - (u_z - w_x)c_1(t) - 4D_r s_1(t) \\
& \quad + \frac{1}{2}(u_z + w_x)c_2(t) - \frac{1}{2}(u_x - w_z)s_2(t), \\
\cos(2j\theta) & : c'_j(t) = \frac{j}{2}(u_x - w_z)(c_{j-1}(t) - c_{j+1}(t)) - 4D_r j^2 c_j(t) \\
& \quad - \frac{j}{2}(u_z + w_x)(s_{j-1}(t) + s_{j+1}(t)) + j(u_z - w_x)s_j(t), \quad j = 2, \dots, N, \\
\sin(2j\theta) & : s'_j(t) = \frac{j}{2}(u_z + w_x)(c_{j-1}(t) + c_{j+1}(t)) - j(u_z - w_x)c_j(t) \\
& \quad + \frac{j}{2}(u_x - w_z)(s_{j-1}(t) - s_{j+1}(t)) - 4D_r j^2 s_j(t), \quad j = 2, \dots, N.
\end{aligned} \tag{4.9}$$

As explained in subsection 4.1.1, we close the infinite system of ordinary differential equations by setting $c_{N+1} = s_{N+1} = 0$. Again, a matrix-vector formulation of the system of ordinary differential equations can be found in [33].

4.2.2 The Two-Dimensional Transport Equation

The two-dimensional transport equation (4.7) can be solved for each $\theta_k \in [0, 2\pi]$, $k = 1, \dots, n$, with the high-resolution Wave Propagation Algorithm of LeVeque, presented in subsection 2.3.3.

In two-dimensions, $f_{i,j,k}^n$ approximates the cell average of f over a grid cell $[x_{i-1/2}, x_{i+1/2}] \times [z_{j-1/2}, z_{j+1/2}] \times [\theta_{k-1/2}, \theta_{k+1/2}]$ in an equidistant grid with mesh width $\Delta x := x_{i+1/2} - x_{i-1/2}$, $\Delta z := z_{j+1/2} - z_{j-1/2}$ and $\Delta\theta := \theta_{k+1/2} - \theta_{k-1/2}$ at time t^n . For each $\theta_k \in [0, 2\pi]$, the cell average $f_{i,j,k}^n$ can be updated with the high-resolution Wave Propagation Algorithm

$$f_{i,j,k}^{n+1} = f_{i,j,k}^n - \frac{\Delta t}{\Delta x} (\mathcal{A}^+ \Delta Q_{i-1/2,j} + \mathcal{A}^- \Delta Q_{i+1/2,j}) - \frac{\Delta t}{\Delta x} (\mathcal{B}^+ \Delta Q_{i,j-1/2} + \mathcal{B}^- \Delta Q_{i,j+1/2}) - \frac{\Delta t}{\Delta x} (\tilde{F}_{i+1/2,j} - \tilde{F}_{i-1/2,j}) - \frac{\Delta t}{\Delta x} (\tilde{G}_{i,j+1/2} - \tilde{G}_{i,j-1/2}), \quad \forall i, j.$$

The fluctuations and waves are defined in a similar way as presented in Example 2.10. The fluxes $F_{i\pm 1/2,j}$, $G_{i,j\pm 1/2}$ depend on the spatially varying velocity field (u, v) (supposed to be constant in time during the substep) and on the discrete value of θ .

4.3 Transfer of Different Degrees of Freedom

For the computation of the evolution of f , the spectral method and the finite volume method need to be combined. As the two methods use different degrees of freedom, transformations between these degrees of freedom have to be defined. We explain the process for the two-dimensional flow problem. A similar approach can be applied for the shear flow problem.

Computation of cell average values

Applying the spectral method to (4.6) in each grid cell (i, j) of the two-dimensional spatial mesh results in a representation of $f(x_i, z_j, t, \theta)$ with coefficients f_0, c_i, s_i , $i = 1, \dots, N$ according to (4.8). From this representation of f , we want to compute cell average values $f_{i,j,k}$ on a three-dimensional grid in space and orientation with the finite volume method. Therefore, we use a projection of the form

$$f_{i,j,k}(t) = \frac{1}{\Delta\theta} \int_{\theta_{k-\frac{1}{2}}}^{\theta_{k+\frac{1}{2}}} f(x_i, z_j, t, \theta) d\theta$$

$$\approx f_0(x_i, z_j, t) + \frac{1}{\Delta\theta} \sum_{l=1}^N c_l(x_i, z_j, t) \frac{\sin(2l\theta)}{2l} - s_l(x_i, z_j, t) \frac{\cos(2l\theta)}{2l} \Bigg|_{\theta_{k-\frac{1}{2}}}^{\theta_{k+\frac{1}{2}}}.$$

Computation of mode coefficients

One step of the high-resolution Wave Propagation Algorithm applied to (4.7) results in cell average values $f_{i,j,k}^n$. We want to compute the coefficients of the spectral method in each grid cell of the two-dimensional spatial mesh. This can be done by a projection of the form

$$\begin{aligned} f_0(x_i, z_j, t) &= \frac{1}{2\pi} \int_0^{2\pi} f(x_i, z_j, t, \theta) d\theta \approx \frac{1}{2\pi} \Delta\theta \sum_k f_{i,j,k}, \\ c_l(x_i, z_j, t) &= \frac{1}{\pi} \int_0^{2\pi} \cos(2l\theta) f(x_i, z_j, t, \theta) d\theta \approx \frac{1}{\pi} \Delta\theta \sum_k \cos(2l\theta_k) f_{i,j,k}, \quad l = 1, \dots, N, \\ s_l(x_i, z_j, t) &= \frac{1}{\pi} \int_0^{2\pi} \sin(2l\theta) f(x_i, z_j, t, \theta) d\theta \approx \frac{1}{\pi} \Delta\theta \sum_k \sin(2l\theta_k) f_{i,j,k}, \quad l = 1, \dots, N. \end{aligned}$$

We apply the midpoint rule and sum over all grid cells used to discretise the interval $[0, 2\pi]$.

In the next chapter, a lower-dimensional model for sedimentation in suspension is introduced which allows us to formulate a method on the two-dimensional spatial grid only. The method does not require transformations between different degrees of freedom, which further simplifies the approach.

Hierarchy of Moment Equations

In the main part of this thesis, we derive a new macroscopic model based on a hierarchy of moment equations which describes the macroscopic flow in sedimentation in suspension of rod-like particles without resolving the microscopic structure. The hierarchy of moment equations replaces the distribution function in the kinetic model (3.1) and allows us to approximate the high dimensional scalar Smoluchowski equation with a lower dimensional system of partial differential equations. We have developed the method in [24, Sec. 4].

In section 5.1, the definition of the moments for the Smoluchowski equation and the moment closure strategy are introduced. In order to simplify the studies, we restrict our considerations to lower dimensional flow problems of two-dimensional flow and shear flow in the following sections. The derivation of a hierarchy of moment equations for a shear flow problem is explained in detail in section 5.2. Subsequently in section 5.3, we prove that the system of moment equations for the shear flow problem is hyperbolic for general N by using a similarity transformation. The derivation of the system of moment equations for the two-dimensional flow problem in section 5.4 is followed by the proof of hyperbolicity of the system in section 5.5.

5.1 Definition of Moments and Moment Closure

In this section, we present the definition of the moments used for the high-dimensional Smoluchowski equation and the moment closure strategy, which are both based on spherical harmonics. Note that the aim of this section is to give a basic understanding of the moment equations and to introduce the notation for the following sections. For a detailed review on spherical harmonics and the derivation of the moments, we refer to [35] and the references therein.

The moments for the Smoluchowski equation are defined as

$$\begin{aligned}
 \rho(\mathbf{x}, t) &:= \int_0^{2\pi} f(\mathbf{x}, t, \theta) d\theta, \\
 C_l(\mathbf{x}, t) &:= \frac{1}{2} \int_0^{2\pi} \cos(2l\theta) f(\mathbf{x}, t, \theta) d\theta, \quad l = 1, 2, \dots \\
 S_l(\mathbf{x}, t) &:= \frac{1}{2} \int_0^{2\pi} \sin(2l\theta) f(\mathbf{x}, t, \theta) d\theta, \quad l = 1, 2, \dots
 \end{aligned} \tag{5.1}$$

They are derived from the full model (3.1) and based on the eigenfunctions of the Laplace-Beltrami operator $\partial_{\theta\theta}$ on the circle S^1 , which are given as $1, \cos(n\theta), \sin(n\theta), n = 1, 2, 3, \dots$. Only the even eigenfunctions are used, as the rods are identical under reflection $\theta \rightarrow -\theta$. In contrast to the quasi-dynamic approximation presented in [35] and [34], which is only based on evolution equations for the density and second order moments, the approach presented in this chapter is based on a whole hierarchy of moment equations, which can adaptively adjust the level of detail used in the mathematical model and the numerical method.

The closure of the moment system is based on numerical results in [34]. Helzel and Tzavaras show that higher order moments decay faster than lower order moments because they correspond to a larger eigenvalue of the Laplace-Beltrami operator. Thus, a reasonable closure for the moment system is to neglect moments of order $N + 1$, i.e. to set $C_{N+1} = S_{N+1} = 0$. In [35], Helzel and Tzavaras use a generalisation of this moment closure for moment equations derived for the more general problem with f on S^2 and explain the closure with the geometric structure of harmonic polynomials.

5.2 Hierarchy of Moment Equations for Shear Flow

In this section, the derivation of a hierarchy of moment equations for the shear flow problem (3.3) is explained in detail.

For the evolution of a system of moment equations, we rewrite the time-dependent two-dimensional Smoluchowski equation in (3.3) as

$$\partial_t f(x, t, \theta) = - \underbrace{w_x \partial_\theta (\cos^2 \theta f(x, t, \theta))}_{(1)} + \underbrace{\frac{1}{2} \sin 2\theta \partial_x f(x, t, \theta)}_{(2)} + \underbrace{D_r \partial_{\theta\theta} f(x, t, \theta)}_{(3)}, \tag{5.2}$$

and consider the three different terms separately. The equation coloured in blue describes the spatial transport in x , the other two equations describe the transport in θ .

For the derivation of the evolution equation of the zero-th order moment ρ in (5.1), we insert equation (5.2) in $\partial_t \rho$ and integrate over S^1

$$\begin{aligned}\partial_t \rho(x, t) &= \int_0^{2\pi} \partial_t f(x, t, \theta) d\theta \\ &= \int_0^{2\pi} -\partial_\theta (w_x \cos^2 \theta f) + \partial_x (\sin \theta \cos \theta f) + D_r \partial_{\theta\theta} f d\theta \\ &= \int_0^{2\pi} \frac{1}{2} \sin(2\theta) \partial_x f d\theta \\ &= \partial_x S_1(x, t).\end{aligned}$$

Due to the periodicity of the solution, the first and third contribution in (5.2) vanish. We proceed similarly for the moments

$$\partial_t C_l(x, t) = \frac{1}{2} \int_0^{2\pi} \cos(2l\theta) \partial_t f(x, t, \theta) d\theta. \quad (5.3)$$

We insert (5.2) in (5.3) and consider the three different contributions of (5.2) separately.

Contribution of (1):

$$\begin{aligned}& -\frac{1}{2} \int_0^{2\pi} \cos(2l\theta) (w_x \cos^2 \theta f) d\theta \stackrel{\text{part. int.}}{=} -w_x l \int_0^{2\pi} \sin(2l\theta) \cos^2 \theta f d\theta \\ &= -w_x l \int_0^{2\pi} \sin(2l\theta) \frac{1}{2} (1 + \cos(2\theta)) f d\theta \\ &= -\frac{1}{2} w_x l \int_0^{2\pi} \sin(2l\theta) f d\theta - w_x \frac{l}{2} \int_0^{2\pi} \frac{1}{2} (\sin(2(l+1)\theta) + \sin(2(l-1)\theta)) f d\theta \\ &= -w_x l S_l - w_x \frac{l}{2} (S_{l+1} + S_{l-1})\end{aligned}$$

Contribution of (2):

$$\begin{aligned}& \frac{1}{4} \int_0^{2\pi} \cos(2l\theta) \sin(2\theta) \partial_x f d\theta = \frac{1}{4} \int_0^{2\pi} \frac{1}{2} (\sin(2(l+1)\theta) - \sin(2(l-1)\theta)) \partial_x f d\theta \\ &= \frac{1}{4} \partial_x (S_{l+1} - S_{l-1})\end{aligned}$$

Contribution of (3):

$$\frac{1}{2} D_r \int_0^{2\pi} \cos(2l\theta) \partial_{\theta\theta} f d\theta \stackrel{\text{part. int.}}{=} -\frac{1}{2} D_r \int_0^{2\pi} 4l^2 \cos(2l\theta) f d\theta = -4l^2 D_r C_l$$

All in all, the evolution equations for $C_l(x, t)$ are given as

$$\partial_t C_l(x, t) = \frac{1}{4} \partial_x (S_{l+1}(x, t) - S_{l-1}(x, t)) - \frac{l}{2} w_x (S_{l-1}(x, t) + 2S_l(x, t) + S_{l+1}(x, t)) - 4l^2 D_r C_l(x, t).$$

A similar procedure for the moments

$$\partial_t S_l(x, t) = \frac{1}{2} \int_0^{2\pi} \sin(2l\theta) \partial_t f(x, t, \theta) d\theta$$

leads to the following results.

Contribution of (1):

$$\begin{aligned} & -\frac{1}{2} \int_0^{2\pi} \sin(2l\theta) (w_x \cos^2 \theta f) d\theta \stackrel{\text{part. int.}}{=} w_x l \int_0^{2\pi} \cos(2l\theta) \cos^2 \theta f d\theta \\ &= w_x l \int_0^{2\pi} \cos(2l\theta) \frac{1}{2} (1 + \cos(2\theta)) f d\theta \\ &= \frac{1}{2} w_x l \int_0^{2\pi} \cos(2l\theta) f d\theta + w_x \frac{l}{2} \int_0^{2\pi} \frac{1}{2} (\cos(2(l+1)\theta) + \cos(2(l-1)\theta)) f d\theta \\ &= w_x l C_l + w_x \frac{l}{2} (C_{l+1} + C_{l-1}) \end{aligned}$$

Contribution of (2):

$$\begin{aligned} & \frac{1}{4} \int_0^{2\pi} \sin(2l\theta) \sin(2\theta) \partial_x f d\theta \\ &= \frac{1}{4} \int_0^{2\pi} \frac{1}{2} (\cos(2(l-1)\theta) - \cos(2(l+1)\theta)) \partial_x f d\theta \\ &= \frac{1}{4} \partial_x (C_{l-1} - C_{l+1}) \end{aligned}$$

Contribution of (3):

$$\frac{1}{2} D_r \int_0^{2\pi} \sin(2l\theta) \partial_{\theta\theta} f d\theta \stackrel{\text{part. int.}}{=} -\frac{1}{2} D_r \int_0^{2\pi} 4l^2 \sin(2l\theta) f d\theta = -4l^2 D_r S_l$$

In total, we obtain

$$\begin{aligned} \partial_t S_l(x, t) &= \frac{l}{2} w_x (C_{l-1}(x, t) + 2C_l(x, t) + C_{l+1}(x, t)) \\ &\quad - \frac{1}{4} \partial_x (C_{l+1}(x, t) - C_{l-1}(x, t)) - 4l^2 D_r S_l(x, t). \end{aligned}$$

We define

$$S_0(x, t) = \frac{1}{2} \int_0^{2\pi} \sin(\theta) f(x, t, \theta) d\theta = 0$$

and

$$C_0(x, t) = \frac{1}{2} \int_0^{2\pi} \cos(\theta) f(x, t, \theta) d\theta = \frac{1}{2} \rho(x, t),$$

in order to use the formulas for $l = 1$. Summarising all evolution equations, the complete infinite system of moment equations has the form

$$\begin{aligned} \partial_t \rho &= \partial_x S_1, \\ \partial_t C_l &= \frac{1}{4} \partial_x (S_{l+1} - S_{l-1}) - \frac{l}{2} w_x (S_{l-1} + 2S_l + S_{l+1}) - 4l^2 D_r C_l, \quad l = 1, 2, \dots \\ \partial_t S_l &= \frac{1}{4} \partial_x (C_{l+1} - C_{l-1}) + \frac{l}{2} w_x (C_{l-1} + 2C_l + C_{l+1}) - 4l^2 D_r S_l, \quad l = 1, 2, \dots \end{aligned}$$

In practical computations we need to consider a fixed number of moment equations. Hence, we use $l = 1, \dots, N$ in the last two equations. The equations C_N and S_N contain a term with C_{N+1} and S_{N+1} . As explained in section 5.1, we close the system by setting $C_{N+1} = S_{N+1} = 0$. The closed moment system is given as

$$\begin{aligned} \partial_t \rho &= \partial_x S_1, \\ \partial_t C_1 &= \frac{1}{4} \partial_x S_2 - \frac{1}{2} w_x (2S_1 + S_2) - 4D_r C_1, \\ \partial_t S_1 &= \frac{1}{8} \partial_x \rho - \frac{1}{4} \partial_x C_2 + \frac{1}{2} w_x \left(2C_1 + \frac{1}{2} \rho + C_2 \right) - 4D_r S_1, \\ \partial_t C_l &= \frac{1}{4} \partial_x (S_{l+1} - S_{l-1}) - \frac{l}{2} w_x (S_{l-1} + 2S_l + S_{l+1}) - 4l^2 D_r C_l, \quad l = 2, \dots, N-1, \\ \partial_t S_l &= \frac{1}{4} \partial_x (C_{l+1}(x, t) - C_{l-1}) + \frac{l}{2} w_x (C_{l-1} + 2C_l + C_{l+1}) - 4l^2 D_r S_l, \quad l = 2, \dots, N-1, \\ \partial_t C_N &= -\frac{1}{4} \partial_x S_{N-1} - \frac{N}{2} w_x (S_{N-1} + 2S_N) - 4N^2 D_r C_N, \\ \partial_t S_N &= \frac{1}{4} \partial_x C_{N-1} - \frac{N}{2} w_x (C_{N-1} + 2C_N) - 4N^2 D_r S_N, \end{aligned} \tag{5.4}$$

and is considered together with the flow equation

$$\text{Re } \partial_t w(x, t) = \partial_{xx} w(x, t) + \delta(\bar{\rho} - \rho(x, t)). \tag{5.5}$$

While the kinetic equation in (3.3) is a time-dependent partial differential equation in space and orientation, the system of moment equations (5.4) depends only on space and time. Consequently, the moment system allows us to approximate the time-dependent two-dimensional scalar Smoluchowski equation with a lower dimensional system of partial differential equations.

tions. In contrast to the detailed method from chapter 4, the scheme avoids transformations of different degrees of freedom. The relation between the detailed model (3.1) and the moment system will be analysed in more detail in section 6.3.

5.3 Hyperbolic Structure of the One-Dimensional System of Moment Equations for Shear Flow

In this section, we prove that the system of moment equations (5.4) is hyperbolic for general N . We rewrite (5.4) as a one-dimensional system of inhomogeneous conservation laws

$$\partial_t Q(x, t) + A \partial_x Q(x, t) = \varphi(Q(x, t)), \quad (5.6)$$

where $Q(x, t) = (\rho, C_1, S_1, \dots, C_N, S_N)^T$ represents the vector of moments. The coefficient matrix $A \in \mathbb{R}^{(2N+1) \times (2N+1)}$, coloured in blue, describes the approximation of the spatial transport in x and has the components

$$\begin{aligned} A_{1,3} &:= -1, \\ A_{3,1} &:= -\frac{1}{8}, \\ \begin{pmatrix} a_{2(N-j)-2, 2(N-j)-2} & \cdots & a_{2(N-j)-2, 2(N-j)+1} \\ \vdots & & \vdots \\ a_{2(N-j)+1, 2(N-j)-2} & \cdots & a_{2(N-j)+1, 2(N-j)+1} \end{pmatrix} &:= \begin{pmatrix} 0 & 0 & 0 & -\frac{1}{4} \\ 0 & 0 & \frac{1}{4} & 0 \\ 0 & \frac{1}{4} & 0 & 0 \\ -\frac{1}{4} & 0 & 0 & 0 \end{pmatrix}, \quad j = 0, \dots, N-2. \end{aligned} \quad (5.7)$$

All other entries are equal to zero. The matrix A can be expressed as the sum of a symmetric matrix and a rank two matrix.

5.1 Example. The system of moment equations for $N = 1$ is given as

$$\partial_t \begin{pmatrix} \rho \\ C_1 \\ S_1 \end{pmatrix} + \begin{pmatrix} 0 & 0 & -1 \\ 0 & 0 & 0 \\ -1/8 & 0 & 0 \end{pmatrix} \partial_x \begin{pmatrix} \rho \\ C_1 \\ S_1 \end{pmatrix} = \begin{pmatrix} 0 & 0 & 0 \\ 0 & -4D_r & -w_x \\ \frac{1}{4}w_x & w_x & -4D_r \end{pmatrix} \begin{pmatrix} \rho \\ C_1 \\ S_1 \end{pmatrix}.$$

5.2 Remark. The derivation of the moment system has shown that the homogeneous system results from subproblem (4.2) and the source term from subproblem (4.1).

In the remainder of the chapter, our goal is to prove that the system of moment equations (5.6) is hyperbolic for general N . According to Definition 2.1, we have to show that the matrix A has only real eigenvalues and a complete set of eigenvectors. In Example 2.5, we computed

the eigenvalues und eigenvectors for the system of moment equations for $N = 1$. For general N , the form of the eigenvalues of the matrix A is presented in the following remark.

5.3 Remark. We verified numerically that the eigenvalues of the coefficient matrix $A \in \mathbb{R}^{(2N+1) \times (2N+1)}$, defined in (5.7), have the form

$$\lambda_i = \sin(x_i) \cos(x_i) = \frac{1}{2} \sin(2x_i).$$

For N even, we have

$$x_i = \begin{cases} \frac{(2i-1) \cdot \pi}{4 + 8 \cdot \frac{N}{2}}, & i = 1, \dots, \frac{N}{2}, \\ \frac{-3\pi + 2(i - \frac{N}{2})\pi}{N+1}, & i = \frac{N}{2} + 1, \dots, \frac{3N}{2} + 1, \\ \frac{(2i - N - 1) \cdot \pi}{4 + 8 \cdot \frac{N}{2}}, & i = \frac{3N}{2} + 2, \dots, 2N + 1, \end{cases} \quad (5.8)$$

and for N odd, we have

$$x_i = \begin{cases} \frac{\pi i}{4 \cdot \lceil \frac{N}{2} \rceil}, & i = 1, \dots, \lceil \frac{N}{2} \rceil, \\ \frac{-3\pi + 4(i - \lfloor \frac{N}{2} \rfloor - 1)\pi}{8 \cdot \lceil \frac{N}{2} \rceil}, & i = \lceil \frac{N}{2} \rceil + 1, \dots, \lceil \frac{N}{2} \rceil + N + 1, \\ \frac{\pi \cdot (i - \lfloor \frac{N}{2} \rfloor - 1)}{4 \cdot \lceil \frac{N}{2} \rceil}, & i = \lceil \frac{N}{2} \rceil + N + 2, \dots, 2N + 1. \end{cases} \quad (5.9)$$

In contrast to the eigenvalues, there is no general structure recognisable for the eigenvectors of A for general N . But according to Example 2.5, there is a connection between the eigenvalues of the symmetric part of the $(4N + 3) \times (4N + 3)$ matrix and the eigenvalues of the original $(2N + 1) \times (2N + 1)$ matrix.

Thus, for proving the hyperbolicity of the coefficient matrix A for general N , we extend the approach based on similarity transformations, presented for $N = 1$ in Example 2.5, to general N . Therefore, we consider two auxiliary matrices $\bar{A}, \tilde{A} \in \mathbb{R}^{(4N+3) \times (4N+3)}$ with

$$\bar{A} = \left(\begin{array}{c|cc} 0 & & 0 \\ \hline 0 & A & 0 \\ \hline & 0 & A \end{array} \right), \quad \text{with } A \text{ as in (5.7),} \quad (5.10)$$

and

$$\tilde{A} = \begin{pmatrix} \tilde{a}_{2(2N-j)-2,2(2N-j)} & \cdots & \tilde{a}_{2(2N-j)-2,2(2N-j)+3} \\ \vdots & & \vdots \\ \tilde{a}_{2(2N-j)+3,2(2N-j)} & \cdots & \tilde{a}_{2(2N-j)+3,2(2N-j)+3} \end{pmatrix} = \begin{pmatrix} 0 & 0 & 0 & -\frac{1}{4} \\ 0 & 0 & \frac{1}{4} & 0 \\ 0 & \frac{1}{4} & 0 & 0 \\ -\frac{1}{4} & 0 & 0 & 0 \end{pmatrix}, \quad (5.11)$$

$$j = 0, \dots, N - 2,$$

all other components are equal to zero.

5.4 Remark. Note that the matrix \tilde{A} obtained for $N = k$ can be obtained from the matrix A for $N = 2k + 1$ by setting $a_{1,3} = a_{3,1} = 0$. We can of course ignore the first row and the first column of \bar{A} and \tilde{A} , but then this relation between A and \tilde{A} would be lost.

5.5 Lemma. Let $p_A(\lambda)$ be the characteristic polynomial of the coefficient matrix $A \in \mathbb{R}^{(2N+1) \times (2N+1)}$, defined in (5.7). Then the characteristic polynomial of $\bar{A} \in \mathbb{R}^{(4N+3) \times (4N+3)}$, defined in (5.10), has the form $p_{\bar{A}}(\lambda) = \lambda(p_A(\lambda))^2$.

Proof. Let I_k denote the $k \times k$ identity matrix. The characteristic polynomial of \bar{A} satisfies

$$p_{\bar{A}}(\lambda) = \det(\lambda I_{4N+3} - \bar{A}) = \lambda \det(\lambda I_{2N+1} - A) \det(\lambda I_{2N+1} - A) = \lambda(p_A(\lambda))^2.$$

□

5.6 Lemma. The matrices $\bar{A}, \tilde{A} \in \mathbb{R}^{(4N+3) \times (4N+3)}$, defined in (5.10) and (5.11), are similar.

Proof. For $N = 1$, the similarity of \bar{A} and \tilde{A} was shown in Example 2.5.

For $N > 1$, the structure of the similarity matrix and the matrix multiplications in Example 2.5 have to be generalised. We give a short sketch of the proof. We provide a nonsingular matrix $S \in \mathbb{R}^{(4N+3) \times (4N+3)}$ such that $\tilde{A} = S\bar{A}S^{-1}$. As the similarity matrix S has different structures for even and odd values of N , we consider these two cases separately. For odd N , the general form of the matrix S is analysed in detail. Also the procedure of multiplying the matrix S with the block diagonal matrix \bar{A} and the structure of the resulting product $Z = S\bar{A}$ is explained in full detail. Subsequently, we prove that multiplying Z with the inverse similarity transformation matrix S^{-1} results in the symmetric matrix \tilde{A} . For even N , similar considerations can be applied as for odd N so that we skip the details and only present the general structure of S , Z and S^{-1} .

We start with the case that $N > 1$ is odd.

The matrix S , which describes the similarity transformation between the matrix \bar{A} , defined in (5.10), and \tilde{A} , defined in (5.11), consists of eight different types of (4×4) -blocks. For

$j = 1, \dots, N - 1$, they are defined as

$$\begin{pmatrix} s_{2N-2j,2j+1} & \cdots & s_{2N-2j,2j+4} \\ \vdots & & \vdots \\ s_{2N-2j+3,2j+1} & \cdots & s_{2N-2j+3,2j+4} \end{pmatrix} = \begin{cases} \begin{pmatrix} 0 & 0 & 1 & -1 \\ 0 & 0 & 0 & 0 \\ 0 & 0 & 0 & 0 \\ -1 & -1 & 0 & 0 \end{pmatrix}, & \text{if } j \text{ is even,} \\ \begin{pmatrix} 0 & 0 & 0 & 0 \\ 0 & 0 & -1 & -1 \\ 1 & -1 & 0 & 0 \\ 0 & 0 & 0 & 0 \end{pmatrix}, & \text{if } j \text{ is odd,} \end{cases}$$

$$\begin{pmatrix} s_{2N+2j+2,2j+1} & \cdots & s_{2N+2j+2,2j+4} \\ \vdots & & \vdots \\ s_{2N+2j+5,2j+1} & \cdots & s_{2N+2j+5,2j+4} \end{pmatrix} = \begin{cases} \begin{pmatrix} 0 & 0 & 0 & 0 \\ -1 & 1 & 0 & 0 \\ 0 & 0 & 1 & 1 \\ 0 & 0 & 0 & 0 \end{pmatrix}, & \text{if } j \text{ is even,} \\ \begin{pmatrix} 1 & 1 & 0 & 0 \\ 0 & 0 & 0 & 0 \\ 0 & 0 & 0 & 0 \\ 0 & 0 & -1 & 1 \end{pmatrix}, & \text{if } j \text{ is odd,} \end{cases}$$

$$\begin{pmatrix} s_{2N-2j,2j+2j+2} & \cdots & s_{2N-2j,2N+2j+5} \\ \vdots & & \vdots \\ s_{2N-2j+3,2N+2j+2} & \cdots & s_{2N-2j+3,2N+2j+5} \end{pmatrix} = \begin{cases} \begin{pmatrix} 0 & 0 & 0 & 0 \\ 0 & 0 & 1 & -1 \\ 1 & 1 & 0 & 0 \\ 0 & 0 & 0 & 0 \end{pmatrix}, & \text{if } j \text{ is even,} \\ \begin{pmatrix} 0 & 0 & 1 & 1 \\ 0 & 0 & 0 & 0 \\ 0 & 0 & 0 & 0 \\ 1 & -1 & 0 & 0 \end{pmatrix}, & \text{if } j \text{ is odd,} \end{cases}$$

N . Obviously, the first line and the first column of Z contain only zeros. Column two and $(2N + 3)$ of S contain only one nonzero element with value $-\frac{1}{2}$ and $\frac{1}{2}$, respectively. These entries are the only nonzero elements in rows $2N + 2$ and $2N + 3$ of S . When we build the matrix product $S\bar{A}$, those entries of S are multiplied with the -1 entries of \bar{A} and lead to

$$z_{2N+2,2N+5} = -\frac{1}{2}, \quad z_{2N+3,4} = \frac{1}{2}.$$

All other rows and columns of S contain two nonzero elements with values -1 or 1 . In rows with two nonzero elements, the nonzero elements arise next to each other. Therefore, each nonzero element of \bar{A} , except the above discussed entries with value -1, contributes to two nonzero entries in the product $S\bar{A}$. In particular, the two matrix elements of \bar{A} with value $-\frac{1}{8}$ lead to the four nonzero matrix elements

$$z_{2N,2} = \frac{1}{8}, \quad z_{2N+1,2N+1} = \frac{1}{8}, \quad z_{2N+4,2} = -\frac{1}{8}, \quad z_{2N+5,2N+1} = -\frac{1}{8}.$$

The remaining nonzero elements of \bar{A} result from 4×4 blocks of the anti-diagonal matrix described in the last equation of (5.10). Each of these 4×4 blocks of the matrix A arises twice in the matrix \bar{A} and contributes to 16 nonzero elements in $S\bar{A}$. We use eight different 4×4 blocks to describe the remaining non-zero entries of $S\bar{A}$. For $j = 0, \dots, \lfloor \frac{N}{2} \rfloor$, we have

$$\begin{aligned} \begin{pmatrix} z_{4j+2,2N-4j-1} & \cdots & z_{4j+2,2N-4j+2} \\ \vdots & & \vdots \\ z_{4j+5,2N-4j-1} & \cdots & z_{4j+5,2N-4j+2} \end{pmatrix} &= \begin{pmatrix} \frac{1}{4} & \frac{1}{4} & 0 & 0 \\ 0 & 0 & 0 & 0 \\ 0 & 0 & 0 & 0 \\ 0 & 0 & -\frac{1}{4} & \frac{1}{4} \end{pmatrix}, \\ \begin{pmatrix} z_{4j+2,4N-4j} & \cdots & z_{4j+2,4N-4j+3} \\ \vdots & & \vdots \\ z_{4j+5,2N-4j} & \cdots & z_{4j+5,2N-4j+3} \end{pmatrix} &= \begin{pmatrix} 0 & 0 & 0 & 0 \\ \frac{1}{4} & \frac{1}{4} & 0 & 0 \\ 0 & 0 & \frac{1}{4} & -\frac{1}{4} \\ 0 & 0 & 1 & 1 \end{pmatrix}, \\ \begin{pmatrix} z_{4j+4,2N-4j-3} & \cdots & z_{4j+4,2N-4j} \\ \vdots & & \vdots \\ z_{4j+7,2N-4j-3} & \cdots & z_{4j+7,2N-4j} \end{pmatrix} &= \begin{pmatrix} 0 & 0 & 0 & 0 \\ \frac{1}{4} & -\frac{1}{4} & 0 & 0 \\ 0 & 0 & -\frac{1}{4} & -\frac{1}{4} \\ 0 & 0 & 0 & 0 \end{pmatrix}, \\ \begin{pmatrix} z_{4j+4,2N-4j-2} & \cdots & z_{4j+4,2N-4j+1} \\ \vdots & & \vdots \\ z_{4j+7,2N-4j-1} & \cdots & z_{4j+7,2N-4j+1} \end{pmatrix} &= \begin{pmatrix} -\frac{1}{4} & \frac{1}{4} & 0 & 0 \\ 0 & 0 & 0 & 0 \\ 0 & 0 & 0 & 0 \\ 0 & 0 & -\frac{1}{4} & -\frac{1}{4} \end{pmatrix}, \end{aligned}$$

5.3. Hyperbolic Structure of the One-Dimensional System of Moment Equations for Shear Flow

$$\begin{pmatrix} z_{4N-4j-2,2N-4j-3} & \cdots & z_{4N-4j-2,2N-4j} \\ \vdots & & \vdots \\ z_{4N-4j+1,2N-4j-3} & \cdots & z_{4N-4j+1,2N-4j} \end{pmatrix} = \begin{pmatrix} 0 & 0 & \frac{1}{4} & -\frac{1}{4} \\ 0 & 0 & 0 & 0 \\ 0 & 0 & 0 & 0 \\ -\frac{1}{4} & -\frac{1}{4} & 0 & 0 \end{pmatrix},$$

$$\begin{pmatrix} z_{4N-4j-2,2N-4j-2} & \cdots & z_{4N-4j-2,4N-4j+1} \\ \vdots & & \vdots \\ z_{4N-4j+1,2N-4j-2} & \cdots & z_{4N-4j+1,2N-4j+1} \end{pmatrix} = \begin{pmatrix} 0 & 0 & 0 & 0 \\ 0 & 0 & \frac{1}{4} & -\frac{1}{4} \\ \frac{1}{4} & \frac{1}{4} & 0 & 0 \\ 0 & 0 & 0 & 0 \end{pmatrix},$$

$$\begin{pmatrix} z_{4N-4j,2N-4j-1} & \cdots & z_{4N-4j-2,2N-4j+2} \\ \vdots & & \vdots \\ z_{4N-4j+3,2N-4j-1} & \cdots & z_{4N-4j+3,2N-4j+2} \end{pmatrix} = \begin{pmatrix} 0 & 0 & 0 & 0 \\ 0 & 0 & \frac{1}{4} & \frac{1}{4} \\ -\frac{1}{4} & \frac{1}{4} & 0 & 0 \\ 0 & 0 & 0 & 0 \end{pmatrix},$$

$$\begin{pmatrix} z_{4N-4j,4N-4j} & \cdots & z_{4N-4j,4N-4j+3} \\ \vdots & & \vdots \\ z_{4N-4j+3,2N-4j} & \cdots & z_{4N-4j+3,4N-4j+3} \end{pmatrix} = \begin{pmatrix} 0 & 0 & -\frac{1}{4} & -\frac{1}{4} \\ 0 & 0 & 0 & 0 \\ 0 & 0 & 0 & 0 \\ -\frac{1}{4} & \frac{1}{4} & 0 & 0 \end{pmatrix}.$$

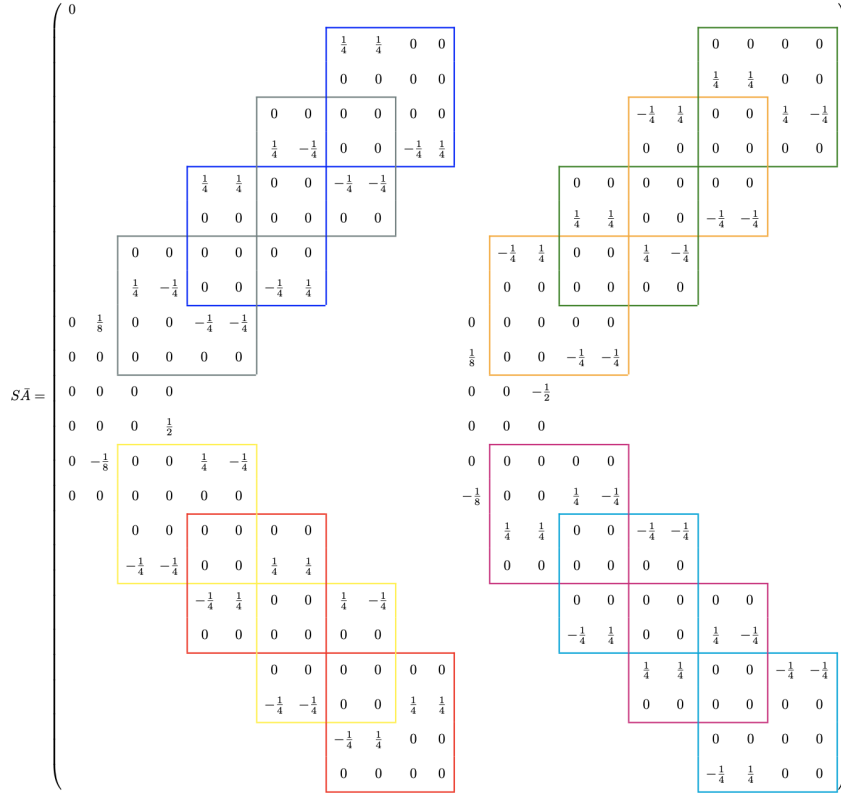


Figure 5.2.: Structure of the matrix $Z = S\bar{A}$ for $N = 5$.

The structure of the matrix $Z = S\bar{A}$ for $N = 5$ is shown in Figure 5.2. Finally, we multiply the matrix Z with S^{-1} . The structure of the matrix S^{-1} can easily be derived from S . Again, S^{-1} is composed of eight different types of blocks. In the following, we use the notation $s_{i,j}^{-1}$ to denote the (i, j) component of the matrix S^{-1} . For $j = 1, \dots, N - 1$, we have

$$\begin{aligned}
 \begin{pmatrix} s_{2j+1,2N-2j+2}^{-1} & \cdots & s_{2j+1,2N-2j+5}^{-1} \\ \vdots & & \vdots \\ s_{2j+4,2N-2j+2}^{-1} & \cdots & s_{2j+4,2N-2j+5}^{-1} \end{pmatrix} &= \begin{cases} \begin{pmatrix} 0 & 0 & \frac{1}{2} & 0 \\ 0 & 0 & -\frac{1}{2} & 0 \\ 0 & -\frac{1}{2} & 0 & 0 \\ 0 & -\frac{1}{2} & 0 & 0 \end{pmatrix}, & \text{if } j \text{ is odd,} \\ \begin{pmatrix} 0 & 0 & 0 & -\frac{1}{2} \\ 0 & 0 & 0 & -\frac{1}{2} \\ \frac{1}{2} & 0 & 0 & 0 \\ -\frac{1}{2} & 0 & 0 & 0 \end{pmatrix}, & \text{if } j \text{ is even,} \end{cases} \\
 \\
 \begin{pmatrix} s_{2j+1,2N+2j+2}^{-1} & \cdots & s_{2j+1,2N+2j+5}^{-1} \\ \vdots & & \vdots \\ s_{2j+4,2N+2j+2}^{-1} & \cdots & s_{2j+4,2N+2j+5}^{-1} \end{pmatrix} &= \begin{cases} \begin{pmatrix} 0 & -\frac{1}{2} & 0 & 0 \\ 0 & \frac{1}{2} & 0 & 0 \\ 0 & 0 & \frac{1}{2} & 0 \\ 0 & 0 & \frac{1}{2} & 0 \end{pmatrix}, & \text{if } j \text{ is even,} \\ \begin{pmatrix} \frac{1}{2} & 0 & 0 & 0 \\ \frac{1}{2} & 0 & 0 & 0 \\ 0 & 0 & 0 & -\frac{1}{2} \\ 0 & 0 & 0 & \frac{1}{2} \end{pmatrix}, & \text{if } j \text{ is odd,} \end{cases} \\
 \\
 \begin{pmatrix} s_{2N+2j+2,2N-2j}^{-1} & \cdots & s_{2N+2j+2,2N-2j+3}^{-1} \\ \vdots & & \vdots \\ s_{2N+2j+5,2N-2j}^{-1} & \cdots & s_{2N+2j+5,2N-2j+3}^{-1} \end{pmatrix} &= \begin{cases} \begin{pmatrix} 0 & 0 & \frac{1}{2} & 0 \\ 0 & 0 & \frac{1}{2} & 0 \\ 0 & \frac{1}{2} & 0 & 0 \\ 0 & -\frac{1}{2} & 0 & 0 \end{pmatrix}, & \text{if } j \text{ is even,} \\ \begin{pmatrix} 0 & 0 & 0 & \frac{1}{2} \\ 0 & 0 & 0 & -\frac{1}{2} \\ \frac{1}{2} & 0 & 0 & 0 \\ \frac{1}{2} & 0 & 0 & 0 \end{pmatrix}, & \text{if } j \text{ is odd,} \end{cases}
 \end{aligned}$$

$$\begin{pmatrix} s_{2N+2j+2,2N+2j+2}^{-1} & \cdots & s_{2N+2j+2,2N+2j+5}^{-1} \\ \vdots & & \vdots \\ s_{2N+2j+5,2N+2j+2}^{-1} & \cdots & s_{2N+2j+5,2N+2j+5}^{-1} \end{pmatrix} = \begin{cases} \begin{pmatrix} \frac{1}{2} & 0 & 0 & 0 \\ -\frac{1}{2} & 0 & 0 & 0 \\ 0 & 0 & 0 & \frac{1}{2} \\ 0 & 0 & 0 & \frac{1}{2} \end{pmatrix}, & \text{if } j \text{ is even,} \\ \begin{pmatrix} 0 & \frac{1}{2} & 0 & 0 \\ 0 & \frac{1}{2} & 0 & 0 \\ 0 & 0 & \frac{1}{2} & 0 \\ 0 & 0 & -\frac{1}{2} & 0 \end{pmatrix}, & \text{if } j \text{ is odd.} \end{cases}$$

Furthermore, we have

$$s_{1,1}^{-1} = 1, \quad s_{2,2N+3}^{-1} = -2, \quad s_{2N+3,2N+2}^{-1} = 2.$$

All other entries are equal to zero. Each block is repeated $\lfloor \frac{N}{2} \rfloor$ times. For $N = 5$, the structure of the matrix S^{-1} is illustrated in Figure 5.3.

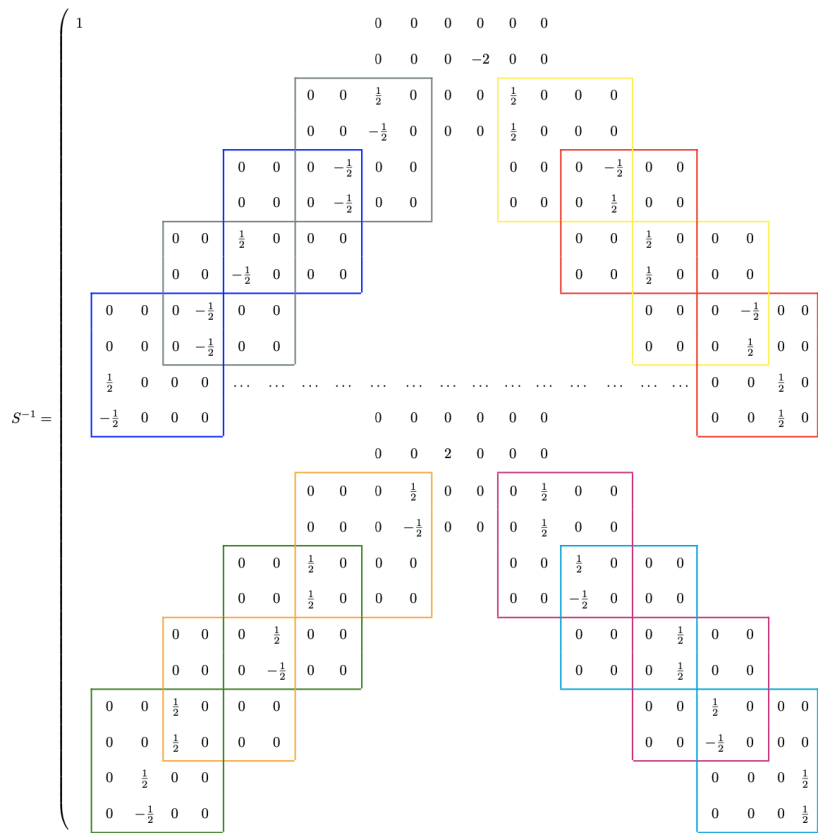


Figure 5.3.: Structure of the matrix S^{-1} for $N = 5$.

Finally, we want to show that the matrix-matrix product ZS^{-1} is equal to the symmetric matrix \tilde{A} , described in (5.11). The matrix $Z = S\tilde{A}$ is mainly characterised by pairs of $\pm\frac{1}{4}$ which arise next to each other and the structure of S^{-1} is mainly characterised by pairs of $\pm\frac{1}{2}$ appearing below each other. This results in values $\pm\frac{1}{4}$ or 0 when we multiply a single row of Z with a single column of S^{-1} . The four special entries of Z with values $\pm\frac{1}{8}$ only lead to a nonzero contribution in the product ZS^{-1} when they are multiplied with the columns $2N+2$ and $2N+3$ of S^{-1} , which contain the special nonzero entries ± 2 . Again, we obtain values $\pm\frac{1}{4}$. Thus, the only nonzero entries of ZS^{-1} have values $\pm\frac{1}{4}$.

Let us now consider the product of Z with the last four columns of S^{-1} .

Contribution from column $4N+3$: We only need to consider the product with rows 4 and $4N$ of Z and obtain

$$(ZS^{-1})_{4,4N+3} = \frac{1}{4}\frac{1}{2} - \frac{1}{4}\frac{1}{2} = 0$$

$$(ZS^{-1})_{4N,4N+3} = -\frac{1}{4}\frac{1}{2} - \frac{1}{4}\frac{1}{2} = -\frac{1}{4}$$

Contribution from column $4N+2$: Now, we only need to consider the product with rows 5 and $4N+1$ of Z and obtain

$$(ZS^{-1})_{5,4N+2} = -\frac{1}{4}\frac{1}{2} + \frac{1}{4}\frac{1}{2} = 0,$$

$$(ZS^{-1})_{4N+1,4N+2} = \frac{1}{4}\frac{1}{2} + \frac{1}{4}\frac{1}{2} = \frac{1}{4}.$$

Contribution from column $4N+1$: Now, we consider the product with rows 2, 6 and $4N+2, 4N-2$ of Z and obtain

$$(ZS^{-1})_{2,4N+1} = \frac{1}{4}\left(-\frac{1}{2}\right) + \frac{1}{4}\frac{1}{2} = 0,$$

$$(ZS^{-1})_{6,4N+1} = -\frac{1}{4}\left(-\frac{1}{2}\right) - \frac{1}{4}\frac{1}{2} = 0,$$

$$(ZS^{-1})_{4N-2,4N+1} = \frac{1}{4}\left(-\frac{1}{2}\right) - \frac{1}{4}\frac{1}{2} = -\frac{1}{4},$$

$$(ZS^{-1})_{4N+2,4N+1} = -\frac{1}{4}\left(-\frac{1}{2}\right) + \frac{1}{4}\frac{1}{2} = \frac{1}{4}.$$

Contribution from column $4N$: We consider the product with rows 3, 7 and $4N-1, 4N+3$ of Z and obtain

$$(ZS^{-1})_{3,4N} = \frac{1}{4}\frac{1}{2} + \frac{1}{4}\left(-\frac{1}{2}\right) = 0,$$

$$(ZS^{-1})_{7,4N} = -\frac{1}{4}\frac{1}{2} - \frac{1}{4}\left(-\frac{1}{2}\right) = 0,$$

$$(ZS^{-1})_{4N-1,4N} = \frac{1}{4}\frac{1}{2} - \frac{1}{4}\left(-\frac{1}{2}\right) = \frac{1}{4},$$

$$(ZS^{-1})_{4N+3,4N} = -\frac{1}{4}\frac{1}{2} + \frac{1}{4}\left(-\frac{1}{2}\right) = -\frac{1}{4}.$$

Thus, the multiplication of Z with the last four columns of S^{-1} produces the symmetric 4×4 block

$$\begin{array}{c} 4N \quad 4N+1 \quad 4N+2 \quad 4N+3 \\ \begin{array}{c} 4N \\ 4N+1 \\ 4N+2 \\ 4N+3 \end{array} \begin{pmatrix} 0 & 0 & 0 & -\frac{1}{4} \\ 0 & 0 & \frac{1}{4} & 0 \\ 0 & \frac{1}{4} & 0 & 0 \\ -\frac{1}{4} & 0 & 0 & 0 \end{pmatrix} \end{array}$$

of $S\bar{A}S^{-1}$ and contributes two nonzero entries to the 4×4 block

$$\begin{array}{c} 4N-2 \quad 4N-1 \quad 4N \quad 4N+1 \\ \begin{array}{c} 4N-2 \\ 4N-1 \\ 4N \\ 4N+1 \end{array} \begin{pmatrix} 0 & 0 & 0 & -\frac{1}{4} \\ 0 & 0 & \frac{1}{4} & 0 \\ 0 & 0 & 0 & 0 \\ 0 & 0 & 0 & 0 \end{pmatrix}. \end{array}$$

This pattern continues, i.e. the next two columns will contribute the missing two nonzero entries at the positions $(4N, 4N-1)$ and $(4N+1, 4N-2)$ and two entries to the next 4×4 block. Finally, the first two columns will contribute the last two missing nonzero entries. This completes the proof for odd values of $N > 1$.

Next, we consider the case $N > 1$ is even.

In this case, we only provide the general form of the matrices S , $Z = S\bar{A}$ and S^{-1} and skip the details of the multiplication process.

For $j = 1, \dots, N-1$, the blocks of S are given as

$$\begin{pmatrix} s_{2N-2j,2j+1} & \cdots & s_{2N-2j,2j+4} \\ \vdots & & \vdots \\ s_{2N-2j+3,2j+1} & & s_{2N-2j+3,2j+4} \end{pmatrix} = \begin{cases} \begin{pmatrix} 0 & 0 & 0 & 0 \\ 0 & 0 & -1 & -1 \\ 1 & -1 & 0 & 0 \\ 0 & 0 & 0 & 0 \end{pmatrix}, & \text{if } j \text{ is even,} \\ \begin{pmatrix} 0 & 0 & 1 & -1 \\ 0 & 0 & 0 & 0 \\ 0 & 0 & 0 & 0 \\ -1 & -1 & 0 & 0 \end{pmatrix}, & \text{if } j \text{ is odd,} \end{cases}$$

$$\begin{aligned}
 \begin{pmatrix} s_{2N+2j+2,2j+1} & \cdots & s_{2N+2j+2,2j+4} \\ \vdots & & \vdots \\ s_{2N+2j+5,2j+1} & & s_{2N+2j+5,2j+4} \end{pmatrix} &= \begin{cases} \begin{pmatrix} 1 & 1 & 0 & 0 \\ 0 & 0 & 0 & 0 \\ 0 & 0 & 0 & 0 \\ 0 & 0 & -1 & 1 \end{pmatrix}, & \text{if } j \text{ is even,} \\ \begin{pmatrix} 0 & 0 & 0 & 0 \\ -1 & 1 & 0 & 0 \\ 0 & 0 & 1 & 1 \\ 0 & 0 & 0 & 0 \end{pmatrix}, & \text{if } j \text{ is odd,} \end{cases} \\
 \begin{pmatrix} s_{2N-2j,2N+2j+2} & \cdots & s_{2N-2j,2N+2j+5} \\ \vdots & & \vdots \\ s_{2N-2j+3,2N+2j+2} & & s_{2N-2j+3,2N+2j+5} \end{pmatrix} &= \begin{cases} \begin{pmatrix} 0 & 0 & 1 & 1 \\ 0 & 0 & 0 & 0 \\ 0 & 0 & 0 & 0 \\ 1 & -1 & 0 & 0 \end{pmatrix}, & \text{if } j \text{ is even,} \\ \begin{pmatrix} 0 & 0 & 0 & 0 \\ 0 & 0 & 1 & -1 \\ 1 & 1 & 0 & 0 \\ 0 & 0 & 0 & 0 \end{pmatrix}, & \text{if } j \text{ is odd,} \end{cases} \\
 \begin{pmatrix} s_{2N+2j+2,2N+2j+2} & \cdots & s_{2N+2j+2,2N+2j+5} \\ \vdots & & \vdots \\ s_{2N+2j+5,2N+2j+2} & & s_{2N+2j+5,2N+2j+5} \end{pmatrix} &= \begin{cases} \begin{pmatrix} 0 & 0 & 0 & 0 \\ 1 & 1 & 0 & 0 \\ 0 & 0 & 1 & -1 \\ 0 & 0 & 0 & 0 \end{pmatrix}, & \text{if } j \text{ is even,} \\ \begin{pmatrix} 1 & -1 & 0 & 0 \\ 0 & 0 & 0 & 0 \\ 0 & 0 & 0 & 0 \\ 0 & 0 & 1 & 1 \end{pmatrix}, & \text{if } j \text{ is odd.} \end{cases}
 \end{aligned}$$

In addition, we have

$$s_{1,1} = 1, \quad s_{2N+2,2} = \frac{1}{2}, \quad s_{2N+3,2N+3} = \frac{1}{2}.$$

All other components of S are equal to zero. Figure 5.4 shows the structure of S for $N = 4$.

$$\begin{aligned}
 \begin{pmatrix} z_{4N-4j-2,2N-4j-3} & \cdots & z_{4N-4j-2,2N-4j} \\ \vdots & & \vdots \\ z_{4N-4j+1,2N-4j-3} & \cdots & z_{4N-4j+1,2N-4j} \end{pmatrix} &= \begin{pmatrix} 0 & 0 & \frac{1}{4} & -\frac{1}{4} \\ 0 & 0 & 0 & 0 \\ 0 & 0 & 0 & 0 \\ -\frac{1}{4} & -\frac{1}{4} & 0 & 0 \end{pmatrix} \quad j = 0, \dots, \frac{N}{2} - 2, \\
 \begin{pmatrix} z_{4N-4j-2,4N-4j-2} & \cdots & z_{4N-4j-2,4N-4j+1} \\ \vdots & & \vdots \\ z_{4N-4j+1,4N-4j-2} & \cdots & z_{4N-4j+1,4N-4j+1} \end{pmatrix} &= \begin{pmatrix} 0 & 0 & 0 & 0 \\ 0 & 0 & \frac{1}{4} & -\frac{1}{4} \\ \frac{1}{4} & \frac{1}{4} & 0 & 0 \\ 0 & 0 & 0 & 0 \end{pmatrix} \quad j = 0, \dots, \frac{N}{2} - 2, \\
 \begin{pmatrix} z_{4N-4j,2N-4j-1} & \cdots & z_{4N-4j,2N-4j+2} \\ \vdots & & \vdots \\ z_{4N-4j+3,2N-4j-1} & \cdots & z_{4N-4j+3,2N-4j+2} \end{pmatrix} &= \begin{pmatrix} 0 & 0 & 0 & 0 \\ 0 & 0 & \frac{1}{4} & \frac{1}{4} \\ -\frac{1}{4} & \frac{1}{4} & 0 & 0 \\ 0 & 0 & 0 & 0 \end{pmatrix} \quad j = 0, \dots, \frac{N}{2} - 1, \\
 \begin{pmatrix} z_{4N-4j,4N-4j} & \cdots & z_{4N-4j,4N-4j+3} \\ \vdots & & \vdots \\ z_{4N-4j+3,4N-4j} & \cdots & z_{4N-4j+3,4N-4j+3} \end{pmatrix} &= \begin{pmatrix} 0 & 0 & -\frac{1}{4} & -\frac{1}{4} \\ 0 & 0 & 0 & 0 \\ 0 & 0 & 0 & 0 \\ -\frac{1}{4} & \frac{1}{4} & 0 & 0 \end{pmatrix} \quad j = 0, \dots, \frac{N}{2} - 1.
 \end{aligned}$$

In addition, we have

$$\begin{aligned}
 z_{2N,2N+3} &= -\frac{1}{8}, & z_{2N+1,2} &= \frac{1}{8}, & z_{2N+2,4} &= -\frac{1}{2}, \\
 z_{2N+3,2N+3} &= -\frac{1}{2}, & z_{2N+4,2} &= \frac{1}{8}, & z_{2N+5,2} &= -\frac{1}{8}.
 \end{aligned}$$

The structure of $Z := S\bar{A}$ is illustrated in Figure 5.6.

$$\begin{aligned}
 \begin{pmatrix} s_{2j+1,2N+2j+2}^{-1} & \cdots & s_{2j+1,2N+2j+5}^{-1} \\ \vdots & & \vdots \\ s_{2j+4,2N+2j+2}^{-1} & \cdots & s_{2j+4,2N+2j+5}^{-1} \end{pmatrix} &= \begin{cases} \begin{pmatrix} \frac{1}{2} & 0 & 0 & 0 \\ \frac{1}{2} & 0 & 0 & 0 \\ 0 & 0 & 0 & -\frac{1}{2} \\ 0 & 0 & 0 & \frac{1}{2} \end{pmatrix}, & \text{if } j \text{ is even,} \\ \begin{pmatrix} 0 & -\frac{1}{2} & 0 & 0 \\ 0 & \frac{1}{2} & 0 & 0 \\ 0 & 0 & \frac{1}{2} & 0 \\ 0 & 0 & \frac{1}{2} & 0 \end{pmatrix}, & \text{if } j \text{ is odd,} \end{cases} \\
 \\
 \begin{pmatrix} s_{2N+2j+2,2N-2j}^{-1} & \cdots & s_{2N+2j+2,2N-2j+3}^{-1} \\ \vdots & & \vdots \\ s_{2N+2j+5,2N-2j}^{-1} & \cdots & s_{2N+2j+5,2N-2j+3}^{-1} \end{pmatrix} &= \begin{cases} \begin{pmatrix} 0 & 0 & 0 & \frac{1}{2} \\ 0 & 0 & 0 & -\frac{1}{2} \\ \frac{1}{2} & 0 & 0 & 0 \\ \frac{1}{2} & 0 & 0 & 0 \end{pmatrix}, & \text{if } j \text{ is even,} \\ \begin{pmatrix} 0 & 0 & \frac{1}{2} & 0 \\ 0 & 0 & \frac{1}{2} & 0 \\ 0 & \frac{1}{2} & 0 & 0 \\ 0 & -\frac{1}{2} & 0 & 0 \end{pmatrix}, & \text{if } j \text{ is odd,} \end{cases} \\
 \\
 \begin{pmatrix} s_{2N+2j+2,2N+2j+2}^{-1} & \cdots & s_{2N+2j+2,2N+2j+5}^{-1} \\ \vdots & & \vdots \\ s_{2N+2j+5,2N+2j+2}^{-1} & \cdots & s_{2N+2j+5,2N+2j+5}^{-1} \end{pmatrix} &= \begin{cases} \begin{pmatrix} 0 & \frac{1}{2} & 0 & 0 \\ 0 & \frac{1}{2} & 0 & 0 \\ 0 & 0 & \frac{1}{2} & 0 \\ 0 & 0 & -\frac{1}{2} & 0 \end{pmatrix}, & \text{if } j \text{ is even,} \\ \begin{pmatrix} \frac{1}{2} & 0 & 0 & 0 \\ -\frac{1}{2} & 0 & 0 & 0 \\ 0 & 0 & 0 & \frac{1}{2} \\ 0 & 0 & 0 & \frac{1}{2} \end{pmatrix}, & \text{if } j \text{ is odd.} \end{cases}
 \end{aligned}$$

In addition, we have

$$s_{1,1}^{-1} = 1, \quad s_{2,2N+3}^{-1} = -2, \quad s_{2N+3,2N+2}^{-1} = 2.$$

All other entries are equal to zero. The structure of S^{-1} is illustrated for $N = 4$ in Figure 5.6.

section 5.5 to prove the hyperbolicity of the two-dimensional system of moment equations. The advection speeds $a(\theta) := -\sin \theta \cos \theta$ of the Smoluchowski equation in (3.3) satisfy

$$a(\theta) = a\left(\frac{\pi}{2} - \theta\right) = -a\left(\frac{\pi}{2} + \theta\right) = -a(\pi - \theta).$$

This symmetry is reflected in the eigenvalues of the coefficient matrix A .

5.8 Lemma. *If λ is an eigenvalue of A , then $-\lambda$ is also an eigenvalue of A .*

Proof. We show that the matrices A and $-A$ are similar, i.e. we provide a non-singular matrix S with $SAS^{-1} = -A$. It is easy to confirm that the similarity transformation is described by a diagonal matrix S with the diagonal entries of the form

$$\text{diag}(S) = (1, -1, -1, 1, 1, -1, -1, 1, 1, \dots).$$

□

5.4 Hierarchy of Moment Equations for General Two-Dimensional Flow

In this section, we derive a hierarchy of moment equations for the two-dimensional flow (3.2). Rewriting the Smoluchowski equation in (3.2) results in

$$\begin{aligned} \partial_t f &= \underbrace{D_r \partial_{\theta\theta} f}_1 - \underbrace{\partial_{\theta}(((w_z - ux) \cos \theta \sin \theta - u_z \sin^2 \theta + w_x \cos^2 \theta) f)}_2 \\ &\quad - \underbrace{\partial_x((u - \cos \theta \sin \theta) f)}_4 - \underbrace{\partial_z((w - (1 - \sin^2 \theta)) f)}_5. \end{aligned} \tag{5.12}$$

For the derivation of an evolution equation of the moment ρ in (5.1), we insert (5.12) in $\partial_t \rho$, integrate over S^1 and separately consider the five different contributions.

$$\begin{aligned} \partial_t \rho(x, z, t) &= \int_0^{2\pi} f(x, z, t, \theta) d\theta \\ &= \int_0^{2\pi} -\partial_x((u - \cos \theta \sin \theta) f) - \partial_z((w - (1 - \sin^2 \theta)) f) d\theta \\ &= \int_0^{2\pi} -u \partial_x f - u_x f + \frac{1}{2} \sin(2\theta) \partial_x f - \left(w - \frac{3}{2}\right) \partial_z f - w_z f - \partial_z \frac{1}{2} \cos(2\theta) f d\theta \\ &= -u_x \rho - u \partial_x \rho + \partial_x S_1 - \left(w - \frac{3}{2}\right) \partial_z \rho - w_z \rho - \partial_z C_1 \end{aligned}$$

Note that there is no contribution from (1)-(3) due to the periodicity of the solution. For the moments

$$\partial_t C_l(x, z, t) = \frac{1}{2} \int_0^{2\pi} \cos(2l\theta) \partial_t f(x, z, t) d\theta,$$

we proceed in a similar way.

Contribution of (1):

$$\begin{aligned} & \frac{1}{2} D_r \int_0^{2\pi} \cos(2l\theta) \partial_{\theta\theta} f d\theta \\ \stackrel{\text{part. int.}}{=} & -\frac{1}{2} D_r \int_0^{2\pi} 4l^2 \cos(2l\theta) f d\theta \\ = & -4l^2 D_r C_l \end{aligned}$$

Contribution of (2):

$$\begin{aligned} & -\frac{1}{2} \int_0^{2\pi} \cos(2l\theta) (w_z - u_x) \partial_{\theta} (\cos \theta \sin \theta) f d\theta \\ \stackrel{\text{part. int.}}{=} & -l \int_0^{2\pi} \sin(2l\theta) (w_z - u_x) \frac{1}{2} \sin(2\theta) f d\theta \\ = & \frac{l}{4} (w_z - u_x) (\cos(2(l-1)\theta) - \cos(2(l+1)\theta)) \\ = & \frac{l}{2} (w_z - u_x) (C_{l-1} - C_{l+1}) \end{aligned}$$

Contribution of (3):

$$\begin{aligned} & \frac{1}{2} \int_0^{2\pi} \cos(2l\theta) \partial_{\theta} (u_z \sin^2 \theta - w_x \cos^2 \theta) f d\theta \\ \stackrel{\text{part. int.}}{=} & l \int_0^{2\pi} \sin(2l\theta) u_z \sin^2(\theta) f d\theta - l \int_0^{2\pi} \sin(2l\theta) w_x \cos^2 \theta f d\theta \\ = & \frac{1}{4} u_z \int_0^{2\pi} (2l \sin(2l\theta) + l \sin(2(l-1)\theta) - l \sin(2(l+1)\theta)) f d\theta \\ & - \frac{1}{4} w_x \int_0^{2\pi} (2l \sin(2l\theta) - l \sin(2(l-1)\theta) + l \sin(2(l+1)\theta)) f d\theta \\ = & -\frac{l}{2} (u_z + w_x) S_{l-1} + l(u_z - w_x) S_l - \frac{l}{2} (u_z + w_x) S_{l+1} \end{aligned}$$

Contribution of (4):

$$\begin{aligned}
 & -\frac{1}{2} \int_0^{2\pi} \cos(2l\theta) \partial_x (u - \sin(2\theta)) f d\theta \\
 = & -\frac{1}{2} \int_0^{2\pi} \cos(2l\theta) (u_x f + u \partial_x f) d\theta + \frac{1}{2} \int_0^{2\pi} \cos(2l\theta) \partial_x (\sin(2\theta) f) d\theta \\
 = & -\frac{1}{2} \int_0^{2\pi} \cos(2l\theta) (u_x f + u \partial_x f) d\theta + \frac{1}{2} \int_0^{2\pi} \frac{1}{4} (\sin(2(l+1)\theta) - \sin(2(l-1)\theta)) \partial_x f d\theta \\
 = & -u_x C_l - u \partial_x C_l + \frac{1}{4} \partial_x (S_{l+1} - S_{l-1})
 \end{aligned}$$

Contribution of (5):

$$\begin{aligned}
 & -\frac{1}{2} \int_0^{2\pi} \cos(2l\theta) \partial_z \left(\left(w - (1 + \sin^2 \theta) \right) f \right) d\theta \\
 = & -\frac{1}{2} \int_0^{2\pi} \cos(2l\theta) (w_z f + w \partial_z f) + \frac{1}{2} \int_0^{2\pi} \cos(2l\theta) \partial_z f d\theta + \frac{1}{2} \int_0^{2\pi} \cos(2l\theta) \sin^2 \theta f d\theta \\
 = & -w_z C_l - w \partial_z C_l + \partial_z C_l + \frac{1}{2} \int_0^{2\pi} \frac{1}{4} (2 \cos(2l\theta) - \cos(2(l-1)\theta) - \cos(2(l+1)\theta)) \partial_z f d\theta \\
 = & -w_z C_l - \partial_z \left(w - \frac{3}{2} \right) C_l - \frac{1}{4} \partial_z C_{l-1} - \frac{1}{4} \partial_z C_{l+1}
 \end{aligned}$$

Combining all five contributions results in

$$\begin{aligned}
 \partial_t C_l = & -u \partial_x C_l + \frac{1}{4} \partial_x (S_{l+1} - S_{l-1}) - \partial_z \left(\frac{1}{4} C_{l-1} + \left(w - \frac{3}{2} \right) C_l + \frac{1}{4} C_{l+1} \right) \\
 & -\frac{l}{2} (w_z - u_x) C_{l-1} - (u_x + w_z) C_l + \frac{l}{2} (w_z - u_x) C_{l+1} \\
 & -\frac{l}{2} (u_z + w_x) S_{l-1} + l (u_z - w_x) S_l - \frac{l}{2} (u_z + w_x) S_{l+1} \\
 & -4l^2 D_r C_l, \quad l = 1, \dots, N.
 \end{aligned}$$

Analogously, we obtain

$$\begin{aligned}
 \partial_t S_l = & -u \partial_x S_l + \frac{1}{4} \partial_x (C_{l-1} - C_{l+1}) - \partial_z \left(\frac{1}{4} S_{l-1} + \left(w - \frac{3}{2} \right) C_l + \frac{1}{4} S_{l+1} \right) \\
 & -\frac{l}{2} (w_z - u_x) S_{l-1} - (u_x + w_z) S_l + \frac{l}{2} (w_z - u_x) S_{l+1} \\
 & -\frac{l}{2} (u_z + w_x) C_{l-1} - l (u_z - w_x) C_l + \frac{l}{2} (u_z + w_x) C_{l+1} \\
 & -4l^2 D_r C_l, \quad l = 1, \dots, N.
 \end{aligned}$$

Altogether, the system of moment equations for the two-dimensional flow problem takes the form

$$\begin{aligned}
 \partial_t \rho &= -u \partial_x \rho + \partial_x S_1 - \left(w - \frac{3}{2} \right) \partial_z \rho - \partial_z C_1 - (u_x - w_z) \rho, \\
 \partial_t C_l &= -u \partial_x C_l + \frac{1}{4} \partial_x (S_{l+1} - S_{l-1}) - \partial_z \left(\frac{1}{4} C_{l-1} + \left(w - \frac{3}{2} \right) C_l + \frac{1}{4} C_{l+1} \right) \\
 &\quad - \frac{l}{2} (w_z - u_x) C_{l-1} - (u_x + w_z) C_l + \frac{l}{2} (w_z - u_x) C_{l+1} \\
 &\quad - \frac{l}{2} (u_z + w_x) S_{l-1} + l (u_z - w_x) S_l - \frac{l}{2} (u_z + w_x) S_{l+1} \\
 &\quad - 4l^2 D_r C_l, \quad l = 1, \dots, N \\
 \partial_t S_l &= -u \partial_x S_l + \frac{1}{4} \partial_x (C_{l-1} - C_{l+1}) - \partial_z \left(\frac{1}{4} S_{l-1} + \left(w - \frac{3}{2} \right) C_l + \frac{1}{4} S_{l+1} \right) \\
 &\quad - \frac{l}{2} (w_z - u_x) S_{l-1} - (u_x + w_z) S_l + \frac{l}{2} (w_z - u_x) S_{l+1} \\
 &\quad - \frac{l}{2} (u_z + w_x) C_{l-1} - l (u_z - w_x) C_l + \frac{l}{2} (u_z + w_x) C_{l+1} \\
 &\quad - 4l^2 D_r C_l, \quad l = 1, \dots, N,
 \end{aligned} \tag{5.13}$$

with $C_0 = \frac{1}{2} \rho$, $S_0 = 0$. As explained in section 5.1, the system is closed with $C_{N+1} = S_{N+1} = 0$. We consider (5.13) together with the two-dimensional flow equation

$$\begin{aligned}
 \text{Re}(\partial_t u + u \partial_x u + w \partial_z u) + p_x &= u_{xx} + u_{zz}, \\
 \text{Re}(\partial_t w + u \partial_x w + w \partial_z w) + p_z &= w_{xx} + w_{zz} - \delta \rho, \\
 u_x + w_z &= 0.
 \end{aligned} \tag{5.14}$$

The moment system (5.13) is lower dimensional than the original kinetic equation (3.2).

5.5 Hyperbolic Structure of the Two-Dimensional System of Moment Equations

In this section, we prove the hyperbolicity of the two-dimensional system of moment equations (5.13) by using the hyperbolicity of the one-dimensional system (5.4).

For this purpose, we rewrite the system of moment equations (5.13) as

$$\partial_t Q(x, z, t) + A \partial_x Q + B \partial_z Q = \varphi(Q), \tag{5.15}$$

where Q is the vector of moments. For the approximation of the spatial transport term in x , we define $A \in \mathbb{R}^{(2N+1) \times (2N+1)}$ with

$$\begin{aligned} a_{1,3} &:= -1, \\ a_{3,1} &:= -\frac{1}{8}, \\ a_{ii} &:= u, & i = 1, \dots, 2N + 1, \\ \begin{pmatrix} a_{2(N-j)-2, 2(N-j)-2} & \cdots & a_{2(N-j)-2, 2(N-j)+1} \\ \vdots & & \vdots \\ a_{2(N-j)+1, 2(N-j)-2} & \cdots & a_{2(N-j)+1, 2(N-j)+1} \end{pmatrix} &:= \begin{pmatrix} 0 & 0 & 0 & -\frac{1}{4} \\ 0 & 0 & \frac{1}{4} & 0 \\ 0 & \frac{1}{4} & 0 & 0 \\ -\frac{1}{4} & 0 & 0 & 0 \end{pmatrix}, & j = 0, \dots, N - 2. \end{aligned} \tag{5.16}$$

The other entries of A are equal to zero. The approximation of the spatial transport term in y is described with a matrix $B \in \mathbb{R}^{(2N+1) \times (2N+1)}$ of the form

$$\begin{aligned} b_{1,2} &:= 1, \\ b_{2,1} &:= \frac{1}{8}, \\ b_{j,j+2} &:= \frac{1}{4}, & j = 2, \dots, 2N - 1, \\ b_{j+2,j} &:= \frac{1}{4}, & j = 2, \dots, 2N - 1, \\ b_{j,j} &:= w - \frac{3}{2}, & j = 1, \dots, 2N + 1. \end{aligned} \tag{5.17}$$

All other components of B are equal to zero.

5.9 Example. *The system of moment equations for the general two-dimensional flow problem for $N = 1$ is given as*

$$\begin{aligned} \partial_t \begin{pmatrix} \rho \\ c_1 \\ s_1 \end{pmatrix} + \underbrace{\begin{pmatrix} u & 0 & -1 \\ 0 & u & 0 \\ -\frac{1}{8} & 0 & u \end{pmatrix}}_{=A} \partial_x \begin{pmatrix} \rho \\ c_1 \\ s_1 \end{pmatrix} + \underbrace{\begin{pmatrix} -\frac{3}{2} + v & 1 & 0 \\ \frac{1}{8} & -\frac{3}{2} + v & 0 \\ 0 & 0 & -\frac{3}{2} + v \end{pmatrix}}_{=B} \partial_y \begin{pmatrix} \rho \\ c_1 \\ s_1 \end{pmatrix} \\ = \underbrace{\begin{pmatrix} 0 & 0 & 0 \\ -\frac{1}{4}(v_y - u_x) & -4D_r & u_y - v_x \\ \frac{1}{4}(u_y + v_x) & -u_y + v_x & -4D_r \end{pmatrix}}_{=\varphi(Q)} \begin{pmatrix} \rho \\ c_1 \\ s_1 \end{pmatrix}. \end{aligned}$$

To prove the hyperbolic structure of the two-dimensional system of moment equations (5.15), we need to show that each matrix of the form $n_1 A + n_2 B$ with $n_1^2 + n_2^2 = 1$ is diagonalisable

with real eigenvalues. The idea of the proof of the hyperbolicity of the system (5.15) is motivated in the following remark.

5.10 Remark. From the derivation of the moment system one can see that the homogeneous system was obtained from subproblem (4.7) and the source term was obtained from subproblem (4.6).

Using a change of variables of the form $\hat{x} = x - u$ and $\hat{y} = y - \left(w - \frac{3}{2}\right)$ and some simple trigonometric identities, equation (4.7) can be written in the form

$$\partial_t f + \partial_{\hat{x}} \left(-\frac{1}{2} \sin(2\theta) f \right) + \partial_{\hat{y}} \left(\frac{1}{2} \cos(2\theta) f \right) = 0. \quad (5.18)$$

For every value of $\theta \in [0, 2\pi]$, we have a linear two-dimensional advection equation with advection speeds between $-\frac{1}{2}$ and $\frac{1}{2}$. Furthermore, in any direction $\mathbf{n} = (\cos(\varphi), \sin(\varphi))$, $\varphi \in [0, 2\pi]$, we obtain an advection equation with propagation speed

$$-\frac{1}{2} \sin(2\theta) \cos(\varphi) + \frac{1}{2} \cos(2\theta) \sin(\varphi) = \frac{1}{2}(\varphi - \theta),$$

i.e. the propagation speeds arising in any direction of the transformed two-dimensional problem (5.18) agree with those of the one-dimensional shear flow problem.

We will now show that this structure can also be seen in the transport part of the moment equations. This will lead us to the proof of hyperbolicity.

5.11 Remark. The matrix $A - uI$, with A as defined in (5.16) and I the $(2N + 1) \times (2N + 1)$ identity matrix, agrees with the coefficient matrix (5.7) of the one-dimensional system.

5.12 Lemma. Let $\bar{\bar{A}} := A - uI$ and $\bar{\bar{B}} := B - \left(w - \frac{3}{2}\right) I$, with A and B as defined in (5.16) and (5.17). The matrices $\bar{\bar{A}}$ and $\bar{\bar{B}}$ are similar.

Proof. We describe the form of a nonsingular matrix $S \in \mathbb{R}^{(2N+1) \times (2N+1)}$ such that

$$\bar{\bar{B}} = S \bar{\bar{A}} S^{-1}.$$

It is instructive to consider the cases $N \leq 6$. For $N = 6$, the matrix $\bar{\bar{A}}$ has the form

$$\bar{\bar{A}} = \begin{pmatrix} 0 & 0 & -1 & 0 & 0 & 0 & 0 & 0 & 0 & 0 & 0 & 0 & 0 \\ 0 & 0 & 0 & 0 & -\frac{1}{4} & 0 & 0 & 0 & 0 & 0 & 0 & 0 & 0 \\ -\frac{1}{8} & 0 & 0 & \frac{1}{4} & 0 & 0 & 0 & 0 & 0 & 0 & 0 & 0 & 0 \\ 0 & 0 & -\frac{1}{4} & 0 & 0 & 0 & -\frac{1}{4} & 0 & 0 & 0 & 0 & 0 & 0 \\ 0 & -\frac{1}{4} & 0 & 0 & 0 & \frac{1}{4} & 0 & 0 & 0 & 0 & 0 & 0 & 0 \\ 0 & 0 & 0 & 0 & \frac{1}{4} & 0 & 0 & 0 & -\frac{1}{4} & 0 & 0 & 0 & 0 \\ 0 & 0 & 0 & -\frac{1}{4} & 0 & 0 & 0 & \frac{1}{4} & 0 & 0 & 0 & 0 & 0 \\ 0 & 0 & 0 & 0 & 0 & 0 & \frac{1}{4} & 0 & 0 & 0 & -\frac{1}{4} & 0 & 0 \\ 0 & 0 & 0 & 0 & 0 & -\frac{1}{4} & 0 & 0 & 0 & \frac{1}{4} & 0 & 0 & 0 \\ 0 & 0 & 0 & 0 & 0 & 0 & 0 & 0 & \frac{1}{4} & 0 & 0 & 0 & -\frac{1}{4} \\ 0 & 0 & 0 & 0 & 0 & 0 & 0 & -\frac{1}{4} & 0 & 0 & 0 & \frac{1}{4} & 0 \\ 0 & 0 & 0 & 0 & 0 & 0 & 0 & 0 & 0 & 0 & \frac{1}{4} & 0 & 0 \\ 0 & 0 & 0 & 0 & 0 & 0 & 0 & 0 & 0 & -\frac{1}{4} & 0 & 0 & 0 \end{pmatrix}.$$

In order to move the entries $-\frac{1}{8}$ and -1 to the positions they have in the matrix $\bar{\bar{B}}$, we change the second and the third row as well as the second and third column. The correct sign is obtained by multiplying the first row and first column by -1 . These changes describe the similarity transformation for $N = 1$, i.e. $\bar{\bar{B}} = S_1 \bar{\bar{A}} S_1^{-1}$ with

$$S_1 = S_1^{-1} = \begin{pmatrix} -1 & 0 & 0 \\ 0 & 0 & 1 \\ 0 & 1 & 0 \end{pmatrix}.$$

For $N > 1$, the 3×3 matrix S_1 is the third order principal submatrix of the matrix which describes the similarity transformation. For $N > 1$, the change of the second and third row and second and third column also effects other nonzero values. After the row and column change, all the nonzero values in the second and third row and second and third column are already at the correct position.

For $N = 6$, the remaining nonzero values of $\bar{\bar{A}}$ are moved to the correct position by additionally changing the rows and columns 6 and 7 as well as 10 and 11. All of the so far discussed

$$S = \begin{pmatrix} \sin(2\theta) & 0 & 0 \\ 0 & \cos(\theta) \cos(2\theta) & \sin(\theta) \cos(2\theta) \\ 0 & -\sin(\theta) \sin(2\theta) & \cos(\theta) \sin(2\theta) \end{pmatrix},$$

$$S^{-1} = \begin{pmatrix} \frac{1}{\sin(2\theta)} & 0 & 0 \\ 0 & \frac{\cos(\theta)}{\cos(2\theta)} & -\frac{1}{2 \cos(\theta)} \\ 0 & \frac{\sin(\theta)}{\cos(2\theta)} & \frac{1}{2 \sin(\theta)} \end{pmatrix}.$$

A straight forward computation confirms

$$SCS^{-1} = \begin{pmatrix} 0 & 0 & -1 \\ 0 & 0 & 0 \\ -\frac{1}{8} & 0 & 0 \end{pmatrix}.$$

The computation presented for $N = 1$ is extended to general N . The proof is split in three steps. First, we introduce the general structure of the similarity transformation matrices S and S^{-1} . Second, we define the matrix $C := n_1 \bar{A} + n_2 \bar{B}$ for general N . Third, we use the structure of S , C and S^{-1} to describe the general matrix-matrix product SCS^{-1} .

1. Structure of S and S^{-1} for general N .

We define the similarity transformation matrix $S \in \mathbb{R}^{(2N+1) \times (2N+1)}$ as

$$s_{1,1} = \sin(2\theta),$$

$$\begin{pmatrix} s_{2i,2i} & s_{2i,2i+1} \\ s_{2i+1,2i} & s_{2i+1,2i+1} \end{pmatrix} = \begin{cases} \begin{pmatrix} \cos(i\theta) \cos(2\theta) & \sin(i\theta) \cos(2\theta) \\ -\sin(i\theta) \sin(2\theta) & \cos(i\theta) \sin(2\theta) \end{pmatrix}, & \text{for } i \text{ odd,} \\ \begin{pmatrix} \cos(i\theta) \sin(2\theta) & \sin(i\theta) \sin(2\theta) \\ -\sin(i\theta) \cos(2\theta) & \cos(i\theta) \cos(2\theta) \end{pmatrix}, & \text{for } i \text{ even.} \end{cases} \quad (5.19)$$

All other components of S are equal to zero. It is easy to see that the inverse of S has the

non-zero components

$$\begin{aligned}
 s_{1,1}^{-1} &= \frac{1}{\sin(2\theta)}, \\
 \begin{pmatrix} s_{2i,2i} & s_{2i,2i+1} \\ s_{2i+1,2i} & s_{2i+1,2i+1} \end{pmatrix} &= \begin{cases} \begin{pmatrix} \frac{\cos(i\theta)}{\cos(2\theta)} & -\frac{\sin(i\theta)}{\sin(2\theta)} \\ \frac{\sin(i\theta)}{\cos(2\theta)} & \frac{\cos(i\theta)}{\sin(2\theta)} \end{pmatrix}, & \text{for } i \text{ odd,} \\ \begin{pmatrix} \frac{\cos(i\theta)}{\sin(2\theta)} & -\frac{\sin(i\theta)}{\cos(2\theta)} \\ \frac{\sin(i\theta)}{\sin(2\theta)} & \frac{\cos(i\theta)}{\cos(2\theta)} \end{pmatrix}, & \text{for } i \text{ even.} \end{cases} \quad (5.20)
 \end{aligned}$$

2. Structure of C for general N :

In the general case, the $(2N + 1) \times (2N + 1)$ matrix $C = \cos(\theta)A + \sin(\theta)B$ has the form

$$C = \begin{pmatrix} 0 & \sin(\theta) & -\cos(\theta) & & & \\ \frac{1}{8}\sin(\theta) & 0 & 0 & D_1 & & \\ -\frac{1}{8}\cos(\theta) & 0 & 0 & & & \\ & & D_2 & \cdots & \cdots & \\ & & & \cdots & \cdots & D_1 \\ & & & & D_2 & 0 \end{pmatrix}$$

with $N - 1$ blocks of the form

$$D_1 := \begin{pmatrix} \frac{1}{4}\sin(\theta) & -\frac{1}{4}\cos(\theta) \\ \frac{1}{4}\cos(\theta) & \frac{1}{4}\sin(\theta) \end{pmatrix}, \quad D_2 := \begin{pmatrix} \frac{1}{4}\sin(\theta) & \frac{1}{4}\cos(\theta) \\ -\frac{1}{4}\cos(\theta) & \frac{1}{4}\sin(\theta) \end{pmatrix}.$$

3. Multiplication of S , C and S^{-1} for general N :

The above computation in the case $N = 1$ arises as a subproblem of larger values of N . This follows from the structure of C , S , S^{-1} . In addition, for $N > 1$ the multiplication of the second and third row of S leads to additional nonzero components when multiplied with the

fourth and fifth columns of C . We obtain

$$\begin{aligned}
 (SC)_{2,4} &= \cos(\theta) \cos(2\theta) \frac{1}{4} \sin(\theta) + \sin(\theta) \cos(2\theta) \frac{1}{4} \cos(\theta) \\
 &= \frac{\sin(4\theta)}{8}, \\
 (SC)_{2,5} &= \cos(\theta) \cos(2\theta) \left(-\frac{1}{4} \cos(\theta)\right) + \sin(\theta) \cos(2\theta) \frac{1}{4} \sin(\theta) \\
 &= -\frac{\cos^2(2\theta)}{4}, \\
 (SC)_{3,4} &= -\sin(\theta) \sin(2\theta) \frac{1}{4} \sin(\theta) + \cos(\theta) \sin(2\theta) \frac{1}{4} \cos(\theta) \\
 &= \frac{\sin(4\theta)}{8}, \\
 (SC)_{3,5} &= -\sin(\theta) \sin(2\theta) \left(-\frac{1}{4} \cos(\theta)\right) + \cos(\theta) \sin(2\theta) \frac{1}{4} \sin(\theta) \\
 &= \frac{1}{8} - \frac{\cos(4\theta)}{8}.
 \end{aligned}$$

These nonzero entries in the second and third row of SC lead to nonzero contributions in SCS^{-1} of the form

$$\begin{array}{c} 2 \\ 3 \end{array} \begin{array}{cc} 4 & 5 \\ \left(\begin{array}{cc} \frac{\sin(4\theta)}{8} & -\frac{\cos^2(2\theta)}{4} \\ \frac{\sin(4\theta)}{8} & \frac{1 - \cos(4\theta)}{8} \end{array} \right) \end{array} \cdot \begin{array}{c} 2 \\ 3 \end{array} \begin{array}{cc} 4 & 5 \\ \left(\begin{array}{cc} \frac{\sin(4\theta)}{8} & -\frac{\cos^2(2\theta)}{4} \\ \frac{\sin(4\theta)}{8} & \frac{1 - \cos(4\theta)}{8} \end{array} \right) \end{array} = \begin{array}{c} 2 \\ 3 \end{array} \begin{array}{cc} 4 & 5 \\ \left(\begin{array}{cc} 0 & -\frac{1}{4} \\ \frac{1}{4} & 0 \end{array} \right) \end{array},$$

i.e. the first three rows of SCS^{-1} agree with the first three rows of the coefficient matrix A of the one-dimensional problem described in (5.7).

Now, we consider the product of the rows $2i, 2i + 1, 2i + 2$ and $2i + 3$ of S as described in (5.20) with the matrix C . Without loss of generalisation we can restrict our considerations to the case of even i . The nonzero entries of the considered rows of S are

$$\begin{array}{c} 2i \\ 2i + 1 \\ 2i + 2 \\ 2i + 3 \end{array} \left(\begin{array}{cccc} & 2i & 2i + 1 & & 2i + 2 & & 2i + 3 \\ \cos(i\theta) \sin(2\theta) & & \sin(i\theta) \sin(2\theta) & & & & \\ -\sin(i\theta) \cos(2\theta) & & \cos(i\theta) \cos(2\theta) & & & & \\ & & & & \cos((i + 1)\theta) \cos(2\theta) & & \sin((i + 1)\theta) \cos(2\theta) \\ & & & & -\sin((i + 1)\theta) \sin(2\theta) & & \cos((i + 1)\theta) \sin(2\theta) \end{array} \right).$$

Nonzero matrix elements are obtained for the product of rows $2i$ and $2i + 1$ of S with columns $2i - 2, 2i - 1, 2i + 2$ and $2i + 3$ of C and for the product of rows $2i + 2$ and $2i + 3$ of S with the columns $2i, 2i + 1, 2i + 4$ and $2i + 5$ of C . We start with the rows $2i$ and $2i + 1$ of S and obtain

$$\begin{aligned} (SC)_{2i,2i-2} &= \cos(i\theta) \sin(2\theta) \frac{1}{4} \sin(\theta) - \sin(i\theta) \sin(2\theta) \frac{1}{4} \cos(\theta) \\ &= -\frac{\sin((i-1)\theta) \sin(2\theta)}{4}, \end{aligned}$$

$$\begin{aligned} (SC)_{2i,2i-1} &= \cos(i\theta) \sin(2\theta) \frac{1}{4} \cos(\theta) + \sin(i\theta) \sin(2\theta) \frac{1}{4} \sin(\theta) \\ &= \frac{\cos((i-1)\theta) \sin(2\theta)}{4}, \end{aligned}$$

$$\begin{aligned} (SC)_{2i,2i+2} &= \cos(i\theta) \sin(2\theta) \frac{1}{4} \sin(\theta) + \sin(i\theta) \sin(2\theta) \frac{1}{4} \cos(\theta) \\ &= \frac{\sin((i+1)\theta) \sin(2\theta)}{4}, \end{aligned}$$

$$\begin{aligned} (SC)_{2i,2i+3} &= -\cos(i\theta) \sin(2\theta) \frac{1}{4} \cos(\theta) + \sin(i\theta) \sin(2\theta) \frac{1}{4} \sin(\theta) \\ &= -\frac{\cos((i+1)\theta) \sin(2\theta)}{4}, \end{aligned}$$

$$\begin{aligned} (SC)_{2i+1,2i-2} &= -\sin(i\theta) \cos(2\theta) \frac{1}{4} \sin(\theta) - \cos(i\theta) \cos(2\theta) \frac{1}{4} \cos(\theta) \\ &= -\frac{\cos((i-1)\theta) \cos(2\theta)}{4}, \end{aligned}$$

$$\begin{aligned} (SC)_{2i+1,2i-1} &= -\sin(i\theta) \cos(2\theta) \frac{1}{4} \cos(\theta) + \cos(i\theta) \cos(2\theta) \frac{1}{4} \sin(\theta) \\ &= -\frac{\sin((i-1)\theta) \cos(2\theta)}{4}, \end{aligned}$$

$$\begin{aligned} (SC)_{2i+1,2i+2} &= -\sin(i\theta) \cos(2\theta) \frac{1}{4} \cos(\theta) + \cos(i\theta) \cos(2\theta) \frac{1}{4} \cos(\theta) \\ &= \frac{\cos((i+1)\theta) \cos(2\theta)}{4}, \end{aligned}$$

$$\begin{aligned} (SC)_{2i+1,2i+3} &= \sin(i\theta) \cos(2\theta) \frac{1}{4} \cos(\theta) + \cos(i\theta) \cos(2\theta) \frac{1}{4} \sin(\theta) \\ &= \frac{\sin((i+1)\theta) \cos(2\theta)}{4}. \end{aligned}$$

From the structure of S^{-1} , see (5.20), we see that it is enough to consider

$$\begin{pmatrix} (SC)_{2i,2i-2} & (SC)_{2i,2i-1} \\ (SC)_{2i+1,2i-2} & (SC)_{2i+1,2i-1} \end{pmatrix} \begin{pmatrix} (S^{-1})_{2i-2,2i-2} & (S^{-1})_{2i-2,2i-1} \\ (S^{-1})_{2i-1,2i-2} & (S^{-1})_{2i-1,2i-1} \end{pmatrix} \quad (5.21)$$

and

$$\begin{pmatrix} (SC)_{2i,2i+2} & (SC)_{2i,2i+3} \\ (SC)_{2i+1,2i+2} & (SC)_{2i+1,2i+3} \end{pmatrix} \begin{pmatrix} (S^{-1})_{2i+2,2i+2} & (S^{-1})_{2i+2,2i+3} \\ (S^{-1})_{2i+3,2i+2} & (S^{-1})_{2i+3,2i+3} \end{pmatrix}. \quad (5.22)$$

All other entries of rows $2i$ and $2i+1$ of SCS^{-1} are equal to zero. Recall that we still consider the case i even, i.e. $i-1$ and $i+1$ odd. For (5.21), we then obtain

$$\begin{aligned} & \frac{1}{4} \begin{pmatrix} -\sin((i-1)\theta) \sin(2\theta) & \cos((i-1)\theta) \sin(2\theta) \\ -\cos((i-1)\theta) \cos(2\theta) & -\sin((i-1)\theta) \cos(2\theta) \end{pmatrix} \begin{pmatrix} \frac{\cos((i-1)\theta)}{\cos(2\theta)} & -\frac{\sin((i-1)\theta)}{\sin(2\theta)} \\ \frac{\sin((i-1)\theta)}{\cos(2\theta)} & \frac{\cos((i-1)\theta)}{\sin(2\theta)} \end{pmatrix} \\ &= \begin{pmatrix} 0 & \frac{1}{4} \\ -\frac{1}{4} & 0 \end{pmatrix}, \end{aligned}$$

and for (5.22) we get

$$\begin{aligned} & \frac{1}{4} \begin{pmatrix} \sin((i+1)\theta) \sin(2\theta) & -\cos((i+1)\theta) \sin(2\theta) \\ \cos((i+1)\theta) \cos(2\theta) & \sin((i+1)\theta) \cos(2\theta) \end{pmatrix} \begin{pmatrix} \frac{\cos((i+1)\theta)}{\cos(2\theta)} & -\frac{\sin((i+1)\theta)}{\sin(2\theta)} \\ \frac{\sin((i+1)\theta)}{\cos(2\theta)} & \frac{\cos((i+1)\theta)}{\sin(2\theta)} \end{pmatrix} \\ &= \begin{pmatrix} 0 & -\frac{1}{4} \\ \frac{1}{4} & 0 \end{pmatrix}. \end{aligned}$$

Now, we consider the product of rows $2i+2$ and $2i+3$ of S with the columns $2i$, $2i+1$, $2i+4$ and $2i+5$ of C

$$\begin{aligned} (SC)_{2i+2,2i} &= \cos((i+1)\theta) \cos(2\theta) \frac{1}{4} \sin(\theta) - \sin((i+1)\theta) \cos(2\theta) \frac{1}{4} \cos(\theta) \\ &= \frac{1}{4} \cos(2\theta) ((\cos(i\theta) \cos(\theta) - \sin(i\theta) \sin(\theta)) \sin(\theta) \\ &\quad - (\sin(i\theta) \cos(\theta) + \cos(i\theta) \sin(\theta)) \cos(\theta)) \\ &= \frac{1}{4} \cos(2\theta) (-\sin(i\theta) \sin^2(\theta) - \sin(i\theta) \cos^2(\theta)) \\ &= -\frac{\sin(i\theta) \cos(2\theta)}{4}, \end{aligned}$$

$$\begin{aligned}
 (SC)_{2i+2,2i+1} &= \cos((i+1)\theta) \cos(2\theta) \frac{1}{4} \cos(\theta) + \sin((i+1)\theta) \cos(2\theta) \frac{1}{4} \sin(\theta) \\
 &= \frac{\cos(i\theta) \cos(2\theta)}{4}, \\
 (SC)_{2i+2,2i+4} &= \cos((i+1)\theta) \cos(2\theta) \frac{1}{4} \sin(\theta) + \sin((i+1)\theta) \cos(2\theta) \frac{1}{4} \cos(\theta) \\
 &= \frac{\sin((i+2)\theta) \cos(2\theta)}{4}, \\
 (SC)_{2i+2,2i+5} &= -\cos((i+1)\theta) \cos(2\theta) \frac{1}{4} \cos(\theta) + \sin((i+1)\theta) \cos(2\theta) \frac{1}{4} \sin(\theta) \\
 &= -\frac{\cos((i+2)\theta) \cos(2\theta)}{4}, \\
 (SC)_{2i+3,2i} &= -\sin((i+1)\theta) \sin(2\theta) \frac{1}{4} \sin(\theta) + \cos((i+1)\theta) \sin(2\theta) \left(-\frac{1}{4} \cos(\theta)\right) \\
 &= -\frac{\cos(i\theta) \sin(2\theta)}{4}, \\
 (SC)_{2i+3,2i+1} &= -\sin((i+1)\theta) \sin(2\theta) \frac{1}{4} \cos(\theta) + \cos((i+1)\theta) \sin(2\theta) \frac{1}{4} \sin(\theta) \\
 &= -\frac{\sin(i\theta) \sin(2\theta)}{4}, \\
 (SC)_{2i+3,2i+4} &= -\sin((i+1)\theta) \sin(2\theta) \frac{1}{4} \sin(\theta) + \cos((i+1)\theta) \sin(2\theta) \frac{1}{4} \cos(\theta) \\
 &= \frac{\cos((i+2)\theta) \sin(2\theta)}{4}, \\
 (SC)_{2i+3,2i+5} &= -\sin((i+1)\theta) \sin(2\theta) \left(-\frac{1}{4} \cos(\theta)\right) + \cos((i+1)\theta) \sin(2\theta) \frac{1}{4} \sin(\theta) \\
 &= \frac{\sin((i+2)\theta) \sin(2\theta)}{4}.
 \end{aligned}$$

Finally, we multiply with the appropriate entries of S^{-1} , i.e. we compute

$$\begin{aligned}
 &\begin{pmatrix} (SC)_{2i+2,2i} & (SC)_{2i+2,2i+1} \\ (SC)_{2i+3,2i} & (SC)_{2i+3,2i+1} \end{pmatrix} \begin{pmatrix} (S^{-1})_{2i,2i} & (S^{-1})_{2i,2i+1} \\ (S^{-1})_{2i+1,2i} & (S^{-1})_{2i+1,2i+1} \end{pmatrix} \\
 &= \frac{1}{4} \begin{pmatrix} -\sin(i\theta) \cos(2\theta) & \cos(i\theta) \cos(2\theta) \\ -\cos(i\theta) \sin(2\theta) & -\sin(i\theta) \sin(2\theta) \end{pmatrix} \begin{pmatrix} \frac{\cos(i\theta)}{\sin(2\theta)} & -\frac{\sin(i\theta)}{\cos(2\theta)} \\ \frac{\sin(i\theta)}{\sin(2\theta)} & \frac{\cos(i\theta)}{\cos(2\theta)} \end{pmatrix} \\
 &= \begin{pmatrix} 0 & \frac{1}{4} \\ -\frac{1}{4} & 0 \end{pmatrix}
 \end{aligned}$$

and

$$\begin{aligned}
 & \begin{pmatrix} (SC)_{2i+2,2i+4} & (SC)_{2i+2,2i+5} \\ (SC)_{2i+3,2i+4} & (SC)_{2i+3,2i+5} \end{pmatrix} \begin{pmatrix} (S^{-1})_{2i+4,2i+4} & (S^{-1})_{2i+4,2i+5} \\ (S^{-1})_{2i+5,2i+4} & (S^{-1})_{2i+5,2i+5} \end{pmatrix} \\
 &= \frac{1}{4} \begin{pmatrix} \sin((i+2)\theta) \cos(2\theta) & -\cos((i+2)\theta) \cos(2\theta) \\ \cos((i+2)\theta) \sin(2\theta) & \sin((i+2)\theta) \sin(2\theta) \end{pmatrix} \begin{pmatrix} \frac{\cos((i+2)\theta)}{\sin(2\theta)} & -\frac{\sin((i+2)\theta)}{\cos(2\theta)} \\ \frac{\sin((i+2)\theta)}{\sin(2\theta)} & \frac{\cos((i+2)\theta)}{\cos(2\theta)} \end{pmatrix} \\
 &= \begin{pmatrix} 0 & -\frac{1}{4} \\ \frac{1}{4} & 0 \end{pmatrix}.
 \end{aligned}$$

Thus, nonzero entries of SCS^{-1} in rows $2i, 2i+1, 2i+2$ and $2i+3$ have the form

$$\begin{array}{cccccccc}
 & 2i-2 & 2i-1 & 2i & 2i+1 & 2i+2 & 2i+3 & 2i+4 & 2i+5 \\
 2i & \begin{pmatrix} 0 & \frac{1}{4} & 0 & 0 & 0 & -\frac{1}{4} & 0 & 0 \end{pmatrix} \\
 2i+1 & \begin{pmatrix} -\frac{1}{4} & 0 & 0 & 0 & \frac{1}{4} & 0 & 0 & 0 \end{pmatrix} \\
 2i+2 & \begin{pmatrix} 0 & 0 & 0 & \frac{1}{4} & 0 & 0 & 0 & -\frac{1}{4} \end{pmatrix} \\
 2i+3 & \begin{pmatrix} 0 & 0 & -\frac{1}{4} & 0 & 0 & 0 & \frac{1}{4} & 0 \end{pmatrix}
 \end{array}$$

□

5.14 Theorem. *The two-dimensional system of moment equations (5.13) is hyperbolic.*

Proof. To prove the hyperbolicity of the two-dimensional system (5.13), we show that each matrix of the form

$$n_1A + n_2B,$$

with $n_1, n_2 \in \mathbb{R}$, $n_1^2 + n_2^2 = 1$, and A and B as defined in (5.16) and (5.17) is diagonalisable with real eigenvalues. Therefore, we use the relation to $\bar{\bar{A}}$ and $\bar{\bar{B}}$. We have

$$n_1A + n_2B = n_1 \left(\bar{\bar{A}} + uI \right) + n_2 \left(\bar{\bar{B}} + \left(w - \frac{3}{2} \right) I \right) = n_1 \bar{\bar{A}} + n_2 \bar{\bar{B}} + \left(n_1u + n_2w - \frac{3}{2}n_2 \right) I.$$

With Lemma 5.13, the matrix $n_1 \bar{\bar{A}} + n_2 \bar{\bar{B}}$ is similar to the coefficient matrix of the one-dimensional problem for n_1 and n_2 both not equal to zero. The special cases $n_2 = 0$ or $n_1 = 0$ have been studied separately in Lemma 5.8 and Lemma 5.12. Since the one-dimensional problem is hyperbolic, see Theorem 5.7, $n_1 \bar{\bar{A}} + n_2 \bar{\bar{B}}$ is diagonalisable with real eigenvalues.

The eigenvalues of $n_1\bar{\bar{A}} + n_2\bar{\bar{B}}$ have the form

$$\lambda + \left(n_1u + n_2w - \frac{3}{2}n_2 \right),$$

where λ is the eigenvalue of the one-dimensional coefficient matrix. The eigenvectors do not change by adding a multiple of the identity matrix. \square

Numerical Discretisation of the Coupled Moment System

The aim of this chapter is to show that the lower dimensional mathematical model, based on a hyperbolic hierarchy of moment equations, can be interpreted as an approximation of the detailed kinetic model and leads to accurate results in the analysis of test cases motivated by physical problems such as the cluster formation during sedimentation in suspensions of rod-like particles [28] or the instability of initially spherical clouds of rigid rod [70]. The main results presented in this chapter are based on [24, section 5] and explained in more detail here.

In section 6.1 and section 6.2, we study the numerical discretisation of the one- and two-dimensional hyperbolic moment systems coupled to the diffusion equation (5.5) or the two-dimensional Navier-Stokes equation (5.14). Subsequently in section 6.3, we compare the numerical solution of the moment systems with the approximations of the detailed kinetic models, described in chapter 4. Finally in section 6.4, we analyse test cases motivated from the physical phenomena described in section 1.1 with the one- and two-dimensional coupled moment systems and study the accuracy of the methods.

6.1 Numerical Discretisation of the Coupled Moment System for Shear Flow

In this section, we compute the numerical solution of the coupled moment system

$$\begin{aligned} \partial_t Q(\mathbf{x}, t) + A \partial_x Q(\mathbf{x}, t) &= \varphi(Q(\mathbf{x}, t)), \\ \text{Re } \partial_t w(x, t) &= \partial_{xx} w(x, t) + \delta(\bar{\rho} - \rho(\mathbf{x}, t)), \end{aligned} \tag{6.1}$$

where the hyperbolic coefficient matrix $A \in \mathbb{R}^{(2N+1) \times (2N+1)}$ is defined as in (5.7).

We discretise the spatial domain $\Omega = [x_l, x_r]$ and the time variable t in the same way as described in section 2.2. We define the discrete values of the velocity $w(x, t)$ and of the vector of moments $Q(x, t)$ on a staggered grid as visualised in Figure 6.1.

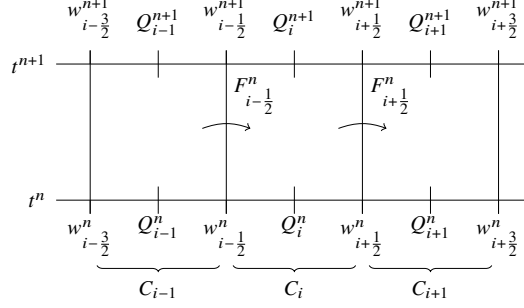


Figure 6.1.: Illustration of the staggered grid used for the discretisation of (6.1).

The discrete value of the velocity at time t^n is stored at the nodes of the grid, i.e.

$$w_{i+\frac{1}{2}}^n \approx w\left(x_{i+\frac{1}{2}}, t^n\right), \quad i = 1, \dots, m+1$$

approximates the point value on the interface $x_{i+\frac{1}{2}}$ at time t^n . The discrete value of the moments at time t^n is stored at the midpoints of the grid cell, i.e.

$$Q_i^n \approx \frac{1}{\Delta x} \int_{x_{i-\frac{1}{2}}}^{x_{i+\frac{1}{2}}} Q(x, t^n) dx \approx Q(x_i, t^n), \quad i = 1, \dots, m$$

approximates the cell average in cell C_i at time t^n . The midpoints of the cells are given as

$$x_i := \frac{x_{i+\frac{1}{2}} - x_{i-\frac{1}{2}}}{2}.$$

We compute the numerical solution of (6.1) with an operator splitting method in which we separately approximate the different components of the coupled moment system. The different steps of the algorithm for solving the coupled moment system for one time step are presented in Algorithm 1. The approach is comparable to the splitting method presented by Cheng and Knorr [14] for the Vlasov-Poisson equation. While in [73] a Poisson equation is considered, we have an inhomogeneous diffusion equation. For each time step, the update of the discrete velocity field $w(x, t)$ is computed with the Crank-Nicolson method for periodic solutions (see section 4.1). This solution is used to calculate

$$w_x(x_i, t^n) = \frac{w_{i+\frac{1}{2}}^n - w_{i-\frac{1}{2}}^n}{\Delta x}, \quad i = 1, \dots, m.$$

Algorithm 1 Operator splitting algorithm for solving the coupled moment system (6.1).

1. $\frac{1}{2}\Delta t$ step on $w_t(x, t) - w_{xx}(x, t) = 0$. Calculate $w_x(x, t)$.
 2. $\frac{1}{2}\Delta t$ step on $\partial_t Q(x, t) = \varphi(Q(x, t))$.
 3. $\frac{1}{2}\Delta t$ step on $w_t(x, t) = \delta(\bar{\rho} - \rho)$.
 4. Δt step on $\partial_t Q(x, t) + A\partial_x Q(x, t) = 0$.
 5. $\frac{1}{2}\Delta t$ step on $w_t(x, t) - w_{xx}(x, t) = 0$. Calculate $w_x(x, t)$.
 6. $\frac{1}{2}\Delta t$ step on $\partial_t Q(x, t) = \varphi(Q(x, t))$.
 7. $\frac{1}{2}\Delta t$ step on $w_t(x, t) = \delta(\bar{\rho} - \rho)$.
-

The system of ordinary differential equations resulting from the source term of the moment system is solved with a solver of second order. We calculate the solution of the homogeneous system of moment equations with the high-resolution Wave Propagation Algorithm by LeVeque, described in section 2.2. The accuracy of this approach will be tested in numerical simulations in section 6.4.

Compared to the discretisation of the detailed model, presented in chapter 4, the calculation of the numerical solution of the coupled moment system (6.1) is simpler and computationally less expensive.

6.2 Numerical Discretisation of the Coupled Moment System for General Two-Dimensional Flow

We present the numerical approach to solve the coupled moment system for the two-dimensional flow problem

$$\begin{aligned}
 \partial_t Q(x, z, t) + A\partial_x Q + B\partial_y Q &= \varphi(Q), \\
 \text{Re}(\partial_t u + u\partial_x u + w\partial_z u) + p_x &= u_{xx} + u_{zz}, \\
 \text{Re}(\partial_t w + u\partial_x w + w\partial_z w) + p_z &= w_{xx} + w_{zz} - \delta\rho, \\
 u_x + w_z &= 0,
 \end{aligned} \tag{6.2}$$

where $A \in \mathbb{R}^{(2N+1) \times (2N+1)}$ is defined as in (5.16) and $B \in \mathbb{R}^{(2N+1) \times (2N+1)}$ as in (5.17).

The spatial domain $[x_l, x_r] \times [y_l, y_r]$ and the time variable t are discretised as in section 2.3. We define the discrete cell average velocities $(U_{i,j}^n, V_{i,j}^n)$ as in (2.34) and the discrete edge velocities $(u_{i-1/2,j}^n, v_{i,j-1/2}^n)$ as in (2.35). The discrete vector of moments $Q_{i,j}^n$ is also defined as a cell average as in (2.21). As described in section 2.5, the scalar function $\varphi_{i,j}$ is a cell average, too. The notation is illustrated in Figure 6.2.

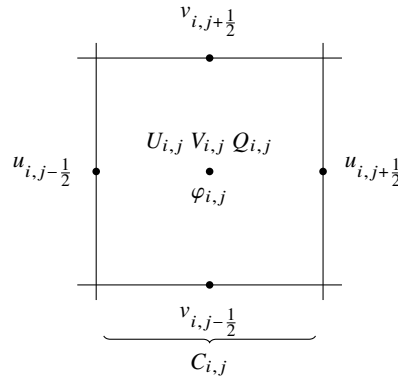


Figure 6.2.: Illustration of the grid used for the discretisation of (6.2).

Comparable to section 6.1, the numerical solution of the coupled moment system for the two-dimensional flow problem is computed with the steps presented in Algorithm 2.

Algorithm 2 Operator splitting algorithm for solving the coupled moment system (6.2)

1. $\frac{1}{2}\Delta t$ step on the Navier-Stokes equation. Calculate $u_x(\mathbf{x}, t), u_z(\mathbf{x}, t), w_x(\mathbf{x}, t), w_z(\mathbf{x}, t)$.
 2. $\frac{1}{2}\Delta t$ step on $\partial_t Q(\mathbf{x}, t) = \varphi(Q(\mathbf{x}, t))$.
 3. $\frac{1}{2}\Delta t$ step on $w_t(\mathbf{x}, t) = -\frac{\delta}{Re}\rho$.
 4. Δt step on $\partial_t Q(\mathbf{x}, t) + A\partial_x Q(\mathbf{x}, t) + B\partial_y Q(\mathbf{x}, t) = 0$.
 5. $\frac{1}{2}\Delta t$ step on the Navier Stokes equation. Calculate $u_x(\mathbf{x}, t), u_z(\mathbf{x}, t), w_x(\mathbf{x}, t), w_z(\mathbf{x}, t)$.
 6. $\frac{1}{2}\Delta t$ step on $\partial_t Q(\mathbf{x}, t) = \varphi(Q(\mathbf{x}, t))$.
 7. $\frac{1}{2}\Delta t$ step on $w_t(\mathbf{x}, t) = -\frac{\delta}{Re}\rho$.
-

In each time step, the Navier-Stokes equation is solved with the projection method presented

in section 2.5. The solution is used to calculate the discrete derivatives

$$\begin{aligned}
 u_x(x_i, y_j, t^n) &= \frac{u_{i+\frac{1}{2},j}^n - u_{i-\frac{1}{2},j}^n}{\Delta x}, \quad i = 1, \dots, m, \quad j = 1, \dots, m, \\
 u_z(x_i, y_j, t^n) &= \frac{u_{i,j+\frac{1}{2}}^n - u_{i,j-\frac{1}{2}}^n}{\Delta y}, \quad i = 1, \dots, m, \quad j = 1, \dots, m, \\
 w_x(x_i, y_j, t^n) &= \frac{w_{i+\frac{1}{2},j}^n - w_{i-\frac{1}{2},j}^n}{\Delta x}, \quad i = 1, \dots, m, \quad j = 1, \dots, m, \\
 w_z(x_i, y_j, t^n) &= \frac{w_{i,j+\frac{1}{2}}^n - w_{i,j-\frac{1}{2}}^n}{\Delta y}, \quad i = 1, \dots, m, \quad j = 1, \dots, m.
 \end{aligned}$$

The system of ordinary differential equations resulting from the source term of the moment system and the Navier-Stokes equation are solved with a solver for ordinary differential equations. The solution of the homogeneous system of moment equations is calculated with the high-resolution Wave Propagation Algorithm by LeVeque described in subsection 2.3.3.

Again, the calculation of the numerical solution of the lower-dimensional coupled moment system (6.2) is simpler than the discretisation of the detailed model described in section 4.2.

6.3 Comparison with the Detailed Numerical Method

In this section, we show that the macroscopic model based on a hyperbolic hierarchy of moment equations allows to approximate the high-dimensional scalar Smoluchowski equation with a lower dimensional system of partial differential equations.

In Remark 5.2 and Remark 5.10, we have already noticed that the homogeneous systems of moment equations for a shear flow (5.4) and a two-dimensional flow (5.13) result from the subproblems (4.2) and (4.7) of the detailed models. Also the source terms (5.6) and (5.15) in the one- and two-space dimensional moment systems result from the subproblems (4.1) and (4.6) of the detailed models. In the following, we want to analyse this relation precisely.

The comparison of the source terms in (5.6) and (5.15) with the spectral methods from subsection 4.1.1 and subsection 4.2.1 leads to the following result.

6.1 Proposition. *The source terms in the moment systems (5.6) and (5.15) are equivalent with the spectral method for the subproblems (4.1) and (4.6).*

Next, we investigate how well the systems of homogeneous conservation laws (5.4) and (5.13) approximate the subproblems (4.2) and (4.7) of the detailed model. While the detailed models are time-dependant partial differential equations in space and orientation, the systems of moment equations depend only on the spatial variables and time.

6.2 Example. We use a generalised Riemann Problem to analyse the relation of the detailed model and the homogeneous system of moment equations for an externally imposed shear flow. In this case, subproblem (4.7) has the form

$$\partial_t f(x, t, \theta) + \partial_x(-\cos \theta \sin \theta f) = 0. \quad (6.3)$$

We compute the numerical solution of (6.3) for a Riemann Problem, in which we use $w_x/D_r = 100$ for $x < 0$ and $w_x/D_r = 200$ for $x > 0$. As initial data for f , we use the steady state solution of subproblem (4.6) with $\rho(x, 0) = \int_0^{2\pi} f(x, 0, \theta) \equiv 1$. Note that for fixed values of θ the initial values of f are piecewise constant. The numerical solution of f at time $t = 5$ is used to compute the moment ρ which can be compared with the solution of the moment system

$$\partial_t Q(x, t) + A \partial_x Q(x, t) = 0. \quad (6.4)$$

Here $Q = (\rho, C_1, S_1, \dots, C_N, S_N)$ is the vector of moments and A has the form described in (5.7). Again, the initial values of Q are obtained from the steady state solution of (4.6) using a scaling of the form $\rho = 2\pi f_0$, $C_i = \frac{\pi}{2} c_i$, $S_i = \frac{\pi}{2} s_i$, $i = 1, \dots, N$ and are piecewise constant. We repeat the comparison for a Riemann problem, in which we use $w_x/D_r = 10$ for the left state and $w_x/D_r = 20$ for the right state.

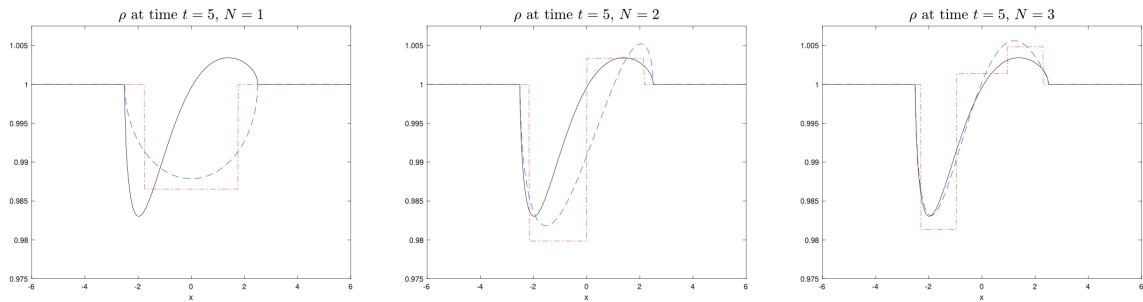


Figure 6.3.: Solution of the Riemann problem defined in Example 6.2 using a highly resolved solution of subproblem (4.2) (blue curve) and the moment system for different N (red curve). The black curve is a highly resolved reference solution. The initial values are steady state solutions of the Smoluchowski equation with left state $w_x/D_r = 10$ and right state $w_x/D_r = 20$.

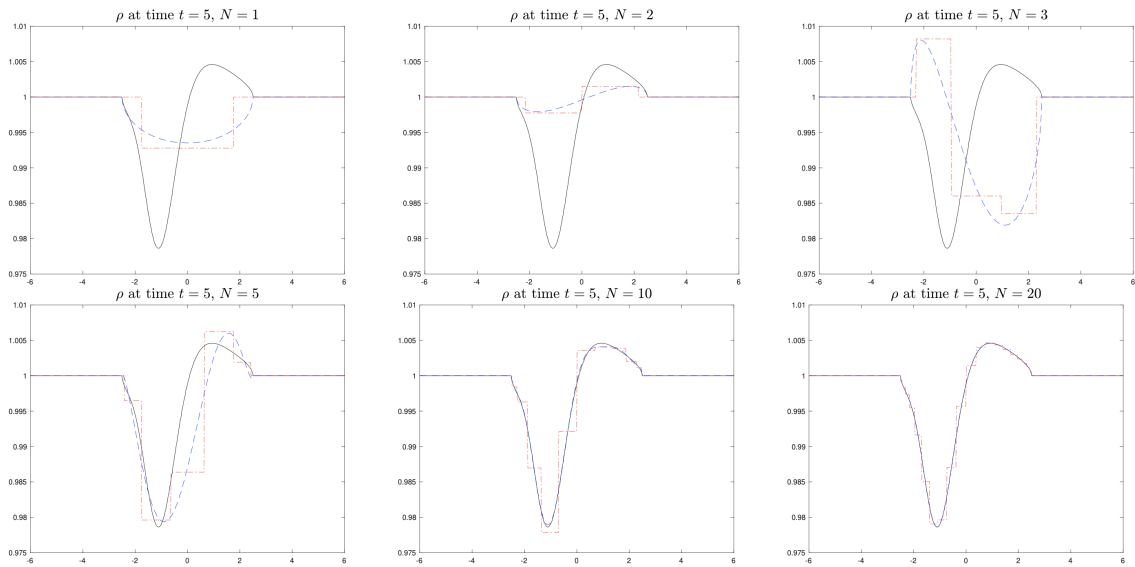


Figure 6.4.: Solution of the Riemann problem defined in Example 6.2 using a highly resolved solution of subproblem (4.2) (blue curve) and the moment system for different N (red curve). The black curve is a highly resolved reference solution. The initial values are steady state solutions of the Smoluchowski equation with left state $w_x/D_r = 100$ and right state $w_x/D_r = 200$.

In Figure 6.4 and Figure 6.3, the results of the comparison described in Example 6.2 are presented.

The black solid curve is a highly resolved reference solution computed from the detailed model (6.3) with accurate initial data. The analysis in section 4.1 has shown that a precise approximation of the steady state solution structure of (4.1) requires a sufficiently large N in the spectral method. The initial values for the reference solution are computed with $N = 50$. This initial data is used to compute the cell average values of f of subproblem (6.3) at time $t = 5$ with the high-resolution Wave Propagation Algorithm from subsection 4.1.3 on a numerical grid with 1000 grid cells in $x \in [-10, 10]$ and 1000 grid cells in $\theta \in [0, 2\pi]$. The discrete solution of $f(x, \theta, t)$ is integrated over θ for the comparison with the moment $\rho(x, t)$ in (6.4).

The red dashed-dotted curves in Figure 6.4 and Figure 6.3 show the first component of the vector Q of the exact solution of the Riemann problem for the homogeneous one-dimensional hyperbolic system (6.4) for different values of N .

The comparison of the solution of the Riemann problem for the moment system in red with the reference solution in black in both figures indicates that the accuracy of the moment

system increases with the number of moments that is used. While the moment system using 3 moments equations in Figure 6.4 results in a very rough approximation of the reference solution, the approximation of the moment system using 41 moments describes the solution structure of subproblem (6.3) very well. Comparable to the results in subsection 4.1.1, Figure 6.3 illustrates that in case of a diffusion dominated regime of small values of w_x/D_r , a smaller number of moment equations produces accurate approximations of the reference solution than in a drift dominated regime of large w_x/D_r . Thus, the test problem in Example 6.2 shows the importance of the choice of N . Once N is large enough, the solution of the system of moment equations describes an accurate approximation of the reference solution.

Moreover, we can see blue dashed curves in Figure 6.4 and Figure 6.3 which once again show results of the highly resolved method for (6.3) but use the same number of degrees of freedom to construct the initial values in f as used in (6.4). Comparing this solution with the red dashed-dotted curve, we observe that this solution of the Riemann problem for the detailed model is smoother than the solution of the Riemann problem for the moment system but not more accurate. The number of modes that can be used to describe the initial data in f depends on the number of degrees of freedom used in the spectral method to solve subproblem (4.1). This comparison reveals that a highly resolved mesh in θ in the detailed model is useless if the initial values are not accurate enough.

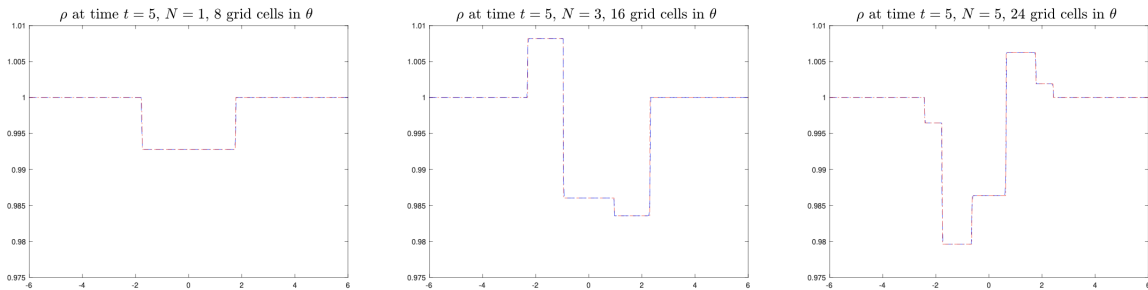


Figure 6.5.: Solution of the Riemann problem using coarse grids in θ for the solution of subproblem (4.2) (blue dashed curve) and the exact solution of the Riemann problem for the homogeneous moment system (red dashed-dotted curve) for odd N .

As a consequence of this finding, we want to compare the solution of the Riemann problem for the hyperbolic system of moment equations with the detailed model using a coarse grid in θ . In Figure 6.4, we once more consider the Riemann problem from Example 6.2, but this time the blue dashed curve shows the solution of the detailed model using the high-resolution Wave Propagation Algorithm on a coarse grid in θ with $8\lceil \frac{N}{2} \rceil$ grid cells for odd values of N . In x , the interval $[-10, 10]$ is still discretised on a highly resolved mesh with 1000 grid cells.

The initial values in f for the detailed method use the same number of ansatz functions as moments are used in the moment system.

The red dashed-dotted curve is again the exact solution of the Riemann problem for the system of moment equations for different values of N .

We observe that the solution of the Riemann problem for the hyperbolic system of moment equations can exactly be approximated with the detailed model using a coarse grid in θ .

Illustration of coarse grid approximation for $N = 5$

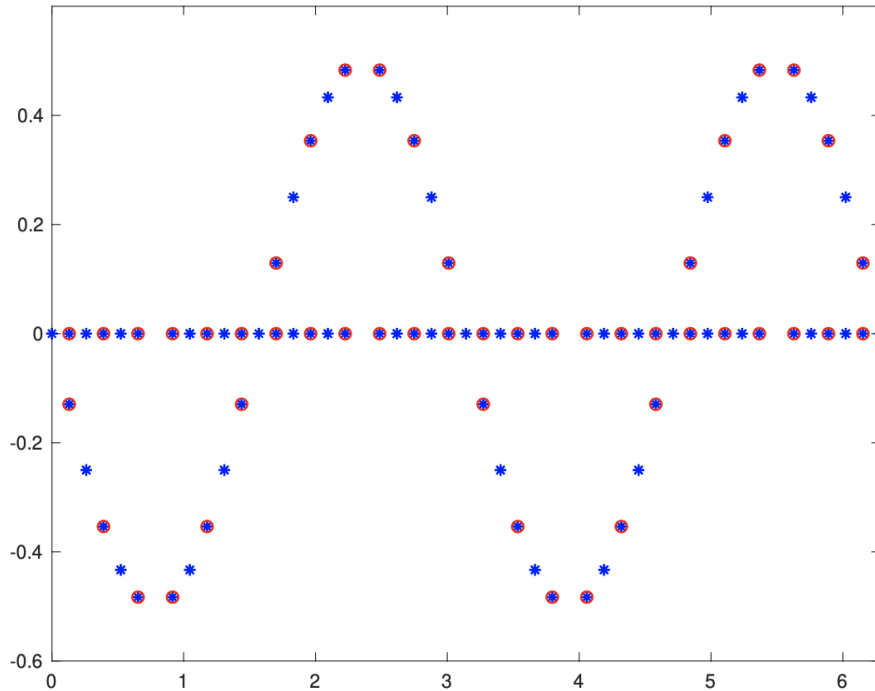


Figure 6.6.: Illustration of the relation between the solution of the Riemann problem for the hyperbolic system and a coarse grid approximation of the transport equation (4.2).

We study the case $N = 5$ in detail. In this case, the hyperbolic moment system uses 11 moment equations, i.e. $A \in \mathbb{R}^{11 \times 11}$. The analysis of the eigenvalues of A , described in remark 5.3, and of the eigenvectors reveals that ρ is a Riemann invariant of 5 waves. Hence, there are 6 jump discontinuities in the last plot of Figure 6.5. Each eigenvalue of A which is not equal to zero is attained four times inside the intervall $[0, 2\pi)$ as a function value of $-\sin \theta \cos \theta$, which is the advection speed of the detailed model (6.3). In Figure 6.6 we plot as stars the values $\theta \in [0, 2\pi]$ where the function $-\sin \theta \cos \theta$ is equal to an eigenvalue; we also plot the corresponding function values. Moreover, we plot the 24 grid cell centres and the corresponding advection speeds that are used on the coarse grid as red circles. Every advection speed is discretised four times. It turns out that a grid with $8 \lceil \frac{N}{2} \rceil$ equidistant grid cells uses every second wave speed as advection speed for the discretisation of (6.3). These

are exactly the waves needed to resolve the structure in ρ .

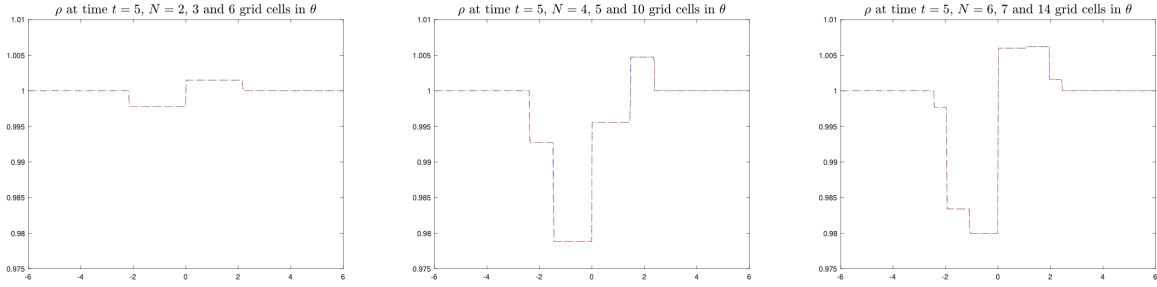


Figure 6.7.: Solution of the Riemann problem using coarse grids in θ for the solution of the subproblem (4.2) (blue dashed curve) and the exact solution of the Riemann problem for the homogeneous moment system (red dashed-dotted curve) for even N .

For even values of N , there is no single equidistant coarse grid for which the approximation of the detailed model agrees with the solution of the Riemann problem for the moment system. Instead, we have to take the average of two coarse grid approximations of the transport equations using $N + 1$ and $2(N + 1)$ grid cells in order to exactly approximate the solution structure of ρ . This is visualised for $N = 2$, $N = 4$ and $N = 6$ in Figure 6.7. We summarise our analysis in the following proposition.

6.3 Proposition. *The homogeneous hyperbolic system $\partial_t Q + A \partial_x Q = 0$, with A defined as in (5.7), provides an approximation of the transport equation (6.3).*

6.4 Example. *We repeat the analysis for the spatial transport in z of subproblem (4.7)*

$$\partial_t f + \partial_z \left(\left(1 + \sin^2 \theta \right) f \right) = 0. \quad (6.5)$$

As in Example 6.2, we use the steady state solution of subproblem (4.6) with $\rho(x, 0) = \int_0^{2\pi} f(x, 0, \theta) \equiv 1$ as initial data for f . For $x < 0$ we use $w_x/D_r = 100$ and for $x > 0$ we use $w_x/D_r = 200$. We discretise the solution of (6.5) in the same way as in Example 6.2 and compare the solution of ρ with the solutions of the homogeneous system of moment equations

$$\partial_t Q(x, t) + B \partial_y Q(x, t) = 0, \quad (6.6)$$

where B has the form described in (5.17). In Figure 6.8, we compare again a highly resolved reference solution of (4.7) using $N = 50$ in the spectral method (black curve) with the solution of the Riemann problem for the moment system (6.6) for different values of N (red curve).

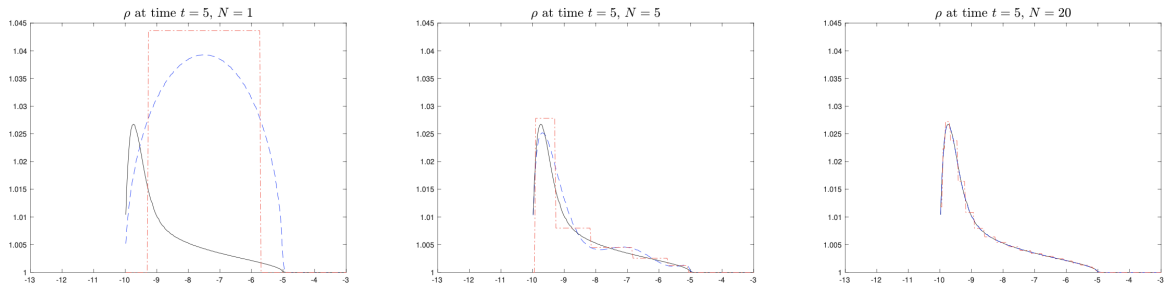


Figure 6.8.: Solution of the Riemann problem defined in Example 6.4 using a highly resolved solution of subproblem (4.7) (blue curve) and the moment system for different N (red curve). The black curve is a highly resolved reference solution.

As in Example 6.2, the solution of the moment system (6.6) compares well with the reference solution if N is large enough.

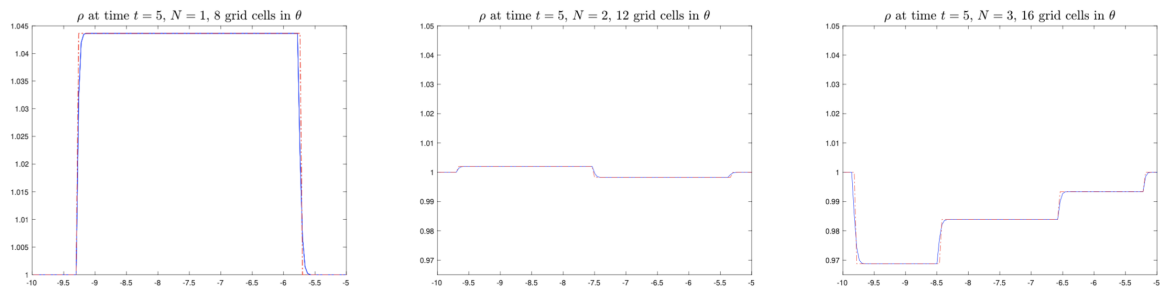


Figure 6.9.: Solution of the Riemann problem using coarse grids in θ for the solution of the subproblem (4.7) (blue dashed curve) and the exact solution of the Riemann problem for the homogeneous moment system (red dashed-dotted curve) for different N .

Again, the correct solution of the Riemann problem for the homogeneous system (6.6) can well be approximated with the detailed method (6.5) using a coarse grid in θ . Now, the blue dashed curve in Figure 6.9 visualises the solution of the detailed model using a finite volume method on an equidistant grid in θ with $12 + 8 \cdot (\frac{N}{2} - 1)$ grid cells if N is even and with $8 \lceil \frac{N}{2} \rceil$ grid cells if N is odd.

We conjecture that the homogeneous hyperbolic system (5.15) for the two-dimensional flow problem provides an approximation of subproblem (4.7).

Note that the solution of the one-dimensional Riemann problem is a crucial building block in finite volume methods for higher dimensional problems. Thus, the considerations of this subsection are of importance also in more complex flow situations.

6.4 Numerical Simulations

So far, the analysis has shown that the hyperbolic system of moment equations can be interpreted as a lower-dimensional approximation of the high-dimensional Smoluchowski equation and consequently simplifies the numerical approximation of sedimentation in suspensions of rod-like particles. In this section, we investigate the ability of the method to accurately approximate test cases motivated by complex flow structures as described in section 1.1.

6.5 Example. *First, we analyse the cluster formation for an initially well stirred suspension of rod-like particles with the coupled moment system for shear flow (6.1). Let*

$$\rho(x, 0) = 1 + 10^{-3}\eta(x),$$

$$C_i(x, 0) = S_i(x, 0) = w(x, 0) = 0, \quad i = 1, \dots, N,$$

where $\eta(x)$ takes random values between $-\frac{1}{2}$ and $\frac{1}{2}$. We use the parameters $D_r = 0.01$ and $\delta = 1$ and periodic boundary conditions. The solution of ρ is computed on an interval $[0, 100]$ at time $t = 50$ using different values of N . For each simulation, we use the same random initial perturbation of ρ .

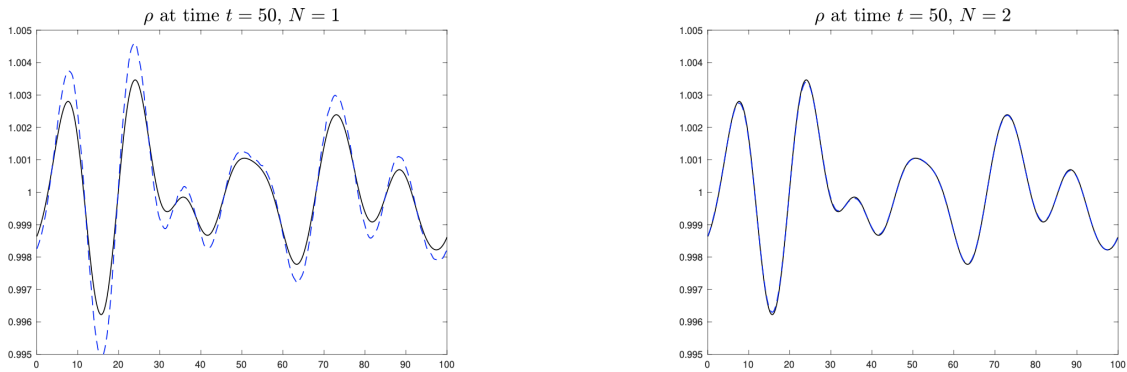


Figure 6.10.: Approximation of the coupled problem for shear flow as described in Example 6.5. We show the density at time $t = 50$ for $N = 1$ and $N = 2$ as dashed blue line. The black solid line is a reference solution computed using $N = 50$.

In Figure 6.10, we compare the numerical solution of ρ of the coupled model (6.1) at time $t = 50$ calculated with the initial data presented in Example 6.5 for different values of N (blue dashed line) with a reference solution computed using $N = 50$ (black solid line). For the discretisation in x , 1000 grid cells on the interval $[0, 100]$ are used. The moment system using $N = 1$ moment equations already approximates the formation of clusters and the cluster

width quite well. However, the approximation of the amplitude is improvable. For $N = 2$, the numerical solution compares very well with the reference solution.

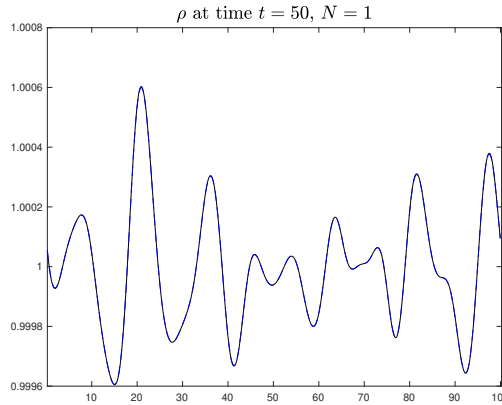


Figure 6.11.: Approximation of the coupled problem for shear flow as described in Example 6.5 but with $D_r = 1$. We show the density at time $t = 50$ for $N = 1$ as dashed blue line. The black solid line is a reference solution computed using $N = 50$.

In Figure 6.11, we consider the same initial data as in Example 6.5 but use $D_r = 1$. In this case, the numerical solution computed with $N = 1$ moment equations already compares very well with the reference solution. Hence, in a diffusion dominated regime less moments are needed for an accurate approximation of the reference solution than in a drift dominated regime.

6.6 Example. We study the numerical solution of the coupled moment system for initial values that are far away from an equilibrium state. Therefore, we consider the coupled moment system for shear flow (6.1) with initial data on the interval $[0, 100]$ of the form

$$\rho(x, 0) = \exp(-(x - 50)^2)$$

$$C_i(x, 0) = S_i(x, 0) = w(x, 0) = 0, \quad i = 1, \dots, N$$

and periodic boundary conditions. We use the parameters $D_r = 0.01$ and $\delta = 1$. The solution of ρ is computed at time $t = 30$ using different values of N .

In Figure 6.13, we plot the density ρ calculated with the initial data presented in Example 6.6 at time $t = 30$ for different values of N as a blue dashed line. The reference solution using $N = 50$ is visualised as a black solid line. The numerical simulations show that a certain number of moment equations is needed in order to compute accurate approximations with the system of moment equations. The comparison of the reference solution with the numerical

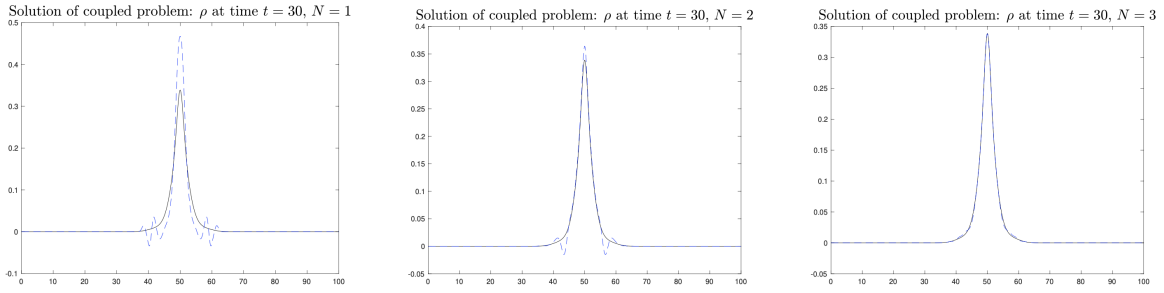


Figure 6.12.: Approximation of the coupled problem for shear flow as described in Example 6.6. We show the density at time $t = 30$ for different values of N as blue dashed line. The black solid line is a reference solution computed using $N = 50$. (Note different y-axis.)

approximation obtained with $N = 1$ moment equations reveals decisive differences. The negative values of the solution of the moment system are unphysical. For $N = 2$, the accuracy has improved, but we still have unphysical negative values of the density. By increasing the number of moments that is used to approximate the physical problem, we can ensure physical admissibility. For $N = 3$, the solution is of comparable accuracy as the reference solution. In Table 6.1 and Table 6.2, we present a convergence study for the problem in Example 6.6

	N=1		N=2		N=3		N=4	
grid	L_∞ -Error	EOC						
128	$1,543 \cdot 10^{-1}$		$1,14 \cdot 10^{-1}$		$1,479 \cdot 10^{-1}$		$1,359 \cdot 10^{-1}$	
256	$5,51 \cdot 10^{-2}$	1,49	$4,738 \cdot 10^{-2}$	1,57	$4,666 \cdot 10^{-2}$	1,66	$4,545 \cdot 10^{-2}$	1,58
512	$1,99 \cdot 10^{-2}$	1,47	$1,293 \cdot 10^{-2}$	1,87	$1,286 \cdot 10^{-2}$	1,86	$1,262 \cdot 10^{-2}$	1,85
1024	$6,791 \cdot 10^{-3}$	1,55	$4,07 \cdot 10^{-3}$	1,67	$3,881 \cdot 10^{-3}$	1,73	$3,824 \cdot 10^{-3}$	1,72

Table 6.1.: Accuracy study for the problem in Example 6.6 using $N = 1, \dots, 4$ moment equations. The reference solution uses the same number of moment equations as the coarse solution. The models are discretised with the methods from section 6.1.

for different values of N . As there is no analytical solution for the coupled problem (6.1), we use a highly resolved numerical solution of (6.1) calculated on a very fine grid with 4096 grid cells as a reference solution. We compare the highly resolved solution of ρ with the numerical solution of ρ on coarse grids for different values of N . As the grids are chosen in the way that all grid points on coarser grids are also grid points on the fine grid, we can compare the numerical solutions of ρ on coincident grid points. The highly resolved solution and the coarse solution use the same number of moment equations. We show the L_∞ -error and the experimental order of convergence (EOC), computed by comparing the error on two

different grids

$$EOC = \frac{\log \left(\frac{\|\rho_n - \rho_n^{ex}\|_\infty}{\|\rho_{2n} - \rho_{2n}^{ex}\|_\infty} \right)}{\log(2)}.$$

ρ_n denotes the numerical solution computed on a coarse grid with n grid cells in x at time $t = 30$. ρ_n^{ex} is the reference solution which is computed on a fine grid in x at time $t = 30$ and subsequently coarsened to n grid cells. In all computations for Table 6.1 and Table 6.2, we discretised problem (6.1) with the methods of second order presented in section 6.1.

	N=5		N=10		N=15		N=20	
grid	L_∞ -Error	EOC						
128	$1,369 \cdot 10^{-1}$		$1,379 \cdot 10^{-1}$		$1,38 \cdot 10^{-1}$		$1,379 \cdot 10^{-1}$	
256	$4,556 \cdot 10^{-2}$	1,59	$4,538 \cdot 10^{-2}$	1,6	$4,535 \cdot 10^{-2}$	1,61	$4,534 \cdot 10^{-2}$	1,61
512	$1,261 \cdot 10^{-2}$	1,85	$1,251 \cdot 10^{-2}$	1,86	$1,249 \cdot 10^{-2}$	1,86	$1,248 \cdot 10^{-2}$	1,86
1024	$3,812 \cdot 10^{-3}$	1,73	$3,768 \cdot 10^{-3}$	1,73	$3,758 \cdot 10^{-3}$	1,73	$3,754 \cdot 10^{-3}$	1,73

Table 6.2.: Accuracy study for the problem in Example 6.6 using $N = 5$, $N = 10$, $N = 15$ and $N = 20$ moment equations. The reference solution uses the same number of moment equations as the coarse solution. The models are discretised with the methods from section 6.1.

In Table 6.1 and Table 6.2, we can see that we do not get the full second order. The convergence rate of 1,55 for $N = 1$ increases to 1.73 for $N \geq 3$.

	N=1		N=2		N=3		N=4	
grid	L_∞ -Error	EOC						
128	$1,989 \cdot 10^{-1}$		$1,473 \cdot 10^{-1}$		$1,473 \cdot 10^{-1}$		$1,357 \cdot 10^{-1}$	
256	$1,109 \cdot 10^{-1}$	0,84	$5,341 \cdot 10^{-2}$	1,46	$4,861 \cdot 10^{-2}$	1,6	$4,564 \cdot 10^{-2}$	1,57
512	$7,638 \cdot 10^{-2}$	0,54	$1,874 \cdot 10^{-2}$	1,51	$1,508 \cdot 10^{-2}$	1,69	$1,273 \cdot 10^{-2}$	1,84
1024	$6,338 \cdot 10^{-2}$	0,27	$9,807 \cdot 10^{-3}$	0,95	$6,198 \cdot 10^{-3}$	1,28	$3,897 \cdot 10^{-3}$	1,71

Table 6.3.: Accuracy study for the problem in Example 6.6 using $N = 1, \dots, 4$. The reference solution uses $N = 20$ moment equations. The models are discretised with the methods from section 6.1.

Next, we calculate the reference solution on a highly resolved grid with 4096 grid cells and $N = 20$ moment equations. We compare this reference solution with the numerical solution on a coarse grid using $N = \{1, 2, 3, 4, 5, 6, 10, 15\}$ moments in Table 6.3 and Table 6.4. In Table 6.3, we observe that the numerical solutions calculated with $N = 1$ or $N = 2$ moment equations do not converge to the reference solution. We have seen in Figure 6.13 that in this case the numerical solution leads to unphysical solutions. For $N = 3$, the solution structure of the numerical solution compares well with the reference solution and the numerical solution

grid	N=5		N=6		N=10		N=15	
	L_∞ -Error	EOC						
128	$1,369 \cdot 10^{-1}$		$1,378 \cdot 10^{-1}$		$1,379 \cdot 10^{-1}$		$1,38 \cdot 10^{-1}$	
256	$4,538 \cdot 10^{-2}$	1,59	$4,547 \cdot 10^{-2}$	1,6	$4,539 \cdot 10^{-2}$	1,6	$4,535 \cdot 10^{-2}$	1,61
512	$1,243 \cdot 10^{-2}$	1,87	$1,256 \cdot 10^{-2}$	1,86	$1,252 \cdot 10^{-2}$	1,86	$1,249 \cdot 10^{-2}$	1,86
1024	$3,639 \cdot 10^{-3}$	1,77	$3,782 \cdot 10^{-3}$	1,73	$3,772 \cdot 10^{-3}$	1,73	$3,759 \cdot 10^{-3}$	1,73

Table 6.4.: Accuracy study for the problem in Example 6.6 using $N = 5$, $N = 10$, $N = 15$ and $N = 20$. The reference solution uses $N = 20$ moment equations. The models are discretised with the methods from section 6.1.

starts to converge. Table 6.4 shows that numerical solutions computed with more than $N = 3$ moment equations converge to the reference solution with the expected order of convergence of 1.73. This convergence study demonstrates that a certain number of moments is needed so that the solution of the moment system converges to the reference solution.

6.7 Example. *In a final example, we extend the test problem in Example 6.6 to the two-dimensional case. The test case was motivated by experimental observations for the sedimentation of clouds of rod-like particles as described in [70]. Clouds of particles become unstable and break into smaller droplets of particles.*

We consider the coupled moment system (6.2) and the same initial data as in Example 6.6 but now constantly extended in the z -direction. Now, both velocity components (u, w) are initially set to zero. The non-dimensional parameters are set to $D_r = 0.01$, $\delta = 1$, $Re = 1$ and $\gamma = 0$. We use periodic boundary conditions in the x - and z -direction on a domain of size $[0, 100] \times [0, 100]$. We compute solutions for different values of N on a grid with 512×512 grid cells.

In Figure 6.13, we plot the temporal evolution of the density ρ which was computed with the coupled system of moment equations (6.2) for the initial data in Example 6.7 and different values of N . For all values of N , the plots show that a column with higher particle density does not remain constant in the z -direction and gets unstable in a two-dimensional flow. While the numerical solution of the coupled system (6.2) for $N = 1$ predicts an instability in density at time $t = 16$, this instability of the solution structure is seen at an earlier time for larger N , compare with Figure 6.13. In addition, the moment system for $N = 1$ produces unphysical, negative values in density at time $t = 20$. If we increase the number of moment equations to $N = 4$ for the calculation of the numerical solution of the coupled system (6.2), the temporal evolution of the density compares well with the solution observed for $N = 10$ and unphysical solutions can be avoided.

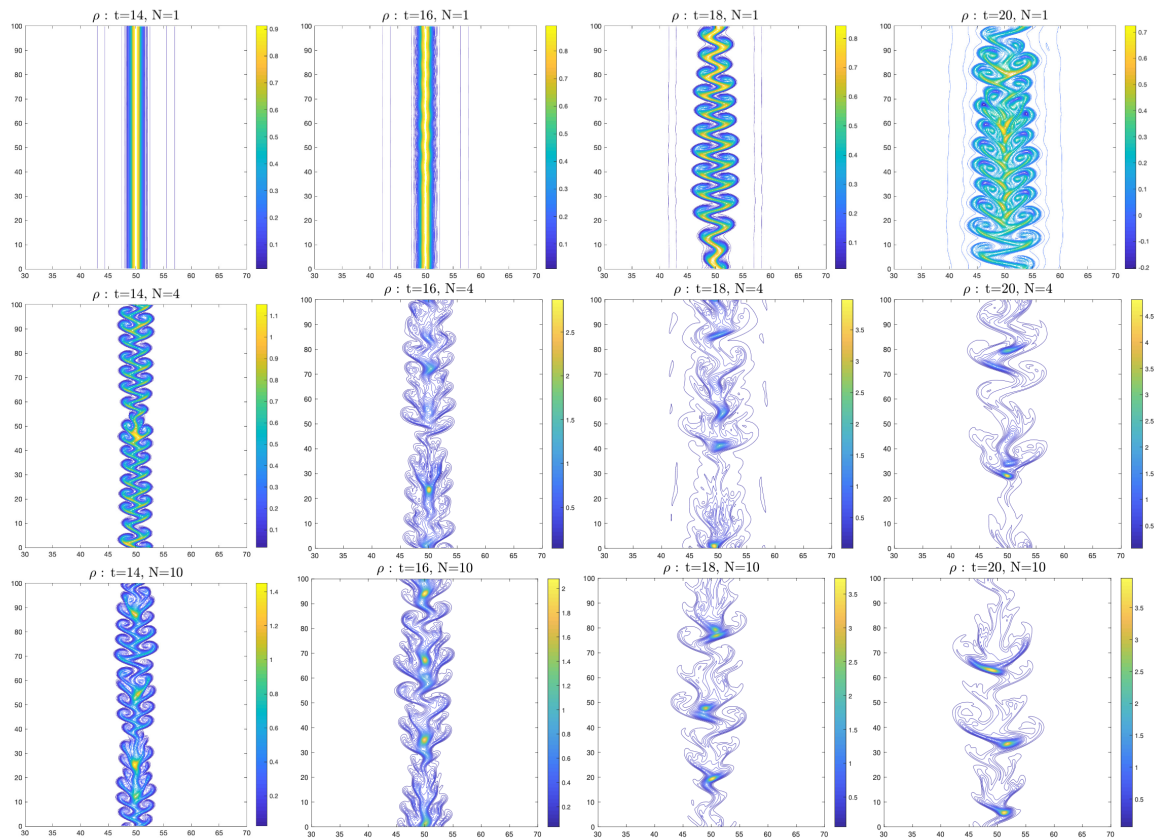


Figure 6.13.: Numerical solutions of the two-dimensional coupled problem described in Example 6.7 for $N = 1$ (top), $N = 4$ (middle) and $N = 10$ (bottom).

The numerical simulations in this chapter have shown that complex flow structures observed during sedimentation in suspensions of rod-like particles can well be approximated using the lower dimensional hyperbolic system of moment equations if the number of moments equations is high enough. So far, independently of the flow structure, the same number of moment equations was used throughout the domain of interest.

Interface Coupling of Moment Systems with Different Resolution

In this chapter, we use the hierarchy of moment equations to derive a macroscopic model for sedimentation in suspensions of rod-like particles which adaptively adjusts the level of detail by coupling hyperbolic moment systems with different numbers of moment equations.

As described in section 1.1, the interplay of the particle orientation and the flow field generated by the sedimenting rod leads to a destruction of the spatially homogeneous distribution of the particles and structural instabilities like cluster formations. While the rods are nearly isotropic in regions with low particle densities, they are strongly oriented in the direction of gravity in regions of particle packages.

Numerical simulations in the previous chapters have shown that different levels of detail are required to accurately approximate the spatially varying behaviour of the particles. The approximation of the steady state solution of the Smoluchowski equation with an externally imposed velocity gradient in Example 4.1 as well as the approximation of the coupled problem with initial data which is far away from equilibrium state in Example 6.6 demonstrated that a high number of moment equations is needed to resolve the complex flow structure in spatial regions of the domain with clusters, while few moment equations are sufficient in spatial regions of the domain with low particle densities. Thus, for deriving an accurate and efficient approximation of the concentration instabilities in sedimentations of suspensions of rod-like particles, the number of moment equations used in the hyperbolic moment system should be adapted to locally varying flow features and accuracy requirements.

The results presented in Figure 4.1 suggest the magnitude of the highest moments as a possible selection criteria for choosing the right number of moment equations.

The chapter is structured as follows: In section 7.1, we solve generalised Riemann problems for moment systems with different levels of resolution for shear flow. Subsequently in

section 7.2, we develop a conservative finite volume method for solving the one-space dimensional hyperbolic moment system using different numbers of moment equations in different spatial areas of the domain. Finally, we analyse numerical simulations of the coupled shear flow problem in which the number of moment equations is adjusted adaptively.

7.1 Riemann Problems for Moment Systems with Different Resolution for Shear Flow

Our goal is to derive models for sedimentation in suspension of rod-like particles that adaptively adjust the level of detail. The idea is to couple moment systems consisting of different numbers of moment equations in different spatial regions of the domain. For solving these moment systems with different resolution with the high-resolution Wave Propagation Algorithm, generalised Riemann problems of the following form have to be solved at interfaces between two cells in which moment systems with different numbers of moment equations are used.

$$\begin{aligned}
 \partial_t Q^{2N+1} + A^{2N+1} \partial_x Q^{2N+1} &= 0, & \partial_t Q^{2M+1} + A^{2M+1} \partial_x Q^{2M+1} &= 0, \\
 Q^{2N+1}(x, 0) &= Q_L^{2N+1}, & Q^{2M+1}(x, 0) &= Q_R^{2M+1}, \\
 x < x_0, & & x > x_0, &
 \end{aligned} \tag{7.1}$$

where $A^{2N+1} \in \mathbb{R}^{(2N+1) \times (2N+1)}$ and $A^{2M+1} \in \mathbb{R}^{(2M+1) \times (2M+1)}$ correspond to the coefficient matrix (5.7) of the one dimensional moment system, $M \neq N$ and $Q^{2N+1} \in \mathbb{R}^{2N+1}$, $Q^{2M+1} \in \mathbb{R}^{2M+1}$. In this subsection, we compute the solution of (7.1).

The change of the number of moment equations considered in the coefficient matrices on the left and right hand side of the interface in (7.1) leads to a change of the eigenvalues and eigenvectors. Starting from the left hand side of the interface, we compute the solution $Q^{2N+1} = Q_L^{2N+1} + \sum_{p: \lambda^p < x/t} \mathcal{W}^p$ of the generalised Riemann problem (7.1) with the eigenvectors corresponding to the negative eigenvalues of the coefficient matrix A^{2N+1} and with initial values using $2N + 1$ moment equations. On the right hand of the interface, the solution $Q^{2M+1} = Q_R^{2M+1} - \sum_{p: \lambda^p \geq x/t} \mathcal{W}^p$ can be computed with the eigenvectors corresponding to the positive eigenvalues of A^{2M+1} and with initial values using $2M + 1$ moment equations. Thus, the solution of (7.1) no longer satisfies the equality in (2.9) and is not conservative.

The solution of (7.1) can be written as

$$Q(x, t) = \begin{cases} Q_L^{2N+1}, & x - \lambda_1^{2N+1}t < 0, \\ \tilde{Q}_i, & x \in (\lambda_i^{2N+1}t, \lambda_{i+1}^{2N+1}t), \quad i = 1, \dots, N-1, \\ \tilde{Q}_N, & x \in (\lambda_N^{2N+1}t, \lambda_{M+1}^{2M+1}t), \\ \tilde{Q}_j, & x \in (\lambda_k^{2M+1}t, \lambda_{k+1}^{2M+1}t), \quad j = N+1, \dots, N+M, k = M+1, \dots, 2M \\ Q_R^{2M+1}, & x - \lambda_{2M+1}^{2M+1}t > 0, \end{cases}$$

where λ_i^{2N+1} is an eigenvalue of the coefficient matrix A_{2N+1} and λ_j^{2M+1} an eigenvalue of A_{2M+1} . The eigenvalues can be calculated with the formula (5.3). The initial values are obtained from the steady state solution of (4.1) using $\rho = 2\pi f_0$, $C_i = \frac{\pi}{2}c_i$, $S_i = \frac{\pi}{2}s_i$, $i = 1, \dots, N$ and $C_j = \frac{\pi}{2}c_j$, $S_j = \frac{\pi}{2}s_j$, $j = 1, \dots, M$.

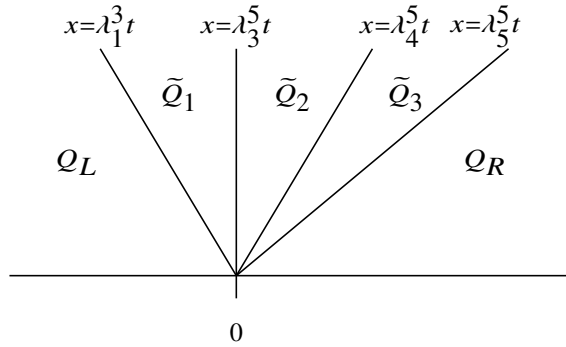


Figure 7.1.: Structure of the solution Q of the generalised Riemann Problem for $N = 1$ and $M = 2$. The value of Q is constant in each wedge of the $x - t$ plane.

In Figure 7.1, the solution of the generalised Riemann Problem (7.1) is visualised in the $x-t$ plane for $N = 1$ and $M = 2$. For $x < 0$ we consider the coefficient matrix A_3 and for $x \geq 0$ the matrix A_5 . While the negative eigenvalue λ_1^3 of A_3 gives the wave speed of the left-going wave $\mathcal{W}^{1,3}$, the positive eigenvalue λ_4^5 of A_5 describes the wave speed of the right-going wave $\mathcal{W}^{4,5}$. Both matrices A_3 and A_5 have the eigenvalue $\lambda_i = 0$. On the left hand side of the interface, three moment equations are used to construct the initial values in f . On the right hand side of the interface, five moment equations are used for the initial values in f .

We want to compare the solution of the generalised Riemann problem (7.1) for moment systems with different resolutions with the solution of the Riemann problem for a moment

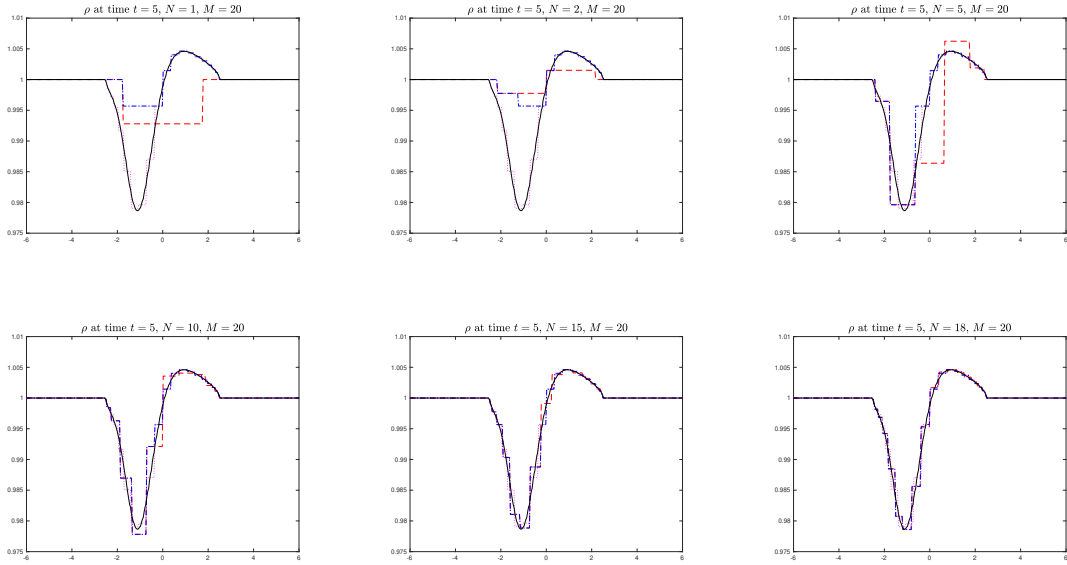


Figure 7.2.: Solution of the generalised Riemann problem described in Example 7.1. The blue dashed dotted curve is the solution for different values of N and $M = 20$. The red dashed curve is a rough solution using different values of $N = M$ throughout the domain. The purple dotted curve is a detailed solution using $N = M = 20$ throughout the domain. The black solid curve is a highly resolved reference solution.

system using $2N + 1 = 2M + 1$ moment equations throughout the domain.

7.1 Example. We consider the generalised Riemann problem (7.1) for different values of N and $M = 20$. The initial values of Q are obtained from the steady state solution of (4.1) using $\rho = 2\pi f_0$, $C_i = \frac{\pi}{2}c_i$, $S_i = \frac{\pi}{2}s_i$, $i = 1, \dots, N$, $C_j = \frac{\pi}{2}c_j$, $S_j = \frac{\pi}{2}s_j$, $j = 1, \dots, 20$ and are piecewise constant for our test problem. For $x < 0$ we used $w_x/D_r = 100$, for $x > 0$ we used $w_x/D_r = 200$. In addition, we consider the Riemann problem (7.1) for $N = M = 20$. As a reference solution we compute the solution of the detailed model (6.3). The initial values for f correspond to steady state solutions of subproblem (4.1). We compute the numerical solution f of (6.3) at time $t = 5$ and use the solution to compute ρ .

In Figure 7.2, we compare the solution of the generalised Riemann problem described in Example 7.1 for moment systems with different levels of detail with the solution of the Riemann problem using $2N + 1 = 2M + 1$. The blue dashed-dotted curve shows the first component ρ of the vector Q of the exact solution of the generalised Riemann problem (7.1) for the homogeneous hyperbolic system at time $t = 5$ for different values of N and $M = 20$. The red dashed curve is a rough solution using different values of $2N + 1 = 2M + 1$ throughout the domain. For example in the first plot in the first line of Figure 7.2, the red dashed curve is computed with $N = M = 1$ modes. The purple dotted curve is the first component ρ of a

detailed solution of the generalised Riemann problem (7.1) using $N = M = 20$. The black solid curve is the solution of the two-dimensional transport problem (6.3), which is solved as described in section 6.3. The function $\rho(x, t = 5)$ from this highly resolved approximation is used as a reference solution.

On the right hand side of the interface, the solution of the generalised Riemann problem described in Example 7.1 for moment systems with different levels of detail (blue dashed dotted curve) is identical to the detailed solution using $N = M = 20$ modes (purple dotted curve). Both solutions have the same waves on right hand side of the interface. For $N = 5$ and $M = 20$, the solution in ρ roughly approximates the reference solution. At lower computational costs, the approximation using $N = 15$ and $M = 20$ compares very well with the solution using $N = M = 20$. The test problem shows that a spatial coupling of moment systems with different resolution allows an accurate approximation of the reference solution once N is large enough.

7.2 Numerical Discretisation of Moment Systems with Different Resolution for Shear Flow

In this section, we derive a conservative high-resolution finite volume method in Wave Propagation form for solving hyperbolic moment systems which couple different numbers of moment equations in different spatial regions of the domain.

Solving coupled moment systems with different resolution with the Wave Propagation Algorithm means solving Riemann problems of the form (7.1) at interfaces between cells in which moment systems with different numbers of moment equations are coupled. As the flux function of the moment system on the left hand side of the interface differs from the flux function on the right hand side, fluctuations defined in the standard form (2.13) and (2.14) would lead to an approximation that is not conservative.

To derive a conservative Wave Propagation Algorithm for solving coupled moment systems with different numbers of moment equations, we define the fluctuations $\mathcal{A}^\pm \Delta Q_{i-\frac{1}{2}}$ as

$$\mathcal{A}^+ \Delta Q_{i-\frac{1}{2}} = f(Q_i) - f(Q_{i-\frac{1}{2}}^*), \quad \mathcal{A}^- \Delta Q_{i-\frac{1}{2}} = f(Q_{i-\frac{1}{2}}^*) - f(Q_{i-1}). \quad (7.2)$$

The fluxes $f(Q_{i-\frac{1}{2}}^*)$ are calculated by solving generalised Riemann problems as described in section 7.1. Recall that the Riemann solution $Q_{i-\frac{1}{2}}^*$ along the interface $x = x_{i-\frac{1}{2}}$ can be

written as

$$Q_{i-\frac{1}{2}}^* = Q_{i-1} + \sum_{p:\lambda^p < 0} \mathcal{W}_{i-1/2}^p \quad (7.3)$$

or alternatively as

$$Q_{i-\frac{1}{2}}^* = Q_i - \sum_{p:\lambda^p > 0} \mathcal{W}_{i-1/2}^p. \quad (7.4)$$

If the same number of moment equations is used in adjacent cells, we have the same flux function on both sides of the interface $x = x_{i-\frac{1}{2}}$. For $2N + 1$ moment equations, formula (7.2) leads to

$$\begin{aligned} \mathcal{A}^+ \Delta Q_{i-\frac{1}{2}} &= A_{2N+1} Q_i^{2N+1} - A_{2N+1} Q_{i-1}^{2N+1} + \sum_{i=1}^{2N+1} (\lambda^{p,2N+1})^+ \mathcal{W}_{i-\frac{1}{2}}^{p,2N+1} \\ &= \sum_{p=1}^{2N+1} (\lambda^{p,2N+1})^+ \mathcal{W}_{i-1/2}^{p,2N+1}, \end{aligned} \quad (7.5)$$

$$\begin{aligned} \mathcal{A}^- \Delta Q_{i-\frac{1}{2}} &= A_{2N+1} Q_{i-1}^{2N+1} + (\lambda^{p,2N+1})^- \mathcal{W}_{i-\frac{1}{2}}^{p,2N+1} - A_{2N+1} Q_{i-1}^{2N+1} \\ &= \sum_{p=1}^{2N+1} (\lambda^{p,2N+1})^- \mathcal{W}_{i-1/2}^{p,2N+1}, \end{aligned} \quad (7.6)$$

where $Q_{i-1}^{2N+1} \in \mathbb{R}^{2N+1}$. Analogously for adjacent cells in which $2M + 1$ moments are used.

At the interface between spatial regions of the domain in which different numbers of moment equations are used we solve Riemann problems between states Q_{i-1}^{2N+1} and Q_i^{2M+1} (or Q_{i-1}^{2M+1} and Q_i^{2N+1}). To construct a conservative method that fulfills the conservation condition (2.15), we assign both states at the interface to the flux function f of the moment system of higher order. We extend the vector $Q_{i-1}^{2N+1} \in \mathbb{R}^{2N+1}$ to a vector of length $2M + 1$ by adding $2M - 2N$ zeros, i.e., we define

$$\tilde{Q}_{i-1}^{2N+1} := \begin{pmatrix} Q_{i-1}^{2N+1} \\ 0 \\ \vdots \\ 0 \end{pmatrix} \in \mathbb{R}^{2M+1}.$$

Moreover, we use (7.4) for both fluctuations $\mathcal{A}^\pm \Delta Q_{i-\frac{1}{2}}$. Assuming that $2M + 1 > 2N + 1$, the fluctuations are given as

$$\mathcal{A}^+ \Delta Q_{i-\frac{1}{2}} = f(Q_i) - f(Q_{i-\frac{1}{2}}^*)$$

$$\begin{aligned}
 &= A_{2M+1} Q_i^{2M+1} - A_{2M+1} \tilde{Q}_i^{2M+1} + \sum_{i=1}^{2M+1} \left(\lambda^{p,2M+1} \right)^+ \mathcal{W}_{i-\frac{1}{2}}^{p,2M+1} \\
 &= \sum_{i=1}^{2M+1} \left(\lambda^{p,2M+1} \right)^+ \mathcal{W}_{i-\frac{1}{2}}^{p,2M+1}, \tag{7.7}
 \end{aligned}$$

$$\begin{aligned}
 \mathcal{A}^- \Delta Q_{i-\frac{1}{2}} &= f \left(Q_{i-\frac{1}{2}}^* \right) - f \left(Q_{i-1} \right) \\
 &= A_{2M+1} Q_i^{2M+1} - \sum_{i=1}^{2M+1} \left(\lambda^{p,2M+1} \right)^+ \mathcal{W}_{i-\frac{1}{2}}^{p,2M+1} - A_{2M+1} \tilde{Q}_{i-1}^{2N+1} \\
 &= A_{2M+1} \left(Q_i^{2M+1} - \tilde{Q}_{i-1}^{2N+1} \right) - \sum_{i=1}^{2M+1} \left(\lambda^{p,2M+1} \right)^+ \mathcal{W}_{i-\frac{1}{2}}^{p,2M+1}.
 \end{aligned}$$

We summarise our results in the following theorem.

7.2 Theorem. *Let*

$$\begin{aligned}
 \mathcal{A}^+ \Delta Q_{i-\frac{1}{2}} &= \sum_{i=1}^{2M+1} \left(\lambda^{p,2M+1} \right)^+ \mathcal{W}_{i-\frac{1}{2}}^{p,2M+1}, \\
 \mathcal{A}^- \Delta Q_{i-\frac{1}{2}} &= A_{2M+1} \left(Q_i^{2M+1} - \tilde{Q}_{i-1}^{2N+1} \right) - \sum_{i=1}^{2M+1} \left(\lambda^{p,2M+1} \right)^+ \mathcal{W}_{i-\frac{1}{2}}^{p,2M+1}
 \end{aligned}$$

at interfaces between cells in which moment systems with $2N+1$ and $2M+1$, $M > N$, moment equations are used and

$$\begin{aligned}
 \mathcal{A}^+ \Delta Q_{i-\frac{1}{2}} &= \sum_{p=1}^{2N+1} \left(\lambda^{p,2N+1} \right)^+ \mathcal{W}_{i-1/2}^{p,2N+1}, \\
 \mathcal{A}^- \Delta Q_{i-\frac{1}{2}} &= \sum_{p=1}^{2N+1} \left(\lambda^{p,2N+1} \right)^- \mathcal{W}_{i-1/2}^{p,2N+1}
 \end{aligned}$$

at interfaces between cells in which moment systems with $2N+1 = 2M+1$ moment equations are used. Then the high-resolution Wave Propagation Algorithm

$$Q_i^{n+1} = Q_i - \frac{\Delta t}{\Delta x} \left(\mathcal{A}^+ \Delta Q_{i-1/2} + \mathcal{A}^- \Delta Q_{i+1/2} \right) - \frac{\Delta t}{\Delta x} \left(\tilde{F}_{i+1/2} - \tilde{F}_{i-1/2} \right) \tag{7.8}$$

is a conservative method for solving moment systems with different resolution in different spatial regions of the domain.

Proof. At interfaces between cells in which moment systems with $2N+1$ and $2M+1$, $M > N$

are used, we have

$$\begin{aligned}
 & \mathcal{A}^- \Delta Q_{i-\frac{1}{2}} + \mathcal{A}^+ \Delta Q_{i-\frac{1}{2}} \\
 &= \sum_{i=1}^{2M+1} \left(\lambda^{p,2M+1} \right)^+ \mathcal{W}_{i-\frac{1}{2}}^{p,2M+1} + A_{2M+1} \left(Q_i^{2M+1} - \tilde{Q}_{i-1}^{2N+1} \right) - \sum_{i=1}^{2M+1} \left(\lambda^{p,2M+1} \right)^+ \mathcal{W}_{i-\frac{1}{2}}^{p,2M+1} \\
 &= A_{2M+1} Q_i^{2M+1} - A_{2M+1} \tilde{Q}_{i-1}^{2N+1} \\
 &= f(Q_i) - f(Q_{i-1}).
 \end{aligned}$$

At interfaces between cells in which moment systems with $2N+1 = 2M+1$ moment equations are used, the fluctuations (7.5) and (7.6) are defined in the standard form and obviously fulfill the conservation condition (2.15).

As the second order correction terms are defined in flux difference form, (7.8) leads to a conservative update. \square

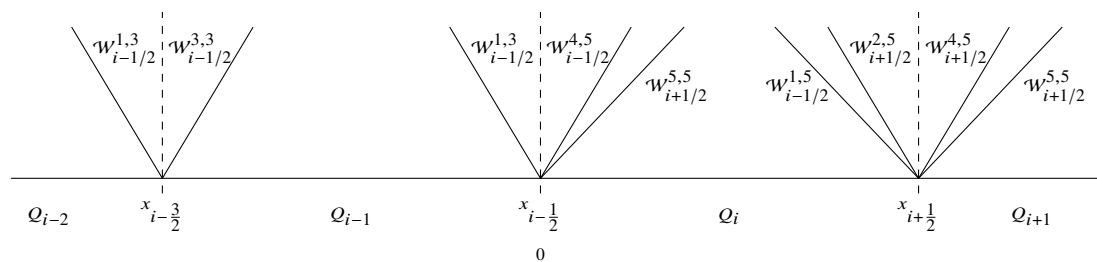


Figure 7.3.: Schematic diagram of the Godunov's method for solving the generalised Riemann Problem (7.1) for $N = 1$ and $M = 2$. The Riemann problem is solved at each cell interface.

Figure 7.3 gives a schematic diagram of the Godunov's method for solving the generalised Riemann problem (7.1) for $N = 1$ and $M = 2$. At the interface $x_{i-\frac{3}{2}}$, the Riemann problem between the states Q_{i-2}^3 and Q_{i-1}^3 has to be solved. The flux function on the left and on the right hand side of the interface is given as $A_3 Q^3$. Analogously, the flux function at the interface $x_{i+\frac{1}{2}}$ is given as $A_5 Q^5$. At the interface $x_{i-\frac{1}{2}}$, three moment equations are used on the left and five moment equations on the right hand side of the interface. To get a conservative method, we choose the coefficient matrix A_5 for the flux function and solve the Riemann problem for the coefficient matrix A_5 to determine the fluctuations (7.7).

In the following example, we use the presented finite volume method to solve a moment system coupling different numbers of moment equations in different spatial regions of the domain. Based on the results in Figure 4.1, we use the magnitude of the highest moment equations to choose the right number of moment equations.

7.3 Example. We consider the coupled moment system for shear flow (6.1) with initial data on the interval $[0, 100]$ of the form

$$\begin{aligned}\rho(x, 0) &= \exp(-10(x - 50)^2) \\ w(x, 0) &= 0\end{aligned}\tag{7.9}$$

and periodic boundary conditions. We couple different numbers of moment equations in the moment system. We choose $C_i(x, 0) = S_i(x, 0) = 0$, $i = 1, \dots, N$ and $C_j(x, 0) = S_j(x, 0) = 0$, $j = 1, \dots, M$. We use the parameters $D_r = 0.01$ and $\delta = 1$ and compute the solution of ρ at time $t = 50$. We compare this solution using different levels of detail with the solution of the coupled problem (6.1) using the same number of moment equations throughout the domain.

In Figure 7.4, the solution of the coupled moment system using the same number of moment equations throughout the domain is illustrated.

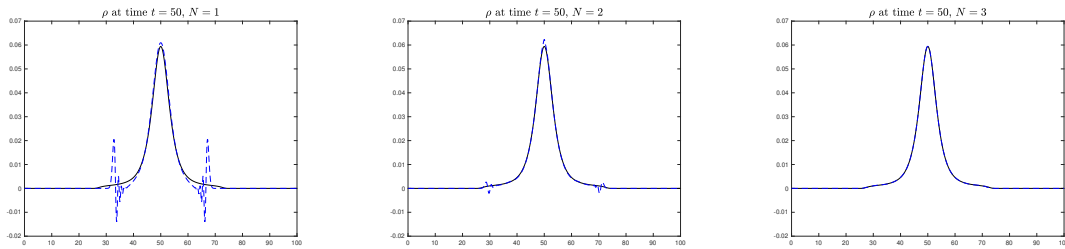


Figure 7.4.: Approximation of the coupled problem for shear flow as described in Example 7.3. The blue dashed dotted curve shows the density at time $t = 50$ for different values of N . The black solid line is a reference solution.

We plot the density ρ at time $t = 50$ for $N = 1$, $N = 2$ and $N = 3$ as a blue dashed line. The black solid line is a reference solution using $N = 20$. Using three moment equations leads to negative and thus unphysical solutions for $x \in (30, 40) \cup (60, 70)$. In spatial regions of low density the solution of the moment system using three moment equations approximates the highly resolved solution very well. The solution of the coupled moment system using five moments still leads to negative values in the intervals $[25, 35]$ and $[65, 75]$. Also in the area of the highest density $[45, 55]$, the moment system using five moments leads to deviations from the solution structure of the reference solution. A coupled moment system with seven moment equations compares well with the reference solution and does not have any unphysical solutions.

In Figure 7.5, we plot the solution of the initial problem in Example 7.3 for the last mo-

ments C_N or S_N for $N = 1$, $N = 2$ and $N = 3$ as a black solid curve. For $N = 1$, we can see that the last moment $|S_1|$ has maximal values for $x \in (30, 40) \cup (60, 70)$. Precisely in this area, the moment ρ for $N = 1$ has unphysical values in Figure 7.4. For $N = 1$, the last two moments have a magnitude of 10^{-3} . Also for $N = 2$, the intervals of the maximal values of $|C_2|$ and $|S_2|$ coincide with the intervals of negative values in the solution ρ of the coupled moment system in Figure 7.4. The inaccuracy of ρ in the interval $[45, 55]$ in Figure 7.4 is accompanied by maximal values in $|C_2|$ and $|S_2|$ with a magnitude of 10^{-4} . In the areas in which $|C_2|$ and $|S_2|$ are smaller than 10^{-5} , the solution structure of ρ compares well with the reference solution. For $N = 3$, the last two moments $|C_3|$ and $|S_3|$ are smaller than 10^{-5} . The magnitude of the last two coefficients C_3 and S_3 is that small that the solution in ρ leads to an accurate approximation of the reference solution.

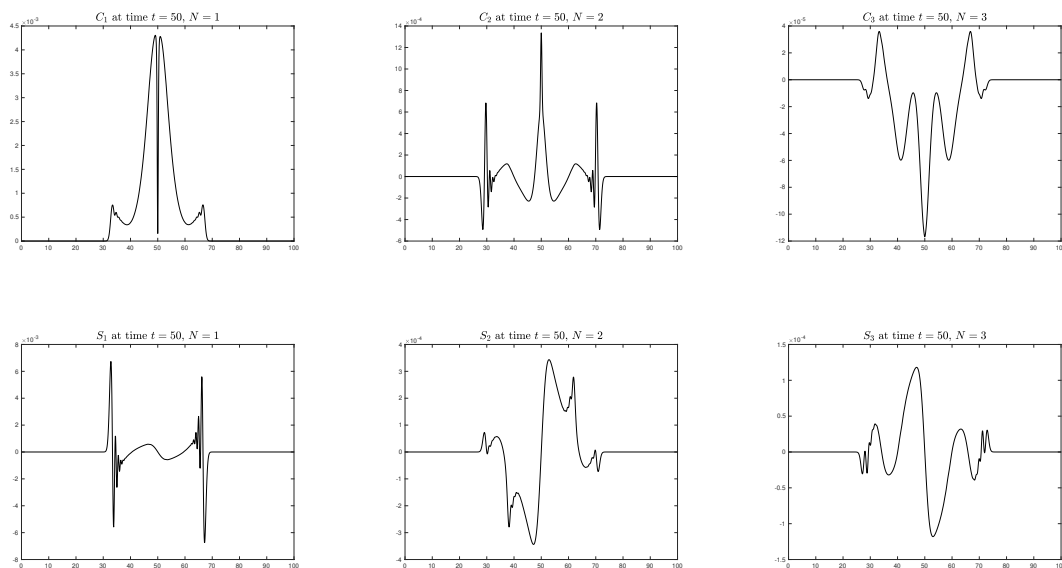


Figure 7.5.: Approximation of the coupled problem for shear flow as described in Example 7.3. The black solid curve shows the moments C_N or S_N for $N = 1$, $N = 2$, $N = 3$.

Based on these observations, we choose the number of moment equations used in the coupled moment system in the different regions of the domain $[0, 100]$ to compute an accurate and efficient approximation of the solution in Example 7.3. The solution structure observed in Figure 7.4 and Figure 7.5 suggests using three moment equations in the intervals $[0, 25]$ and $[75, 100]$. The unphysical solution of the moment system using three moments can be repaired partly by the moment system using five moments. In the intervals $[35, 45]$ and $[55, 65]$, the moment system using five moments leads to accurate solutions while the moment system using three moments leads to negative densities. The unphysical solutions of

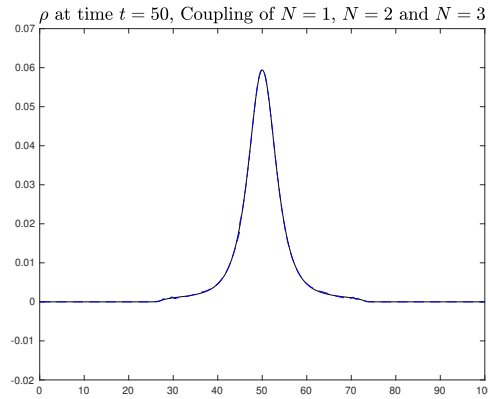


Figure 7.6.: Approximation of the coupled problem for shear flow as described in Example 7.3. The blue dashed dotted curve shows the density at time $t = 50$. We use $N = 1$ for $x \in [0, 25] \cup [75, 100]$, $N = 2$ for $x \in [35, 45] \cup [55, 65]$ and $N = 3$ for $x \in (25, 35) \cup (45, 66) \cup (65, 75)$. The black solid line is a reference solution.

the moment system using five moment equations can be repaired with the moment system using seven moment equations.

In Figure 7.6, the first component ρ of the solution of the coupled moment system with different resolution in different spatial regions and initial data as described in Example 7.3 is shown as a blue dashed line. As explained, we use three moments for $x \in [0, 25] \cup [75, 100]$, five moments for $x \in [35, 45] \cup [55, 65]$ and seven moments for $x \in (25, 35) \cup (45, 66) \cup (65, 75)$. We compare this solution of the coupled moment system using different levels of detail with a highly resolved reference solution, which is given as a black solid line. The solution of the coupled moment system using different levels of resolution has no unphysical values anymore and compares very well with the solution structure of the reference solution although only three moment equations are used on half of the domain.

The comparison demonstrates that a local increase of the number of moment equations can repair unphysical solutions of moment systems using only a few moment equations. Like this, the adaptive usage of moment systems of higher resolution leads to accurate approximations at low computational costs. The magnitude of the highest moments provides a useful selection criteria for choosing the right number of moments. The example has shown that the number of moment equations should be increased if the magnitude of the last two moments is bigger than 10^{-5} .

Conclusions and Outlook

The central goals of this thesis were to develop a moment based approximation of simplified models for sedimentation in dilute suspensions of rigid rod-like particles which can adaptively adjust the level of detail, to prove the hyperbolicity of the closed moment systems and to compare the numerical solutions of the system of moment equations and the more detailed kinetic model. In this last chapter, a summary of the new results is given along with directions for further research in this area.

8.1 New Results

We derived a hierarchy of moment equations for simplified models, which describe sedimentation in suspensions of rod-like particles. While the original system is a time-dependent partial differential equation in space and orientation, the system of moment equations depends only on space and time. We showed that the system of moment equations is hyperbolic. Furthermore, we showed that the system of moment equations can be interpreted as an approximation of the original problem. Finally, we adaptively adjusted the level of detail of the model by coupling moment systems with different numbers of moment equations. We derived a conservative high-resolution finite volume method for solving the moment systems with different resolution. Selection criteria for the choice of the right number of moment equations was presented.

Throughout the thesis, we made the simplified assumption that the macroscopic space is one or two-dimensional and that the rod-like particles are allowed to orient only in a plane.

8.2 Future Work

In future work, we plan to extend our results to more general configurations. The long-term goal is the derivation of physically realistic, moment based models and efficient numerical methods that approximate the dynamics of sedimenting rod-like particles dispersed in a three-dimensional fluid.

A first step in the direction of a generalised moment system will be to derive a spectral method for the Smoluchowski equation on S^2 , as we have seen in section 6.3 that the update described by the source term of the moment systems for the simplified problems is equivalent to the spectral method for the Smoluchowski equation with an externally imposed velocity gradient. Subsequently, we aim to generalise the evolution equations derived in [35] up to N -th order to extend the presented hierarchies of moment equations for the simplified flow problems from $f \in S^1$ to $f \in S^2$.

The observed concentration instabilities during the sedimentation process, ranging from a dilute well-stirred suspension to clusters with high particle densities, suggest the extension of the model to semi-dilute and concentrated regimes (compare with Figure 1.1). Switching locally between the models could give deeper insights into the mechanism of cluster formation.

Based on the premise that higher moments decay faster than lower moments [34], the generalised infinite systems of moment equation can be closed by neglecting moments of order $N + 1$. Many open questions concerning the principles for choosing the number of moments that should be used for accurate and efficient approximations remain. In this context, a comparison of the presented closure mechanism with the closure approximation from [34], which is based on the assumption that the evolution equation of the moments of order N can be replaced by an equilibrium relation, could be valuable.

The proof of the hyperbolicity of the systems of moment equations for the simplified flows in chapter 5 gives reason to hope that the generalised moment systems are hyperbolic, too. We are going to investigate this point in future work.

Calculating the numerical solution of the coupled generalised moment system for a three dimensional flow requires the extension of the Navier-Stokes solver to more than two dimensions. So far, it is only implemented for periodic boundary conditions and two-space dimensions. A comparison of the solution structure of the generalised moment system and the kinetic model will be of interest. A further point will be to improve the accuracy of the numerical approximation of the system of moment equations.

Appendices

CHAPTER A

Statement about the Authors Contribution to Previously Published Work

The theoretical results presented in [24] were derived by the authors supervisor, Christiane Helzel, and the author of this thesis in equal parts. All numerical computations were performed by the author of this thesis.

Bibliography

- [1] E. Abisset-Chavanne, F. Chinesta, J. Férec, G. Ausias, and R. Keunings. On the multiscale description of dilute suspensions of non-brownian rigid clusters composed of rods. *Journal of Non-Newtonian Fluid Mechanics*, 222:34–44, 2015.
- [2] S. Advani and C. L. Tucker. The use of tensors to describe and predict fiber orientation in short fiber composites. *Journal of Rheology*, 31:751 – 784, 1978.
- [3] M. Alves, P. Oliveira, and F. Pinho. Numerical methods for viscoelastic fluid flows. *Annual Review of Fluid Mechanics*, 53:1–33, 2020.
- [4] A. Ammar, B. Mokdad, F. Chinesta, and R. Keunings. A new family of solvers for some classes of multidimensional partial differential equations encountered in kinetic theory modeling of complex fluids. *Journal of Non-Newtonian Fluid Mechanics*, 139:153–176, 2006.
- [5] A. Ammar, B. Mokdad, F. Chinesta, and R. Keunings. A new family of solvers for some classes of multidimensional partial differential equations encountered in kinetic theory modeling of complex fluids. part ii. *Journal of Non-Newtonian Fluid Mechanics*, 144:98–121, 2007.
- [6] H. Anton, E. M. Grobe, and C. A. Grobe. *Elementary linear algebra*. New York [u.a.]: Wiley., 1994.
- [7] G. K. Batchelor. Slender-body theory for particles of arbitrary cross-section in stokes flow. *Journal of Fluid Mechanics*, 44(3):419–440, 1970.
- [8] J. B. Bell, P. Colella, and H. M. Glaz. A second-order projection method for the incompressible navier-stokes equations. *Journal of Computational Physics*, 85(2):257 – 283, 1989.
- [9] C. Binetruy, F. Chinesta, and R. Keunings. *Flows in polymers reinforced polymers and composites: A multiscale approach*. Springerbriefs, 2015.

- [10] D. Brown, R. Cortez, and M. L. Minion. Accurate projection methods for the incompressible navier-stokes equations. *J. Comput. Phys.*, 168:464 – 499, 2001.
- [11] J. E. Butler and E. S. G. Shaqfeh. Dynamic simulations of the inhomogeneous sedimentation of rigid fibres. *Journal of Fluid Mechanics*, 468:205 – 237, 2002.
- [12] C. Chauviere. A new method for micro-macro simulations of viscoelastic flows. *SIAM J. Sci. Comput.*, 23:2123–2140, 2002.
- [13] C. Chauviere and Alexei Lozinski. Simulation of dilute polymer solutions using a fokker–planck equation. *Computers and Fluids*, 33(5):687–696, 2004.
- [14] C. Z. Cheng and G. Knorr. The integration of the vlasov equation in configuration space. *Journal of Computational Physics*, 22(3):330–351, 1976.
- [15] F. Chinesta, R. Keunings, and Leygue A. *The proper generalized decomposition for advanced numerical simulations. A primer*. 2014.
- [16] F. Chinestra, A. Ammar, A. Leygue, and R. Keunings. An overview of the proper generalized decomposition with applications in computational rheology. *Journal of Non-Newtonian Fluid Mechanics*, 166:578–592, 2011.
- [17] A. J. Chorin. A numerical method for solving incompressible viscous flow problems. *Journal of Computational Physics*, 2(1):12 – 26, 1967.
- [18] A. J. Chorin. Numerical solution of the navier–stokes equations. *Mathematics of Computation*, 22(104):745 – 762, 1968.
- [19] A. J. Chorin. On the convergence of discrete approximations to the navier-stokes equations. *Mathematics of Computation*, 23(106):341 – 353, 1969.
- [20] D. Chung and T. Kwon. Invariant-based optimal fitting closure approximation for the numerical prediction of flow-induced fiber orientation. *Journal of Rheology*, 46:169–194, 2002.
- [21] P. Colella. Multidimensional upwind methods for hyperbolic conservation laws. *Journal of Computational Physics*, 87(1):171 – 200, 1990.
- [22] R. Courant, K. Friedrichs, and H. Lewy. On the partial difference equations of mathematical physics. *IBM Journal of Research and Development*, 11(2):215 – 234, 1967.

- [23] C. Cruz, F. Chinesta, and G. Régnier. Review on the brownian dynamics simulation of bead-rod-spring models encountered in computational rheology. *Archives of Computational Methods in Engineering*, 19:227–259, 2012.
- [24] S. Dahm and C. Helzel. Hyperbolic systems of moment equations describing sedimentation in suspensions of rod-like particles. *Multiscale Modeling & Simulation*, 20(3):1002–1039, 2022.
- [25] M. Doi and S. F. Edwards. *The theory of polymer dynamics*. International series of monographs on physics. Oxford Univ. Press, 1986.
- [26] S. K. Godunov. A difference method for numerical calculation of discontinuous solutions of the equations of hydrodynamics. *Mat. Sb.*, 47:271 – 306, 1959.
- [27] E. Guazzelli. Sedimentation of small particles: how can such a simple problem be so difficult? *Comptes Rendus Mécanique*, 334(8):539–544, 2006.
- [28] E. Guazzelli and J. Hinch. Fluctuations and instability in sedimentation. *Annual Review of Fluid Mechanics*, 43(1):97 – 116, 2011.
- [29] E. Guazzelli, J. F. Morris, and S. Pic. *A Physical Introduction to Suspension Dynamics*. Cambridge Texts in Applied Mathematics. Cambridge University Press, 2011.
- [30] P. Halin, G. Lielens, R. Keunings, and V. Legat. The lagrangian particle method for macroscopic and micro-macro viscoelastic flow computations. *Journal of Non-newtonian Fluid Mechanics*, 79:387–403, 1998.
- [31] A. Hamid, A. Arshad, S. Mehdi, M. D. Qasim, A. Ullah, J.J. Molina, and R. Yamamoto. A numerical study of sedimentation of rod like particles using smooth profile method. *International Journal of Multiphase Flow*, 127:103263, 2020.
- [32] C. Helzel and F. Otto. Multiscale simulations for suspensions of rod-like molecules. *Journal of Computational Physics*, 216(1):52 – 75, 2006.
- [33] C. Helzel and M. Schneiders. Numerical approximation of the smoluchowski equation using radial basis functions. *Journal of Computational Mathematics*, 38(1):176 – 194, 2020.
- [34] C. Helzel and A. E. Tzavaras. A comparison of macroscopic models describing the collective response of sedimenting rod-like particles in shear flows. *Physica D: Nonlinear Phenomena*, 337:18 – 29, 2016.

- [35] C. Helzel and A. E. Tzavaras. A kinetic model for the sedimentation of rod-like particles. *Multiscale Modeling and Simulation*, 15:500 – 536, 2017.
- [36] B. Herzhaft and E. Guazzelli. Experimental study of the sedimentation of dilute and semi-dilute suspensions of fibres. *Journal of Fluid Mechanics*, 384:133 – 158, 1999.
- [37] B. Herzhaft, E. Guazzelli, M. Mackaplow, and E. Shaqfeh. Experimental investigation of the sedimentation of a dilute fiber suspension. *Physical review letters*, 77:290 – 293, 1996.
- [38] J. S. Hesthaven, S. Gottlieb, and D. Gottlieb. *Spectral Methods for Time-Dependent Problems*. Cambridge Monographs on Applied and Computational Mathematics. Cambridge University Press, 2007.
- [39] E. J. Hinch and L. G. Leal. Constitutive equations in suspension mechanics. part 2. approximate forms for a suspension of rigid particles affected by brownian rotations. *Journal of Fluid Mechanics*, 76(1):187 – 208, 1976.
- [40] R. A. Horn and C. R. Johnson. *Matrix Analysis*. Cambridge [u.a.]: Cambridge Univ. Press., 1996.
- [41] M. Hulsen, A.P.G Heel, and B.H.A.A Brule. Simulation of viscoelastic flow using brownian configuration fields. *Journal of Non-Newtonian Fluid Mechanics*, 70:79–101, 1997.
- [42] Shen J. and Haijun Yu. On the approximation of the fokker–planck equation of the finitely extensible nonlinear elastic dumbbell model i: A new weighted formulation and an optimal spectral-galerkin algorithm in two dimensions. *SIAM Journal on Numerical Analysis*, 50:1136–1161, 2012.
- [43] L. Ji and J. Ryan. *Smoothness-Increasing Accuracy-Conserving (SIAC) Filters in Fourier Space*, pages 415–423. 01 2015.
- [44] Liangyue Ji, P. Slingerland, J. Ryan, and C. Vuik. Superconvergent error estimates for position-dependent smoothness-increasing accuracy-conserving (siac) post-processing of discontinuous galerkin solutions. *Mathematics of Computation*, 83, 09 2014.
- [45] K. Gustavsson and A. K. Tornberg. Gravity induced sedimentation of slender fibers. *Physics of Fluids*, 21:123301, 2009.
- [46] R. Keunings. Micro-macro methods for the multiscale simulation of viscoelastic flow using molecular models of kinetic theory. page 67.98, 2004.

- [47] J. Kim and P. Moin. Application of a fractional-step method to incompressible navier-stokes equations. *Journal of Computational Physics*, 59(2):308 – 323, 1985.
- [48] D. Knezevic and E. Süli. A heterogeneous alternating-direction method for a micro-macro dilute polymeric fluid model. 43(6):1117 – 1156, 2009.
- [49] D. L. Koch and E. S. G. Shaqfeh. The instability of a dispersion of sedimenting spheroids. *Journal of Fluid Mechanics*, 209:521 – 542, 1989.
- [50] M. Laso and H.C. Öttinger. Calculation of viscoelastic flow using molecular models: the connffessit approach. *Journal of Non-Newtonian Fluid Mechanics*, 47:1–20, 1993.
- [51] N. Lebovka, Y. Tarasevich, L. Bulavin, V. Kovalchuk, and N. Vygornitskii. Sedimentation of a suspension of rods: Monte carlo simulation of a continuous two-dimensional problem. *Physical Review E*, 99, 2019.
- [52] L. Lee. A class of high-resolution algorithms for incompressible flows. *Computers and Fluids*, 39(6):1022 – 1032, 2010.
- [53] R. J. LeVeque. *Numerical methods for conservation laws*. Lectures in mathematics. Birkhäuser, Basel u.a., 1990.
- [54] R. J. LeVeque. High-resolution conservative algorithms for advection in incompressible flow. *SIAM Journal on Numerical Analysis*, 33(2):627 – 665, 1996.
- [55] R. J. LeVeque. Wave propagation algorithms for multidimensional hyperbolic systems. *Journal of Computational Physics*, 131(2):327 – 353, 1997.
- [56] R. J. LeVeque. *Finite Volume Methods for Hyperbolic Problems*. Cambridge Texts in Applied Mathematics. Cambridge University Press, 2002.
- [57] J. Lin, Y. Wang, W. Wang, and Z. Yu. Numerical simulation of the sedimentation of cylindrical pollutant particles in fluid. *Journal of Environmental Sciences*, 14(4):433 – 438, 2002.
- [58] C. Lohmann. Efficient algorithms for constraining orientation tensors in galerkin methods for the fokker–planck equation. *Computers and Mathematics with Applications*, 71(5):1059–1073, 2016.
- [59] F. Lundell, D. Söderberg, and P. Alfredsson. Fluid mechanics of papermaking. *Annual Review of Fluid Mechanics*, 43:195–217, 01 2011.

- [60] M. B. Mackaplow and E. S. G. Shaqfeh. A numerical study of the sedimentation of fibre suspensions. *Journal of Fluid Mechanics*, 376:149 – 182, 1998.
- [61] J. Martin, A. Lusher, R. Thompson, and A. Morley. The deposition and accumulation of microplastics in marine sediments and bottom water from the irish continental shelf. *Scientific Reports*, 7, 2017.
- [62] B. Metzger and J. Butler and E. Guazzelli. Experimental investigation of the instability of a sedimenting suspension of fibres. *Journal of Fluid Mechanics*, 575:307 – 332, 2007.
- [63] B. Metzger, E. Guazzelli, and J. Butler. Large-scale streamers in the sedimentation of a dilute fiber suspension. *Physical review letters*, 95(16):164506, 2005.
- [64] B. Mokdad, E. Prulière, A. Ammar, and F. Chinesta. On the simulation of kinetic theory models of complex fluids using the fokker-planck approach. *Appl. Rheol*, 2, 2007.
- [65] E. Nazockdast, A. Rahimian, D. Zorin, and M. J. Shelley. A fast platform for simulating semi-flexible fiber suspensions applied to cell mechanics. *J. Comput. Phys.*, 329:173–209, 2017.
- [66] J. M. Nitsche and G. K. Batchelor. Break-up of a falling drop containing dispersed particles. *Journal of Fluid Mechanics*, 340:161 – 175, 1997.
- [67] H.C. Öttinger. *Stochastic Processes in Polymeric Fluids: Tools and Examples for Developing Simulation Algorithms*. Springer, 1996.
- [68] F. Otto and A. E. Tzavaras. Continuity of velocity gradients in suspensions of rod-like molecules. *Comm. Math. Phys.*, 277:729 – 758, 2008.
- [69] J. Park. *Dynamics of Suspensions of Rodlike Polymers with Hydrodynamic Interactions*. PhD thesis, 05 2009.
- [70] J. Park, B. Metzger, E. Guazzelli, and J. E. Butler. A cloud of rigid fibres sedimenting in a viscous fluid. *Journal of Fluid Mechanics*, 648:351 – 362, 2010.
- [71] M. Perez, A. Scheuer, E. Abisset-Chavanne, A. Ammar, F. Chinesta, and R. Keunings. On the multi-scale description of micro-structured fluids composed of aggregating rods. *Continuum Mechanics and Thermodynamics*, 2018.
- [72] W. H. Reinhart, A. Singh, and S. Werner. Red blood cell aggregation and sedimentation: the roll of cell shape. *Brit. J. Hematol.*, 73:551 – 556, 1989.

- [73] J. A. Rossmannith and D. C. Seal. A positivity-preserving high-order semi-lagrangian discontinuous galerkin scheme for the vlasov–poisson equations. *Journal of Computational Physics*, 230(16):6203 – 6232, 2011.
- [74] J. Ryan. *Exploiting Superconvergence Through Smoothness-Increasing Accuracy-Conserving (SIAC) Filtering*, pages 87–102. 01 2015.
- [75] J. Ryan and B. Cockburn. Local derivative post-processing for the discontinuous galerkin method. *J. Comput. Physics*, 228:8642–8664, 12 2009.
- [76] J. Ryan, C.-W. Shu, and H. Atkins. Extension of a post processing technique for the discontinuous galerkin method for hyperbolic equations with application to an aeroacoustic problem. *SIAM J. Scientific Computing*, 26:821–843, 01 2005.
- [77] D. Saintillan, E. F. Darve, and E. Shaqfeh. A smooth particle-mesh ewald algorithm for stokes suspension simulations: The sedimentation of fibers. *Physics of Fluids*, 17:033301, 2005.
- [78] A. Scheuer, G. Gregoire, E. Abisset-Chavanne, F. Chinesta, and R. Keunings. Modelling the effect of particle inertia on the orientation kinematics of fibres and spheroids immersed in a simple shear flow. *Computers and Mathematics with Applications*, 79, 2019.
- [79] F. Schneider, G. Alldredge, M. Frank, and A. Klar. Higher order mixed-moment approximations for the fokker-planck equation in one space dimension. *SIAM Journal on Applied Mathematics*, 74(4):1087–1114, 2014.
- [80] W. E. Stewart and J. P. Sorensen. Hydrodynamic interaction effects in rigid dumb-bell suspensions ii computations for steady shear flow. *Transactions of the Society of Rheology*, 16:1–13, 1972.
- [81] G. Strang. On the construction and comparison of difference schemes. *SIAM Journal on Numerical Analysis*, 5(3):506 – 517, 1968.
- [82] J. Su, C. Hou, Y. Ma, and Y. Wang. Multilevel monte carlo method for the brownian configuration field of polymer fluids. *AIP Advances*, 10:095013, 2020.
- [83] A. Tiehm, V. Herwig, and U. Neis. Particle size analysis for improved sedimentation and filtration in waste water treatment. *Water Science and Technology*, 39(8):99–106, 1999.

- [84] A. K. Tornberg and K. Gustavsson. A numerical method for simulations of rigid fiber suspensions. *Journal of Computational Physics*, 215(1):172 – 196, 2006.
- [85] H. Vandeven. Family of spectral filters for discontinuous problems. *J. Sci. Comput.*, 6(2):159–192, 1991.

List of Figures

1.1. Concentration regimes of rod-like polymers: (a) dilute solution, (b) semidilute solution, (c) isotropic concentrated solution, and (d) liquid crystalline solution. Compare with [25, Fig. 9.1].	2
1.2. Sketch of the structural instability of a sedimenting suspension of fibres. Compare with [29, chap. 6, Fig. 6.15].	2
1.3. Experimental simulation of the evolution of a cloud of rigid fibres. Images in the top row are views normal to the direction of gravity; the row of images on the bottom are views from the direction of gravity. The rigid fibres are made of copper with a dimension of $l = 0.127 \pm 0.013$ cm and $d = 0.0149 \pm 0.0020$ cm. Compare with [69, Fig. D-1], [70].	3
2.1. Construction of the solution of the Riemann problem in Example 2.6 in the $x - t$ plane. The jump across each discontinuity in the solution is an eigenvector of A	14
2.2. Illustration of a finite volume method for updating the cell average Q_i^n by fluxes at the cell edge. Shown in the $x - t$ space. Compare with [56, chap. 4].	15
2.3. Schematic of Godunov's Method for the linear system in (2.3). Riemann problems are solved at each interface. The exact solution at time t^{n+1} is determined by the wave structure. The solution is averaged over the grid cell to determine Q_i^{n+1}	17
2.4. Finite volume grid in two space dimensions, where $Q_{i,j}^n$ represents a cell average at time t^n . Compare with [56, chap. 19].	20
2.5. Illustration of the four transverse flux differences for a general system of equations. Compare with [55].	21
2.6. The interface velocity values.	24
2.7. Variables of the projection method for the Navier-Stokes equation (2.33). . .	27
3.1. Basic notation for a rod-like molecule which is falling sideways, see [35]. .	31

4.1. Modulus of coefficients c_i, s_i versus i for the spectral representation of f in the steady state approximation for shear flow with different values of $ w_x /D_r$.	38
4.2. Approximations of steady state solutions of f for externally imposed shear flow with $w_x/D_r = 10$ and different values of N .	39
4.3. Approximations of steady state solutions of f for externally imposed shear flow with $ w_x /D_r = 100$ and different values of N .	39
4.4. Approximations of steady state solutions of f for externally imposed shear flow with $w_x/D_r = 1000$ and different values of N .	40
4.5. Modulus of coefficients c_i, s_i versus i for the filtered and unfiltered spectral representations of f in the steady state approximation for shear flow with different values of $ w_x /D_r$.	42
4.6. Comparison of the approximations of the steady state solution of f for externally imposed shear flow with $w_x/D_r = 100$ and $N = 3$ using the filtered and unfiltered spectral methods.	43
4.7. Approximations of steady state solutions of f for externally imposed shear flow with $w_x/D_r = 100$ and different values of N using the exponential filter in the spectral method.	44
4.8. Grid for the numerical approximation of the one-dimensional transport equation (4.2), where $f_{i,k}^n$ approximates the cell average at time t^n .	45
5.1. Structure of the matrix S for $N = 5$.	59
5.2. Structure of the matrix $Z = S\bar{A}$ for $N = 5$.	61
5.3. Structure of the matrix S^{-1} for $N = 5$.	63
5.4. Structure of the matrix S for $N = 4$.	67
5.5. Structure of the matrix $Z := S\bar{A}$ for $N = 4$.	69
5.6. Structure of the matrix S^{-1} for $N = 4$.	71
6.1. Illustration of the staggered grid used for the discretisation of (6.1).	90
6.2. Illustration of the grid used for the discretisation of (6.2).	92
6.3. Solution of the Riemann problem defined in Example 6.2 using a highly resolved solution of subproblem (4.2) (blue curve) and the moment system for different N (red curve). The black curve is a highly resolved reference solution. The initial values are steady state solutions of the Smoluchowski equation with left state $w_x/D_r = 10$ and right state $w_x/D_r = 20$.	94

6.4. Solution of the Riemann problem defined in Example 6.2 using a highly resolved solution of subproblem (4.2) (blue curve) and the moment system for different N (red curve). The black curve is a highly resolved reference solution. The initial values are steady state solutions of the Smoluchowski equation with left state $w_x/D_r = 100$ and right state $w_x/D_r = 200$	95
6.5. Solution of the Riemann problem using coarse grids in θ for the solution of subproblem (4.2) (blue dashed curve) and the exact solution of the Riemann problem for the homogeneous moment system (red dashed-dotted curve) for odd N	96
6.6. Illustration of the relation between the solution of the Riemann problem for the hyperbolic system and a coarse grid approximation of the transport equation (4.2).	97
6.7. Solution of the Riemann problem using coarse grids in θ for the solution of the subproblem (4.2) (blue dashed curve) and the exact solution of the Riemann problem for the homogeneous moment system (red dashed-dotted curve) for even N	98
6.8. Solution of the Riemann problem defined in Example 6.4 using a highly resolved solution of subproblem (4.7) (blue curve) and the moment system for different N (red curve). The black curve is a highly resolved reference solution.	99
6.9. Solution of the Riemann problem using coarse grids in θ for the solution of the subproblem (4.7) (blue dashed curve) and the exact solution of the Riemann problem for the homogeneous moment system (red dashed-dotted curve) for different N	99
6.10. Approximation of the coupled problem for shear flow as described in Example 6.5. We show the density at time $t = 50$ for $N = 1$ and $N = 2$ as dashed blue line. The black solid line is a reference solution computed using $N = 50$	100
6.11. Approximation of the coupled problem for shear flow as described in Example 6.5 but with $D_r = 1$. We show the density at time $t = 50$ for $N = 1$ as dashed blue line. The black solid line is a reference solution computed using $N = 50$	101
6.12. Approximation of the coupled problem for shear flow as described in Example 6.6. We show the density at time $t = 30$ for different values of N as blue dashed line. The black solid line is a reference solution computed using $N = 50$. (Note different y-axis.)	102

6.13. Numerical solutions of the two-dimensional coupled problem described in Example 6.7 for $N = 1$ (top), $N = 4$ (middle) and $N = 10$ (bottom).	105
7.1. Structure of the solution Q of the generalised Riemann Problem for $N = 1$ and $M = 2$. The value of Q is constant in each wedge of the $x - t$ plane. . .	108
7.2. Solution of the generalised Riemann problem described in Example 7.1. The blue dashed dotted curve is the solution for different values of N and $M = 20$. The red dashed curve is a rough solution using different values of $N = M$ throughout the domain. The purple dotted curve is a detailed solution using $N = M = 20$ throughout the domain. The black solid curve is a highly resolved reference solution.	109
7.3. Schematic diagram of the Godunov's method for solving the generalised Riemann Problem (7.1) for $N = 1$ and $M = 2$. The Riemann problem is solved at each cell interface.	113
7.4. Approximation of the coupled problem for shear flow as described in Example 7.3. The blue dashed dotted curve shows the density at time $t = 50$ for different values of N . The black solid line is a reference solution.	114
7.5. Approximation of the coupled problem for shear flow as described in Example 7.3. The black solid curve shows the moments C_N or S_N for $N = 1$, $N = 2$, $N = 3$	115
7.6. Approximation of the coupled problem for shear flow as described in Example 7.3. The blue dashed dotted curve shows the density at time $t = 50$. We use $N = 1$ for $x \in [0, 25] \cup [75, 100]$, $N = 2$ for $x \in [35, 45] \cup [55, 65]$ and $N = 3$ for $x \in (25, 35) \cup (45, 66) \cup (65, 75)$. The black solid line is a reference solution.	116

List of Tables

6.1. Accuracy study for the problem in Example 6.6 using $N = 1, \dots, 4$ moment equations. The reference solution uses the same number of moment equations as the coarse solution. The models are discretised with the methods from section 6.1.	102
6.2. Accuracy study for the problem in Example 6.6 using $N = 5, N = 10, N = 15$ and $N = 20$ moment equations. The reference solution uses the same number of moment equations as the coarse solution. The models are discretised with the methods from section 6.1.	103
6.3. Accuracy study for the problem in Example 6.6 using $N = 1, \dots, 4$. The reference solution uses $N = 20$ moment equations. The models are discretised with the methods from section 6.1.	103
6.4. Accuracy study for the problem in Example 6.6 using $N = 5, N = 10, N = 15$ and $N = 20$. The reference solution uses $N = 20$ moment equations. The models are discretised with the methods from section 6.1.	104

Affidavit

I declare under oath that I have produced my thesis independently and without any undue assistance by third parties under consideration of the 'Principles for the Safeguarding of Good Scientific Practice at Heinrich Heine University Düsseldorf'.

Düsseldorf, 1st September 2022

Sina Dahm